SATELLITE BASED PASSIVE RADAR SYSTEM

Nihat Mert Ünal

FEBRUARY 2019

SATELLITE BASED PASSIVE RADAR SYSTEM

A THESIS SUBMITTED TO

THE GRADUATE SCHOOL OF NATURAL AND APPLIED

SCIENCES OF

ÇANKAYA UNIVERSITY

BY

NİHAT MERT ÜNAL

IN PARTIAL FULFILLMENT OF THE REQUIREMENTS FOR THE

DEGREE OF

MASTER OF SCIENCE

IN

ELECTRONIC AND COMMUNICATION ENGINEERING

DEPARTMENT

FEBRUARY 2019

Title of the Thesis: **Satellite Based Passive Radar System.**

Submitted by **Nihat Mert ÜNAL**

Approval of the Graduate School of Natural and Applied Sciences, Çankaya University.

Prof. Dr. Can ÇOĞUN

Director

I certify that this thesis satisfies all the requirements as a thesis for the degree of Master of Science.

Dr. Lecturer Özgür ERGÜL

Head of Department

This is to certify that we have read this thesis and that in our opinion it is fully adequate, in scope and quality, as a thesis for the degree of Master of Science.

Prof. Dr. Yusuf Ziya UMUL

Supervisor

Examination Date: 05.02.2019

Examining Committee Members

Prof. Dr. Yusuf Ziya UMUL	(Çankaya Univ.)	
Assoc. Prof. Dr. Hüsnü Deniz BAŞDEMİR	(Çankaya Univ.)	
Assoc. Prof. Dr. Nursel Akçam	(Gazi Univ.)	

STATEMENT OF NON-PLAGIARISM

I hereby declare that all information in this document has been obtained and presented in accordance with academic rules and ethical conduct. I also declare that, as required by these rules and conduct, I have fully cited and referenced all material and results that are not original to this work.

Name, Last Name: Nihat Mert Ünal

Signature :

Date : 18.02.2019

ABSTRACT

SATELLITE BASED PASSIVE RADAR SYSTEM

ÜNAL, Nihat Mert

M.Sc., Department of Electronic and Communication Engineering

Supervisor: Prof. Dr. Yusuf Ziya UMUL

February 2019, 108 pages

In this thesis, satellite based passive radar's electromagnetic propagation is investigated. Electromagnetic wave which radiated from satellite will propagate through whole atmosphere and scattered by targets which will be modeled as civilian plane and stealth aircraft. Firstly, Modified Theory of Physical Optics (MTPO) is introduced. Diffraction deficiency of Physical Optics (PO) is eliminated by MTPO. Secondly, satellite antenna which is Perfectly Electric Conductor (PEC) Cylindrical Parabolic Reflector Antenna (CPRA) is introduced. CPRA's scattered fields are evaluated. In this thesis, reflected scattered field by CPRA is used as radiated electromagnetic wave. Another point of view of this thesis is Gaussian beam modelling. Radiated electromagnetic wave which is CPRA's reflected scattered field is modeled as Gaussian beam. Gaussian beam's incident Geometrical Optics (GO) wave is used as radiated field from satellite antenna which passes through atmosphere. Fourthly, atmosphere is modeled as using International Telecommunication Union Radiocommunication (ITU-R) Recommendations. Impairments of the atmosphere is investigated. Then, plane wave scattering by PEC surface line strip which is model of civilian plane is expressed. Also, plane wave scattering by perfectly absorbing surface which is model of stealth aircraft is investigated. Finally, numerical analysis is represented for attenuation by atmosphere, civilian plane with original dimension and stealth aircraft with original dimension and results are discussed.

Keywords: Radar, Satellite, Passive Radar, Line Strip, Edge Diffraction, Stealth Aircraft

ÖZ

UYDU TABANLI PASİF RADAR SİSTEMİ

ÜNAL, Nihat Mert

Yüksek Lisans, Elektronik ve Haberleşme Mühendisliği Anabilim Dalı

Tez Yöneticisi: Prof. Dr. Yusuf Ziya UMUL

Şubat 2019, 108 sayfa

Bu tezde uydu tabanlı pasif radarların elektromanyetik yayılımı incelenmiştir. Uydudan yayılan elektromanyetik alanlar tüm atmosferi geçecek ve hedeften saçılacaktır. Bu hedefler sivil uçak ve görünmez savaş uçağıdır. Birinci olarak, Modified Theory of Physical Optics (MTPO)'den bahsedilmiştir. Physical Optics (PO) metodunun kırınan alanlardaki eksikliği MTPO kullanılarak giderilmiştir. İkinci olarak, mükemmel iletken yüzeye sahip silindirik parabolik yansıtıcı uydu anteninden saçılan alanlardan bahsedilmiştir. Silindirik parabolik yansıtıcı antenin yansıyan saçılan alanları bu tezde uydudan yayılan alan olarak kullanılacaktır. Bu tezin bir başka ana noktası da uydu anteninden yayılan alanın Gauss ışınları olarak modellenmesidir. Gauss ışınlarından gelen Geometrik Optik (GO) alanı uydudan yayılan alan olarak kullanılmıştır. Bu tezde, bu alan tüm atmosferi geçecek olan alandır. Dördüncü olarak, atmosfer International Telecommunication Union Radiocommunication (ITU-R) tavsiyeleri kullanılarak modellenmiştir. Atmosferdeki bozulmalar ortaya konmuştur. Sivil uçağın modeli olan mükemmel iletken yüzeye sahip çizgi şeritten düzlemsel dalga saçılımı açıklanmıştır. Ayrıca, görünmez savaş uçağının modeli olan mükemmel soğurucu yüzeye sahip çizgi şeritten düzlemsel dalga saçılımından bahsedilmiştir. Son olarak, atmosferdeki bozulumlardan kaynaklı sönümlenmeler, gerçek uzunlukları hesaba katılmış sivil uçak ve gerçek uzunlukları hesaba katılmış görünmez savaş uçağı numerik olarak analiz edilmiştir. Sonuçlar tartışılmıştır.

Anahtar Kelimeler: Radar, Uydu, Pasif Radar, Çizgi Şerit, Kenar Kırınımı, Görünmez Savaş Uçağı

ACKNOWLEDGEMENTS

I would like to express my sincere gratitude to Prof. Dr. Yusuf Ziya UMUL for his supervision, special guidance, suggestions, and encouragement through the development of this thesis.

I would like to express my sincere gratitude to Assoc. Prof. Dr. Hüsnü Deniz Başdemir for his suggestions, and encouragement through the development of this thesis.

It is a pleasure to express my special thanks to my family for their valuable support.

TABLE OF CONTENTS

LIST OF FIGURES

LIST OF TABLES

LIST OF ABBREVIATIONS

PO	Physical Optics
MTPO	Modified Theory of Physical Optics
GO	Geometrical Optics
GTD	Geometrical Theory of Diffraction
PEC	Perfectly Electric Conducting
CPRA	Cylindrical Parabolic Reflector Antenna
PAS	Perfectly Absorbing Surface

CHAPTER 1
1. INTRODUCTION

Satellite based passive radars are most researched topic nowadays. Many scientists are working on satellite based passive radars, but they are working on signal processing part. There are so many advantages of this type of radar. The biggest advantage is that there are no ground-based active radar systems with transmitter. Radar system which is satellite based does not need dedicated transmitter system, [1]. Countries can detect targets as just using broadcasts of satellites. This make countries achieve well designed electronic defense systems. Another advantage of satellite based passive radar is that country surveillance can be performed by single satellite. Which means that countries don't need many ground-based active radar systems.

In this thesis, satellite based passive radar's electromagnetic propagation model is investigated. Electromagnetic fields which are radiated from satellite's antenna will pass through whole atmosphere. There will be impairments in the atmosphere. After passing through atmosphere, electromagnetic waves are scattered by the target. Then, scattered fields by target will reach the ground-based receiver radar system. Planes will be modeled as civilian and stealth aircrafts. In the Figure 1, general view of the satellite based passive radar is shown.

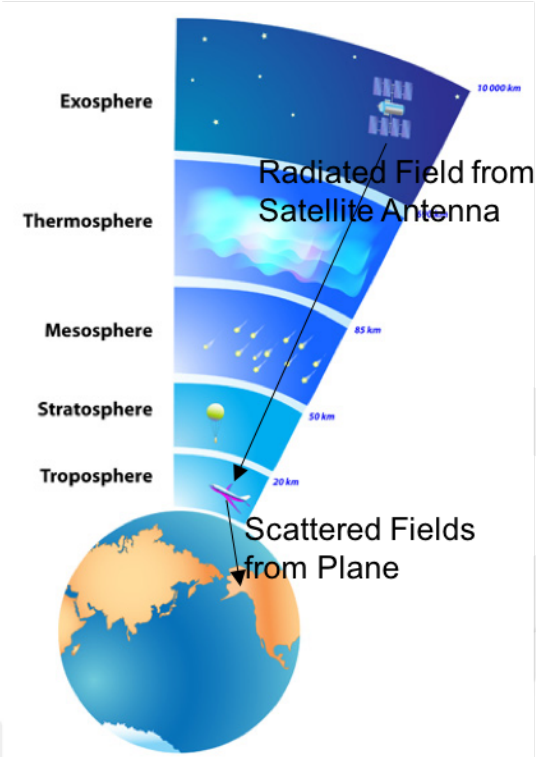

Figure 1. General view of satellite based passive radar

Thesis divided into 6 parts which are expressing MTPO method, radiated fields from satellite antenna, modelling radiated fields of satellite antenna as Gaussian beam, atmospheric propagation, scattered fields by civilian plane and scattered fields by stealth aircraft.

There are few scientific studies about electromagnetic propagation of satellite based passive radar issue. However, satellite communication or mobile communication based on satellite is researched by scientists. There are studies about the electromagnetic scattering by buildings for satellite or mobile communications systems, [2]. Valtr et all. are also studies about wave scattering model by buildings for satellite communication, [3]. Valtr et al. and Miyazaki et al. are not concerned with atmospheric impairments and radiated fields from satellite antennas. They just modeled scattering fields by buildings. On the other hand, satellite radiowave propagation is studied widely. Allnutt is modeled satellite to ground electromagnetic propagation, [4]. Also, Ippolito investigated the radiowave propagation of satellite, [5]. Satellite communications is observed by Roddy, [6].

Modified Theory of Physical Optics(MTPO) method is used instead of Physical Optics (PO) method in order to find scattered fields in this thesis, [7]. MTPO method has advantages comparing PO method and these advantages are expressed in the

Section 2. MTPO is derived by Umul for finding exact solution on edge diffraction. PO method has weak spot on edge diffraction. This deficiency is exterminated by Umul, [7].

Cylindrical parabolic reflector antenna is most commonly used type of antenna for satellite systems. Satellite antenna is chosen as cylindrical parabolic reflector antenna. In this thesis, cylindrical parabolic reflector's surface is modeled as PEC surface. And feeder is selected as line source. Uniform scattered fields by cylindrical parabolic antenna will be investigated. MTPO method is used. Geometrical theory of diffraction method is used to calculate diffracted fields, [8]. Scattered fields of line source are investigated by Umul from cylindrical parabolic reflector which is scattered by impedance surface, [9]. Büyükaksoy et al [10] and Akduman et al [11] studied scattered fields by curved surfaces. Bucci et al was modeled rim loaded reflector antennas by using Maliuzhinet's function, [12]. Yalçın et al was researched uniform diffracted fields by PEC cylindrical parabolic reflector, [13]. Also, Yalçın et al was researched uniform scattered fields by PEC cylindrical parabolic reflector, [14]. Kara was investigated scattered fields of plane waves by PEC cylindrical parabolic reflector, [15]. Simulation of cylindrical parabolic reflector antennas was done by Ragheb, [16].

Gaussian beam will be used to model reflected scattered fields of cylindrical parabolic reflector antenna. Gaussian beam is investigated widely, [17-23]. In this thesis, Umul's beam diffraction article is implemented for modeling reflected scattered field of cylindrical parabolic reflector antenna, [24]. GO incident field of Gaussian beam is used.

Atmospheric propagation is one of the most important issue for satellite based passive radars. Application of satellite based passive radar has big dependency about electromagnetic wave which pass through atmosphere. Atmosphere modelling for electromagnetic wave propagation is widely studied topic. There are so many paper and books about this issue. Atmosphere modelling tree has 4 important impairment types. These are atmospheric gaseous attenuation, tropospheric scintillation attenuation, cloud attenuation and rain attenuation. However, in this thesis rain attenuation is neglected. Rainless medium is considered. There are many researches about atmospheric gaseous attenuation, [25-35]. One of the most important impairment is cloud attenuation and there are many studies about it, [36-46]. The last impairment is tropospheric scintillation attenuation which is studied a lot, [47-54]. In this thesis, ITU-R atmospheric model will be used, [55-59].

Civilian plane is modeled as PEC line strip in this thesis. Line strips dimensions are calculated with plane's dimensions. Plane is chosen as Boeing 737-900, (Figure 26). Scattered fields by line strip are investigated. One of the most important part of this thesis is scattered fields by plane which means that line strip. Because, satellite-based radar systems are focusing mostly scattered fields by targets. Detection of target is mostly depending on gathering electromagnetic waves scattered by target. Diffraction by strip is researched greatly, [60-64]. In this thesis, scattered field by strip is obtained with using MTPO method.

Stealth aircraft is modeled as perfectly absorbing line strip in this thesis. PAS line strip dimensions are evaluated with using Lockheed F-117 Nighthawk's dimensions, (Figure 60). Scattered fields by PAS line strip is represented. Scattered fields by stealth plane is one of the most important part of this thesis. Because, detection of stealth plane is one of the most researched topic in the literature and also in the practice. Kirchhoff integration will be used to evaluate scattered fields by PAS line strip. It is expressed that summation of hard surface and soft surface is equal to PAS surface, [65-70]. There are many researches about scattering of PAS which is also known as Black Half surface, [71-77].

CHAPTER 2

2. MODIFIED THEORY OF PHYSICAL OPTICS(MTPO)

MTPO which is a new procedure found by Y.Z. Umul was introduced for calculating the scattered fields by PEC surface, impedance surface, resistive surface, etc, [7]. In this method, there are three assumptions. These are a new unit vector, reflection angle which is function of integral variables, the angle between reflected and incident rays are dividing into two equal parts. Aperture part also is taking account on this method. In this method, stationary phase method and edge point method are used for evaluating reflected, reflected diffracted, incident and incident diffracted fields asymptotically. Differences between PO and MTPO are aperture part and new unit vector. PO method is weak on edge diffraction. This method is solved this problem.

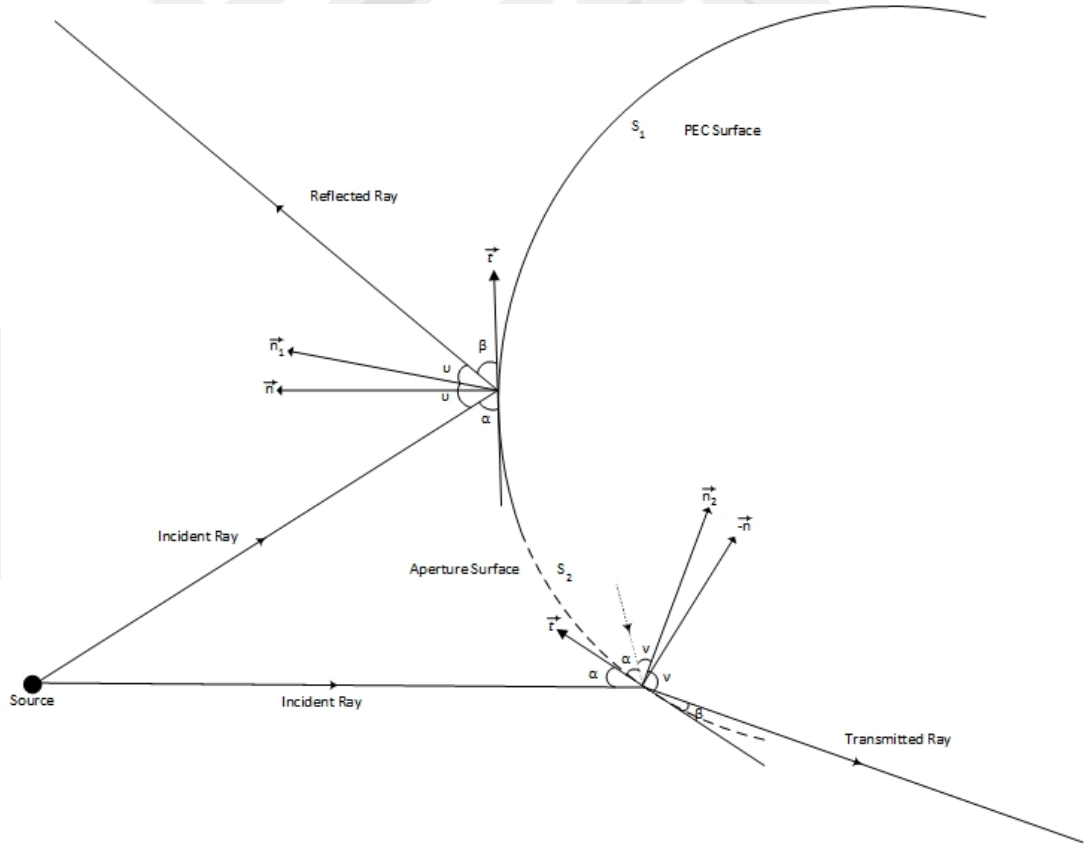

Figure 2. Fields which scattered by PEC and Aperture Surface

In Figure 2, we can clearly see that we are considering aperture surface which is not considered in PO method. s_1 is PEC surface part and s_2 is aperture part. υ is

angle between new unit vector which is at PEC surface and reflected, incident rays. β is angle between $\vec{t}$ axis and reflected which is at PEC surface, transmitted rays which is at aperture surface. α is angle of incidence. ν is angle between new unit vector which is at aperture surface and transmitted, image incident rays, [7].

In this method, there are 3 axioms which are

1. There are scattering fields by s_1 and s_2 surfaces. On PEC surface, surface current is induced by incident ray. Reflected and reflected diffracted fields can be found by evaluating integration of surface current in PO method. As we said before, PO method is not considering incident diffracted fields. Because of this, in this method s_2 surface is considered. Equivalent Source Theorem is used when finding equivalent current at aperture surface. With integrating this current on aperture surface, radiated fields can be found. Incident and incident diffracted fields are parts of radiated fields. s_1 surface's current can be expressed as

$$\overrightarrow{J_{es}} = \overrightarrow{n_1} \times \overrightarrow{H_t}\big|_{s_1}, \tag{2.1}$$

where $\overrightarrow{H_t}$ is the total magnetic field on PEC surface. With using Equivalent Source Theorem on s_2 surface, aperture surface current can be expressed as

$$\overrightarrow{J_{es}} = \overrightarrow{n_2} \times \overrightarrow{H_i}\big|_{s_2}, \overrightarrow{J_{ms}} = -\overrightarrow{n_2} \times \overrightarrow{E_i}\big|_{s_2}. \tag{2.2}$$

where $\overrightarrow{E_i}$, $\overrightarrow{H_i}$ are incident electric field and incident magnetic field respectively on aperture surface.

2. Angle β which is reflection and transmission angle is depended on the surface coordinates.

1. New unit vectors $(\overrightarrow{n_1}, \overrightarrow{n_2})$ can be defined as

$$\overrightarrow{n_1} = \cos(\upsilon + \alpha)\,\vec{t} + \sin(\upsilon + \alpha)\,\vec{n}\ ,\ \overrightarrow{n_2} = \cos(\nu + \alpha)\,\vec{t} - \sin(\nu + \alpha)\,\vec{n}\ , \tag{2.3}$$

where $\vec{t}$ is actual tangential.

Geometry of PEC surface reflection point is shown in Figure 3.

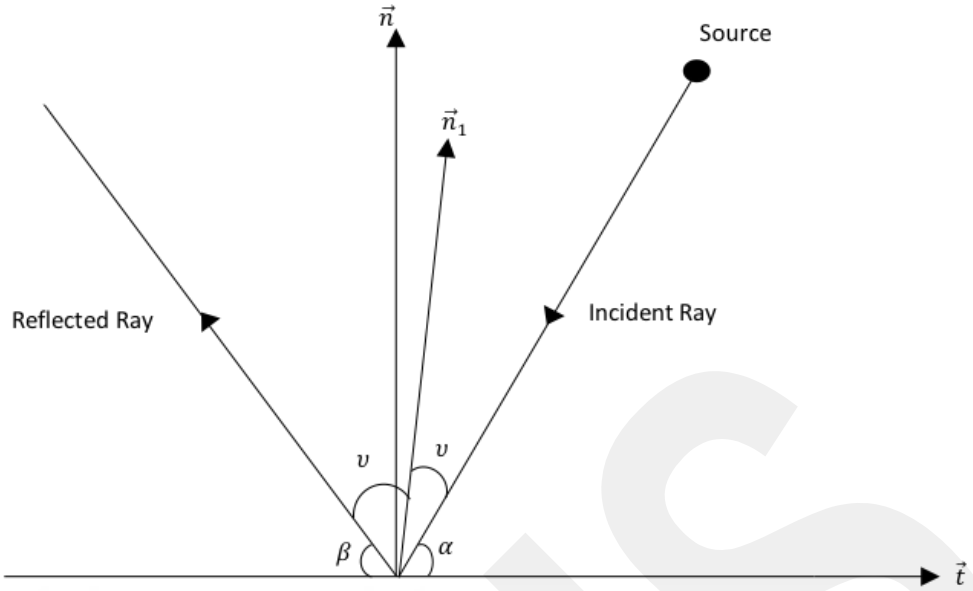

Figure 3. Geometry of PEC surface reflection point.

As seen Figure 3,

$$\upsilon = \frac{\pi}{2} - \frac{(\alpha + \beta)}{2}. \tag{2.4}$$

Geometry of aperture surface transmission point is shown in Figure 4.

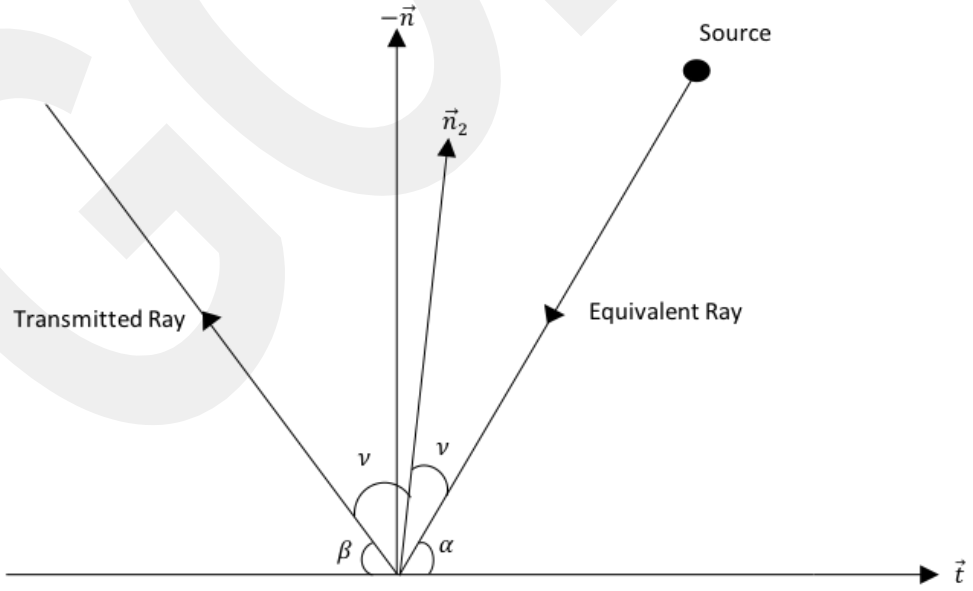

Figure 4. Geometry of aperture surface transmission point.

As seen Figure 4,

$$\nu = \frac{\pi}{2} - \frac{(\alpha + \beta)}{2}. \tag{2.5}$$

The total magnetic field can be defined as

$$\overrightarrow{H_t} = \overrightarrow{H_{ıs}} + \overrightarrow{H_{rs}}, \tag{2.6}$$

where

$$\overrightarrow{H_{ıs}} = \frac{1}{4\pi} \iint_{s_2} \nabla \times \left[\overrightarrow{n_2} \times \overrightarrow{H_{\dot{1}}}\Big|_{s_2} \frac{e^{-jkR_2}}{R_2} \right] dS' + \frac{j\varepsilon\omega}{4\pi} \iint_{s_2} \overrightarrow{n_2} \times \overrightarrow{E_{\dot{1}}}\Big|_{s_2} \frac{e^{-jkR_2}}{R_2} dS', \tag{2.7}$$

and

$$\overrightarrow{H_{rs}} = \frac{1}{4\pi} \iint_{s_1} \nabla \times \left[\overrightarrow{n_1} \times \overrightarrow{H_t}\Big|_{s_1} \frac{e^{-jkR_1}}{R_1} \right] dS'. \tag{2.8}$$

The total electric field can be defined as

$$\overrightarrow{E_t} = \overrightarrow{E_{ıs}} + \overrightarrow{E_{rs}}, \tag{2.9}$$

where

$$\overrightarrow{E_{ıs}} = -\frac{j\mu_0\omega}{4\pi} \iint_{s_2} \overrightarrow{n_2} \times \overrightarrow{H_{\dot{1}}}\Big|_{s_2} \frac{e^{-jkR_2}}{R_2} dS' + \frac{1}{4\pi} \iint_{s_2} \nabla \times \left[\overrightarrow{n_2} \times \overrightarrow{E_{\dot{1}}}\Big|_{s_2} \frac{e^{-jkR_2}}{R_2} \right] dS', \tag{2.10}$$

and

$$\overrightarrow{E_{rs}} = -\frac{j\mu_0\omega}{4\pi} \iint_{s_1} \overrightarrow{n_1} \times \overrightarrow{H_t}\Big|_{s_1} \frac{e^{-jkR_1}}{R_1} dS'. \tag{2.11}$$

Here, $\overrightarrow{E_{is}}$ is incident scattered electric field. $\overrightarrow{E_{rs}}$ is reflected scattered electric field. $\overrightarrow{H_{is}}$ is incident scattered magnetic field. $\overrightarrow{H_{rs}}$ is reflected scattered magnetic field, [7].

CHAPTER 3

3. CYLINDRICAL PARABOLIC REFLECTOR ANTENNA

First of all, electric line source should be investigated. Cylindrical parabolic reflector will be fed from ELS. Which means that, electrical and magnetic fields radiated by cylindrical parabolic reflector antenna will come from ELS. It is shown in Figure 5, [9].

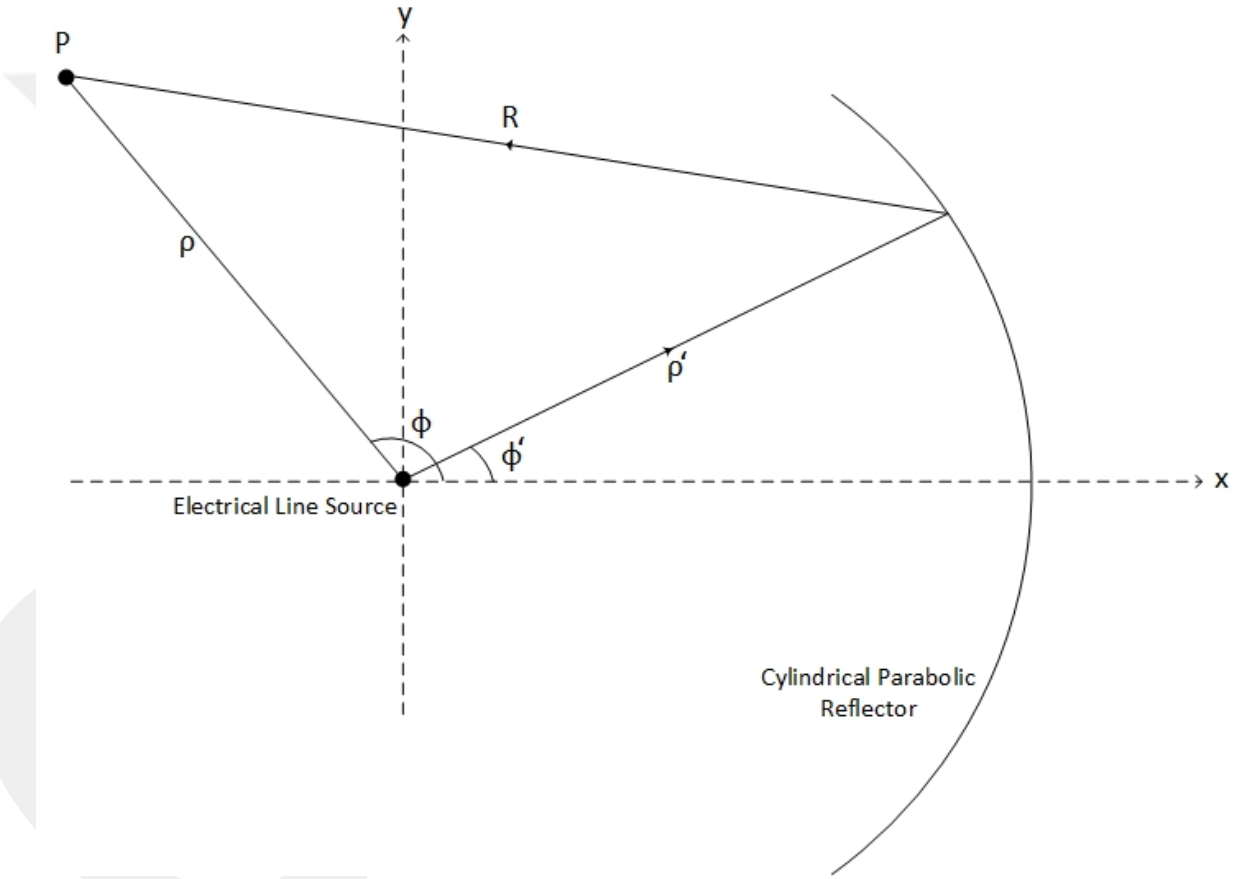

Figure 5. Geometry of the electric line source

Here, expression of the electric line source's electrical field can be written as [9]

$$\overrightarrow{E_{els}} = \overrightarrow{e_z} e^{j(\frac{\pi}{4})} \frac{\omega\mu_0 I_0}{2\sqrt{2\pi}} \frac{e^{-jk\rho}}{\sqrt{k\rho}} , \quad (3.1)$$

where

- ω: Angular frequency.
- μ_0: Permeability of free space.
- I_0: Source current.

Magnetic field can be found by using electrical field which has relation as

$$\overrightarrow{H_{els}} = -\frac{1}{j\omega\mu_0} \nabla \times \overrightarrow{E_{els}} . \quad (3.2)$$

Magnetic field of ELS can be expressed as

$$\overrightarrow{H_{els}} = \overrightarrow{e_\phi} e^{j(\frac{\pi}{4})} \frac{\omega\mu_0 I_0}{2\sqrt{2\pi}} \frac{1}{Z_0} \frac{e^{-jk\rho}}{\sqrt{k\rho}} . \quad (3.3)$$

- Z_0: impedance of free space

As said before, MTPO method has difference about normal vector from PO method. So, we have to define normal vector first. Normal vector is shown in Figure 6, [9].

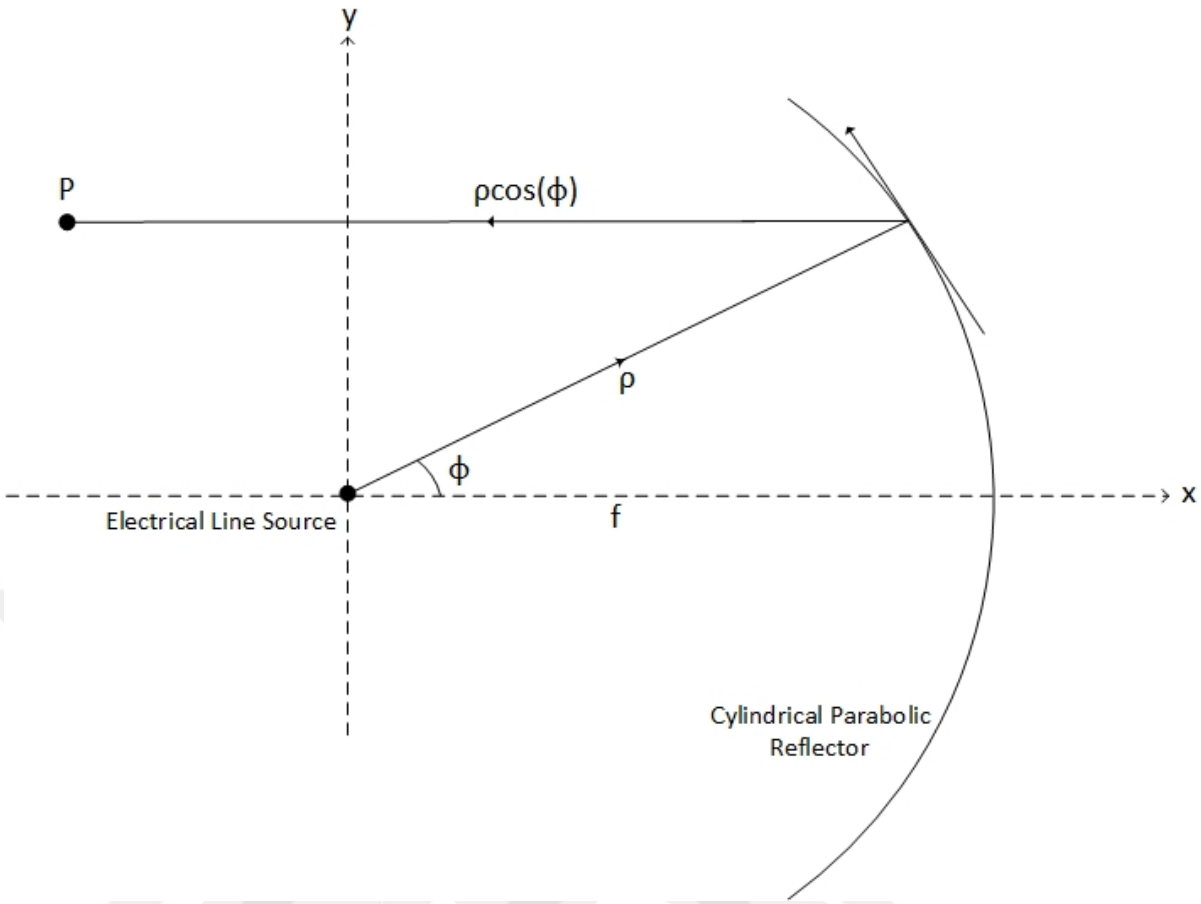

Figure 6. Geometry of normal vector

Focal length equation can be expressed as

$$\rho\cos(\phi) + \rho = 2f. \tag{3.4}$$

Normal vector can be calculated as

$$\vec{n} = \frac{\nabla\varphi}{\|\varphi\|}, \tag{3.5}$$

where

$$\varphi = 2f - \rho(\cos(\phi) + 1) = 0\,. \tag{3.6}$$

With using (3.5) and (3.6) we can obtain normal vector as

$$\vec{n} = -\cos\left(\frac{\phi'}{2}\right)\overrightarrow{e_\rho} + \sin\left(\frac{\phi'}{2}\right)\overrightarrow{e_\phi}\,. \tag{3.7}$$

For using MTPO method, new normal vector should be found. New normal vector $\vec{n}_1$ is shown Figure 7.

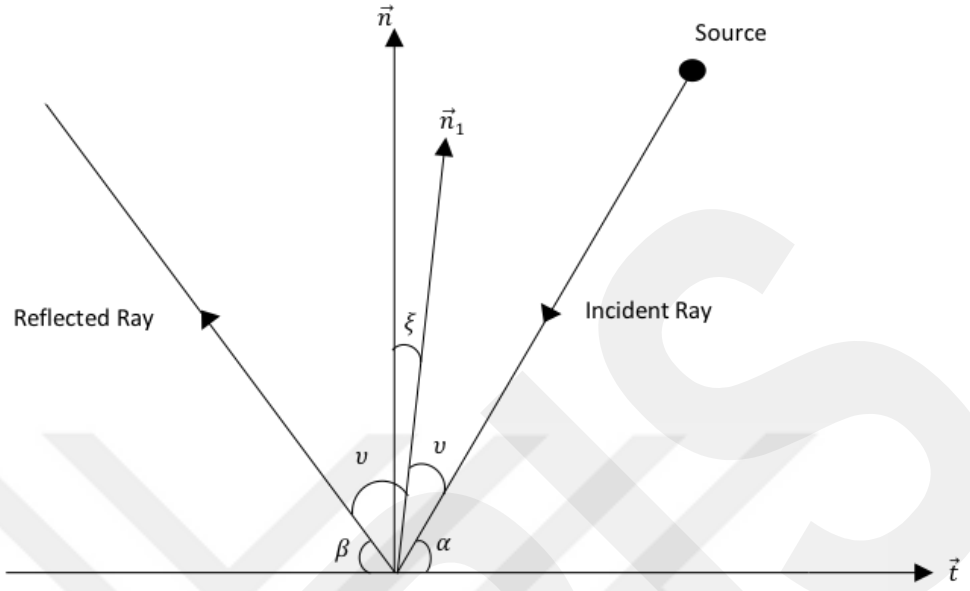

Figure 7. Geometry of new normal vector

The actual reflection event requires that angle of incidence which is angle between the incident ray and the normal vector is equal to $\frac{\Phi'}{2}$.

Parabola's tangential vector $\vec{t}$ can be expressed as

$$\vec{t} = \sin\left(\frac{\Phi}{2}\right)\overrightarrow{e_\rho} + \cos\left(\frac{\Phi}{2}\right)\overrightarrow{e_\phi}. \tag{3.8}$$

New normal vector at PEC surface can be written as

$$\begin{aligned} \vec{n}_1 &= \cos(\xi)\vec{n} + \sin(\xi)\vec{t}, \\ \alpha &= \frac{\pi}{2} - \frac{\Phi'}{2}, \\ \upsilon &= \frac{\pi}{2} - \frac{\alpha+\beta}{2}, \\ \xi &= \frac{\alpha-\beta}{2}. \end{aligned} \tag{3.9}$$

with substituting υ with (3.9), final form of new unit vector is defined as

$$\vec{n}_1 = \sin\left(\frac{\alpha+\beta}{2}\right)\overrightarrow{e_\rho} + \cos\left(\frac{\alpha+\beta}{2}\right)\overrightarrow{e_\phi} \ . \tag{3.10}$$

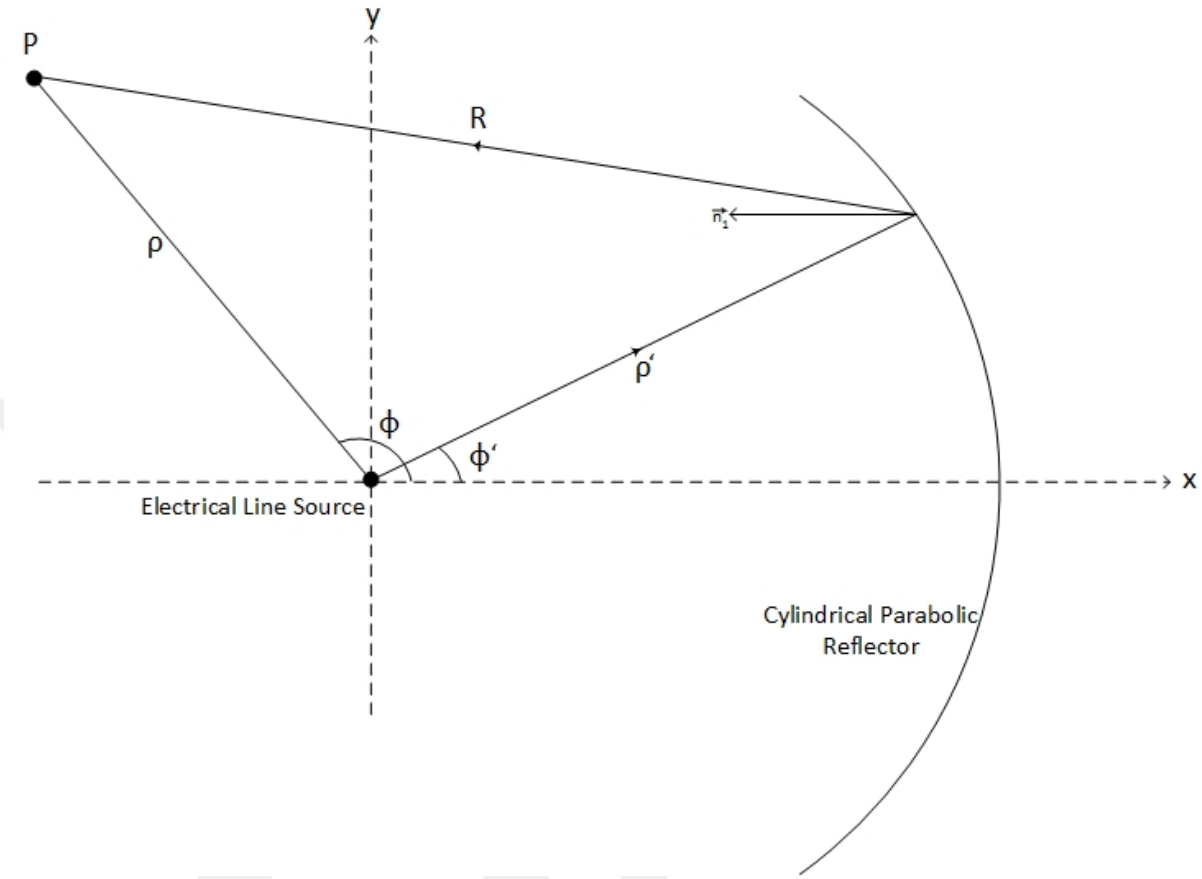

Figure 8. Geometry of cylindrical parabolic reflector antenna

MTPO surface current can be expressed as

$$\vec{J}_{MTPO} = 2\, e^{j\left(\frac{\pi}{4}\right)} \frac{\omega\mu_0 I_0}{2\sqrt{2\pi}} \frac{1}{Z_0} \frac{e^{-jk\rho}}{\sqrt{k\rho}} \sin\left(\frac{\alpha+\beta}{2}\right)\overrightarrow{e_z} \ . \tag{3.11}$$

Reflected scattered field could be expressed as

$$\vec{E}_{rs} = -e^{j\left(\frac{\pi}{4}\right)} \frac{\omega\mu_0 I_0}{2\sqrt{2\pi}} \frac{1}{Z_0} \frac{k\, e^{j\left(\frac{\pi}{4}\right)}}{\sqrt{2\pi}} \overrightarrow{e_z} \int_{-\phi_0}^{\phi_0} \sin\left(\frac{\alpha+\beta}{2}\right) \frac{e^{-jk\rho'}}{\sqrt{k\rho'}} \frac{e^{-jkR}}{\sqrt{kR}} \frac{\rho'}{\cos\frac{\Phi'}{2}} d\phi' \ . \tag{3.12}$$

New normal vector at aperture surface can be written as

$$\vec{n}_2 = \sin\left(\frac{\beta - \alpha}{2}\right)\overrightarrow{e_\rho} + \cos\left(\frac{\beta - \alpha}{2}\right)\overrightarrow{e_\phi} \ . \tag{3.13}$$

MTPO aperture surface current can be expressed as

$$\vec{J}_{AMTPO} = 2\, e^{j(\frac{\pi}{4})} \frac{\omega\mu_0 I_0}{2\sqrt{2\pi}} \frac{1}{Z_0} \frac{e^{-jk\rho}}{\sqrt{k\rho}} \sin\left(\frac{\beta - \alpha}{2}\right)\overrightarrow{e_z} \ . \tag{3.14}$$

Incident scattered field could be expressed as

$$\vec{E}_{is} = e^{j(\frac{\pi}{4})} \frac{\omega\mu_0 I_0}{2\sqrt{2\pi}} \frac{1}{Z_0} \frac{k\, e^{j(\frac{\pi}{4})}}{\sqrt{2\pi}}\overrightarrow{e_z} \int_{-\phi_0}^{\phi_0} \sin\left(\frac{\beta - \alpha}{2}\right) \frac{e^{-jk\rho'}}{\sqrt{k\rho'}} \frac{e^{-jkR}}{\sqrt{kR}} \frac{\rho'}{\cos\frac{\phi'}{2}} d\phi' \ . \tag{3.15}$$

Total scattered field is shown as

$$\vec{E}_s = \vec{E}_i + \vec{E}_{is} + \vec{E}_{rs} \ . \tag{3.16}$$

After finding integral of scattering fields, these integrals are solved asymptotically. For solving these integral, geometry of parabola examines clearly in Figure 4.

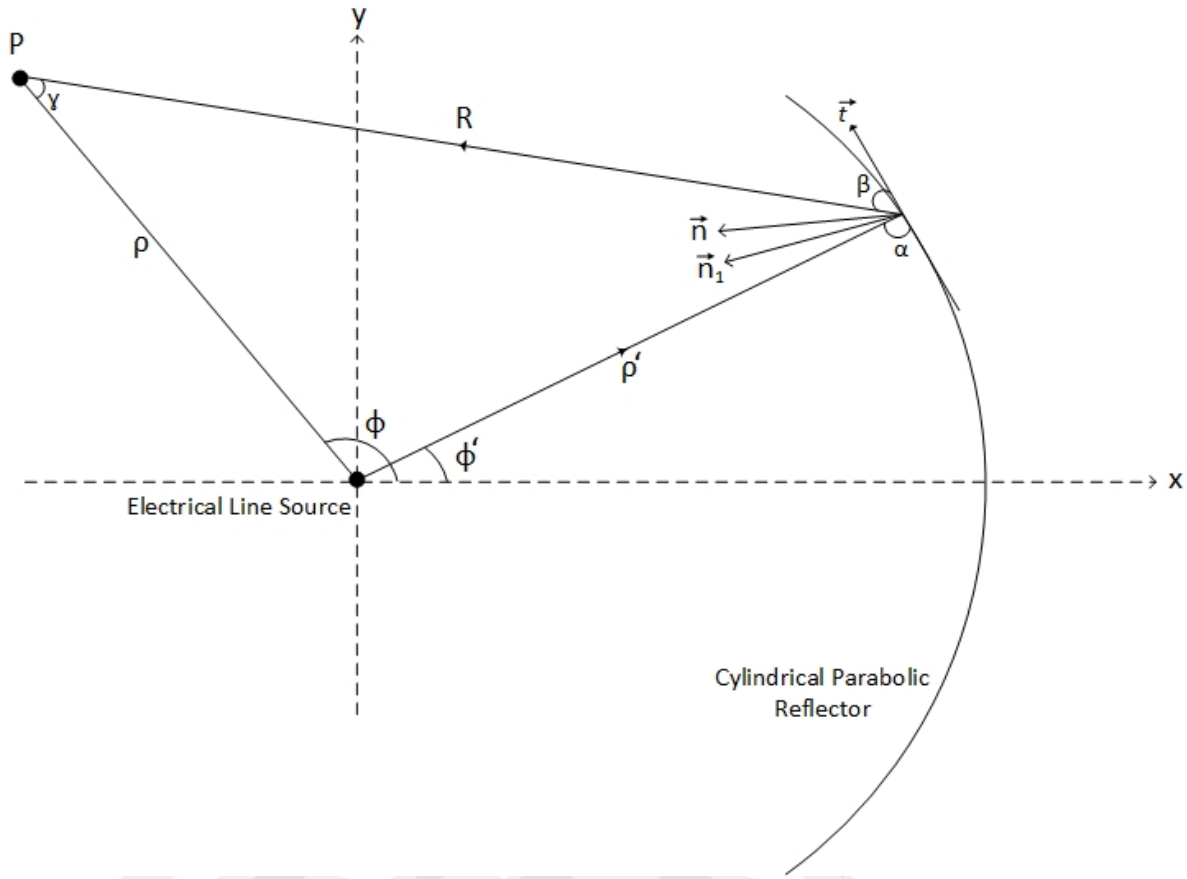

Figure 9. Geometry of parabola

$$\gamma + \phi - \phi' = \alpha + \beta\,, \tag{3.17}$$

$$\frac{d\gamma}{d\phi'} = \frac{d\alpha}{d\phi'} + \frac{d\beta}{d\phi'} - 1, \tag{3.18}$$

$$\frac{d\alpha}{d\phi'} = \frac{\pi}{2} - \frac{\phi'}{2}. \tag{3.19}$$

By using sinus theorem

$$\frac{R}{\sin(\phi - \phi')} = \frac{\rho}{\sin(\alpha + \beta)} = \frac{\rho'}{\sin(\gamma)}\,, \tag{3.20}$$

$$\rho' \sin(\alpha + \beta) = \rho \sin(\gamma), \tag{3.21}$$

Also,

$$R = \rho \cos(\gamma) - \rho' \cos(\alpha + \beta). \tag{3.22}$$

In this study, stationary phase method will be used for evaluating scattering integral asymptotically. The phase function of scattering integral is shown as

$$g(\phi') = \rho' + R. \tag{3.23}$$

This equation can be spread as

$$g(\phi') = \rho'(1 + \cos(\alpha + \beta)) - \rho \cos(\gamma). \tag{3.24}$$

First derivative of phase function of scattering integral can be expressed as

$$g'(\phi') = \rho' \frac{\cos\alpha}{\sin\alpha} [1 + \cos(\alpha + \beta)] + \sin(\alpha + \beta)\rho' \left[\frac{d\alpha}{d\phi'} + \frac{d\beta}{d\phi'}\right] - \rho \sin(\gamma) \frac{d\gamma}{d\phi'}. \tag{3.25}$$

With using (3.17),(3.18),(3.19),

$$g'(\phi') = \rho' \frac{\cos\alpha}{\sin\alpha} [1 - \cos(\alpha + \beta)] + \sin(\alpha + \beta)\rho' - 1. \tag{3.26}$$

Formula at (3.26) can be formed as

$$g'(\phi') = \frac{\rho'}{\sin\alpha} [\cos(\alpha) - \cos(\alpha)\cos(\alpha + \beta)] - \sin(\alpha)\sin(\alpha + \beta). \tag{3.27}$$

The final form of first derivative of phase function of scattering integral is shown as

$$g'(\phi') = \frac{\rho'}{\sin\alpha} [\cos(\alpha) - \cos(\beta)] \ . \tag{3.28}$$

Stationary phase point can be found with using $g'(\phi') = 0$ equation. And stationary phase points for reflection and transmission respectively can be expressed respectively as

$$\beta_{sr} = \alpha \ , \qquad \beta_{tr} = -\alpha \ . \tag{3.29}$$

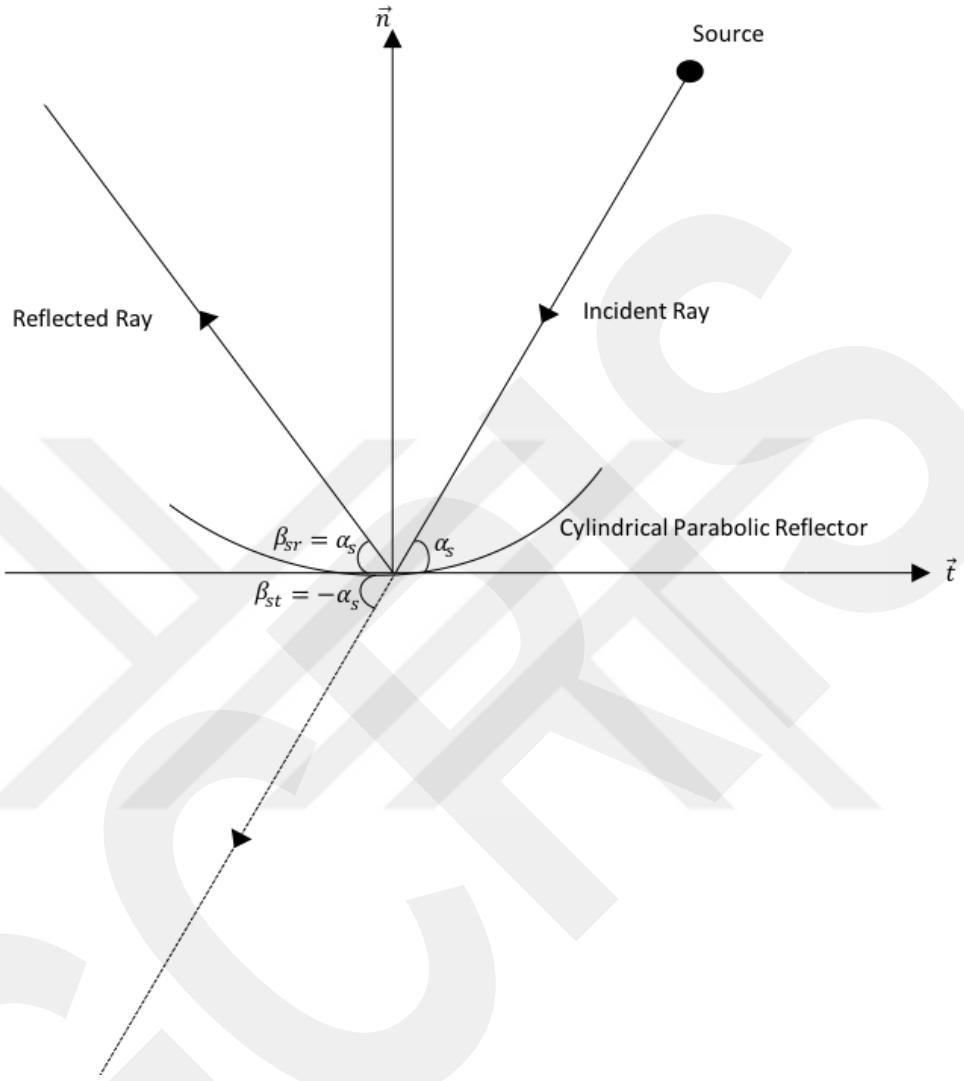

Figure 10. Geometry of stationary phase

The second derivative of phase function of scattering integral is shown as

$$g''(\phi') = \frac{d}{d\phi'}\left(\frac{\rho'}{\sin(\alpha)}\right)[\cos(\alpha) - \cos(\beta)] - \frac{\rho'}{\sin(\alpha)}\left[-\sin(\alpha)\frac{d\alpha}{d\phi'} + \sin(\beta)\frac{d\beta}{d\phi'}\right]. \tag{3.30}$$

$\frac{d\beta}{d\phi'}$ can be found from (3.21) as,

$$\rho' \frac{\cos(\alpha)}{\sin(\alpha)} \sin(\alpha+\beta) + \rho' \cos(\alpha+\beta)\left[\frac{d\alpha}{d\phi'} + \frac{d\beta}{d\phi'}\right] = \rho \cos(\gamma) \frac{d\gamma}{d\phi'} \ , \qquad (3.31)$$

By using eqn.(3.18) and (3.22),

$$\frac{d\beta}{d\phi'} = \frac{\rho' \cos(\alpha) \sin(\alpha+\beta) - \rho \cos(\gamma) \sin(\alpha)}{R \sin(\alpha)} + \frac{1}{2} \ . \qquad (3.32)$$

For reflected stationary phase point $\beta_{sr} = \alpha$, Taylor series expansion can be expressed as

$$\varphi(\phi') = \rho'_s + R_S + \frac{\rho_s'^{\,2}}{2R_S} (\phi' - \phi'_s)^2 \ . \qquad (3.33)$$

where

- ρ'_s : stationary phase value of ρ'.
- R_S: stationary phase value of R .
- ϕ'_s: stationary phase value of ϕ'.

The scattering integral can be expressed as

$$\vec{E}_t = -e^{j\left(\frac{\pi}{4}\right)} \frac{\omega\mu_0 I_0}{2\sqrt{2\pi}} \frac{1}{Z_0} \frac{k\, e^{j\left(\frac{\pi}{4}\right)}}{\sqrt{2\pi}} \frac{e^{-jk(\rho'_s + R_S)}}{\sqrt{kR_S}\sqrt{k\rho'_s}} \overrightarrow{e_z} \int_{-\phi_0}^{\phi_0} e^{-jk\frac{\rho_s'^{\,2}}{2R_S}(\phi' - \phi'_s)^2} d\phi' \quad . \qquad (3.34)$$

By using error function which is defined in (6.20), equation can be written as

$$E_{sr}^{GO} = -e^{j\left(\frac{\pi}{4}\right)} \frac{\omega\mu_0 I_0}{2\sqrt{2\pi}} \frac{e^{-jk\rho'_s}}{\sqrt{k\rho'_s}} e^{-jkR_S} \ . \qquad (3.35)$$

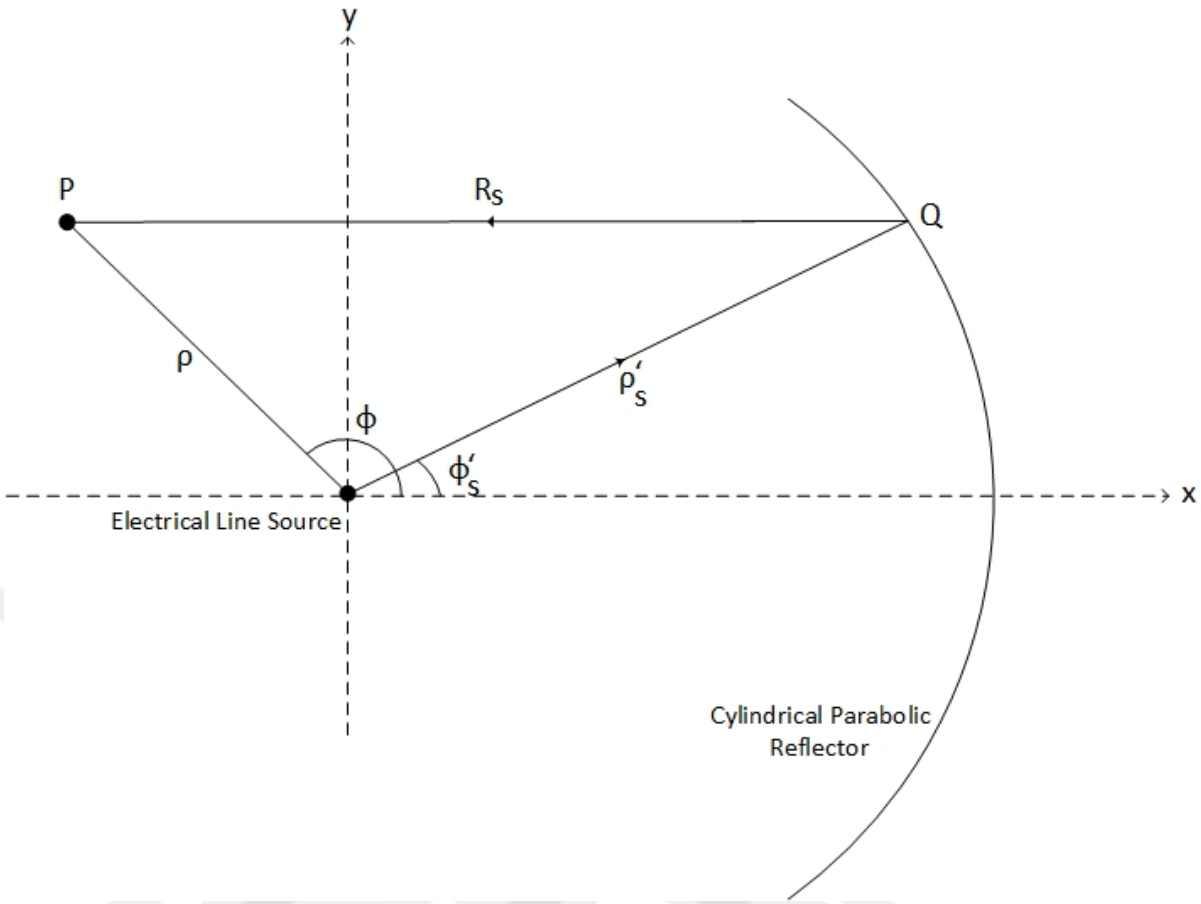

Figure 11. Stationary phase point reflection geometry

For transmitted stationary phase point $\beta_{sr} = -\alpha$ and $\phi = \phi_s'$, Taylor series expansion can be expressed as

$$\varphi(\phi') = \rho + \frac{\rho\rho_s}{2R_{2S}} (\phi' - \phi_s')^2 , \tag{3.36}$$

where

- ρ_s' : stationary phase value of ρ'.
- R_{2S}: stationary phase value of R .
- ϕ_s': stationary phase value of ϕ'.

The scattering integral can be expressed as

$$\vec{E}_t = -e^{j\left(\frac{\pi}{4}\right)} \frac{\omega\mu_0 I_0}{2\sqrt{2\pi}} \frac{1}{Z_0} \frac{k\, e^{j\left(\frac{\pi}{4}\right)}}{\sqrt{2\pi}} \frac{e^{-jk\rho}}{\sqrt{k\rho}} \vec{e_z} \int_{-\phi_0}^{\phi_0} e^{-jk\frac{\rho\rho_s}{2R_{2S}}(\phi'-\phi_s')^2} d\phi' \quad . \tag{3.37}$$

By using error function, equation can be written as

$$E_{st}^{GO} = e^{j(\frac{\pi}{4})} \frac{\omega\mu_0 I_0}{2\sqrt{2\pi}} \frac{e^{-jk\rho}}{\sqrt{k\rho}} [U(\phi - \phi_0) - U(\phi - 2\pi + \phi_0)] \ . \quad (3.38)$$

Geometrical Theory of Diffraction [8] coefficient can be written as

$$E_d = -\frac{e^{-j(\frac{\pi}{4})}}{2\sqrt{2\pi}} \left[\frac{1}{\cos\frac{\phi - \phi_0}{2}} - \frac{1}{\cos\frac{\phi + \phi_0}{2}} \right] \frac{e^{-jk\rho}}{\sqrt{k\rho}} E_i(Q_e) \ . \quad (3.39)$$

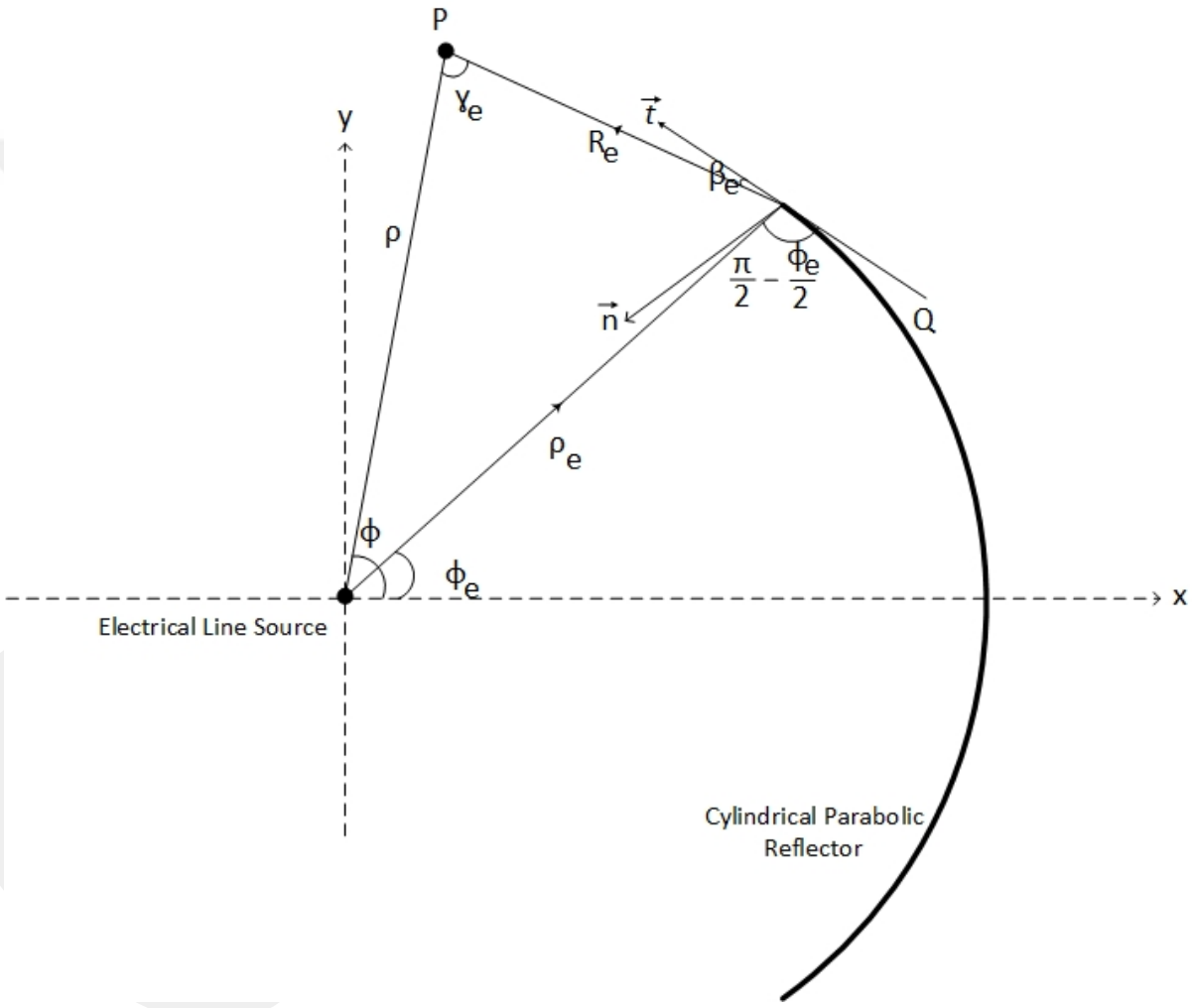

Figure 12. Geometry of edge point diffraction

β_e can be written as

$$\beta_e = \sin^{-1} \frac{\rho \sin(\phi - \phi_e)}{R_e} - \frac{\phi_e}{2}. \quad (3.40)$$

And R_e can be expressed as

$$R_e = \sqrt{\rho^2 + \rho_e^2 - 2\rho\rho_e \cos(\phi - \phi_e)}. \tag{3.41}$$

ρ_e is shown as

$$\rho_e = \frac{f}{\cos^2(\frac{\phi_e}{2})}. \tag{3.42}$$

The edge diffracted can be shown as

$$E_d = -\frac{\omega\mu_0 I_0}{8\pi}\left[\frac{1}{\sin\frac{\beta_e - \alpha_e}{2}} - \frac{1}{\sin\frac{\beta_e + \alpha_e}{2}}\right]\frac{e^{-jk(\rho_e + R_e)}}{k\sqrt{\rho_e R_e}}. \tag{3.43}$$

With using trigonometric expression shown below as

$$\sin^2(x) = \frac{1}{2}(1 - \cos(2x)) \ . \tag{3.44}$$

Substituting x with $\frac{\beta_e \pm \alpha_e}{2}$,

$$1 = 2\sin^2\left(\frac{\beta_e \pm \alpha_e}{2}\right) + \cos(\beta_e \pm \alpha_e), \tag{3.45}$$

Also,

$$e^{-jk\rho_e} = e^{-jk\rho_e 2\sin^2\left(\frac{\beta_e \pm \alpha_e}{2}\right)} e^{-jk\rho_e \cos(\beta_e \pm \alpha_e)} \ . \tag{3.46}$$

Diffracted fields can be expressed for making uniform by using (3.46) as

$$E_d = -\frac{\omega\mu_0 I_0}{8\pi}\left[e^{-jk\rho_e \cos(\beta_e - \alpha_e)}\frac{e^{-jk\rho_e 2\sin^2\left(\frac{\beta_e - \alpha_e}{2}\right)}}{\sin\frac{\beta_e - \alpha_e}{2}} - e^{-jk\rho_e \cos(\beta_e + \alpha_e)}\frac{e^{-jk\rho_e 2\sin^2\left(\frac{\beta_e + \alpha_e}{2}\right)}}{\sin\frac{\beta_e + \alpha_e}{2}}\right] \times \frac{e^{-jkR_e}}{k\sqrt{\rho_e R_e}}, \tag{3.47}$$

$$E_{id} = -\frac{\omega\mu_0 I_0 e^{j\left(\frac{\pi}{4}\right)}}{2\sqrt{2\pi}} e^{-jk\rho_e \cos(\beta_e - \alpha_e)} \left[\frac{e^{-j\left(\frac{\pi}{4}\right)} e^{-jk\rho_e 2\sin^2\left(\frac{\beta_e - \alpha_e}{2}\right)}}{2\sqrt{\pi}\sqrt{2k\rho_e}\sin\frac{\beta_e - \alpha_e}{2}}\right] \frac{e^{-jkR_e}}{\sqrt{kR_e}}, \quad (3.48)$$

$$E_{rd} = \frac{\omega\mu_0 I_0 e^{j\left(\frac{\pi}{4}\right)}}{2\sqrt{2\pi}} e^{-jk\rho_e \cos(\beta_e + \alpha_e)} \left[\frac{e^{-j\left(\frac{\pi}{4}\right)} e^{-jk\rho_e 2\sin^2\left(\frac{\beta_e + \alpha_e}{2}\right)}}{2\sqrt{\pi}\sqrt{2k\rho_e}\sin\frac{\beta_e + \alpha_e}{2}}\right] \frac{e^{-jkR_e}}{\sqrt{kR_e}}. \quad (3.49)$$

Detour parameters can be written as

$$\zeta_i = \sqrt{2k\rho_e}\sin\frac{\beta_e - \alpha_e}{2}, \quad (3.50)$$

$$\zeta_r = \sqrt{2k\rho_e}\sin\frac{\beta_e + \alpha_e}{2}. \quad (3.51)$$

Uniform diffracted fields can be expressed with using Fresnel function as

$$E_d = \frac{\omega\mu_0 I_0 e^{j\left(\frac{\pi}{4}\right)}}{2\sqrt{2\pi}} \frac{e^{-jkR_e}}{\sqrt{kR_e}} \left[-e^{-jk\rho_e \cos(\beta_e - \alpha_e)}\hat{F}(\zeta_i) + e^{-jk\rho_e \cos(\beta_e + \alpha_e)}\hat{F}(\zeta_r)\right], \quad (3.52)$$

And also

$$\hat{F}(x) = \text{sign}(x)F[|x|]. \quad (3.53)$$

Fresnel function is defined in Section 6.3.1.

3.1.Reflected Fields from Cylindrical Parabolic Reflector Antenna

Reflected field for MTPO integral is expressed in (3.12). Reflected field for PO Method can be calculated as

$$\vec{E}_{rs} = -e^{j\left(\frac{\pi}{4}\right)} \frac{\omega\mu_0 I_0}{2\sqrt{2\pi}} \frac{1}{Z_0} \frac{k\, e^{j\left(\frac{\pi}{4}\right)}}{\sqrt{2\pi}} \vec{e_z} \int_{-\phi_0}^{\phi_0} \sin(\alpha) \frac{e^{-jk\rho}}{\sqrt{k\rho}} \frac{e^{-jkR}}{\sqrt{kR}} \frac{\rho'}{\cos\frac{\phi'}{2}} d\phi' \quad . \quad (3.54)$$

Simulations are done for $\phi_0 = 45°$,$\rho = 9333$km, $\lambda = 0.03$m. Reflected field is shown in Figure 13.

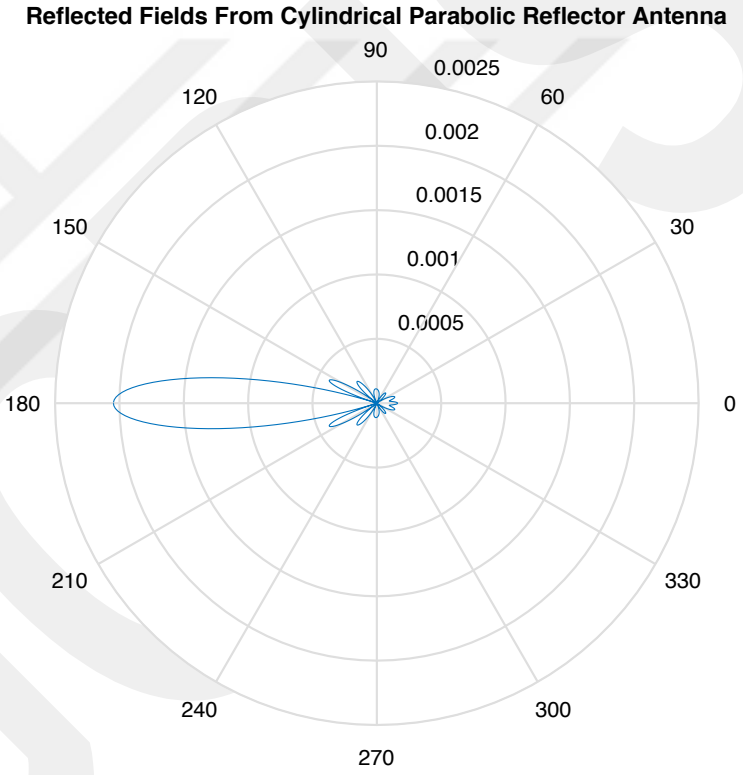

Figure 13. Reflected field from cylindrical parabolic reflector antenna

Whole path considered in simulations. However, attenuation is not considered. It will be considered in Section 8.1. Directivity of the CPRA's is shown well in the Figure 13. Comparison between MTPO and PO methods is shown in Figure 14.

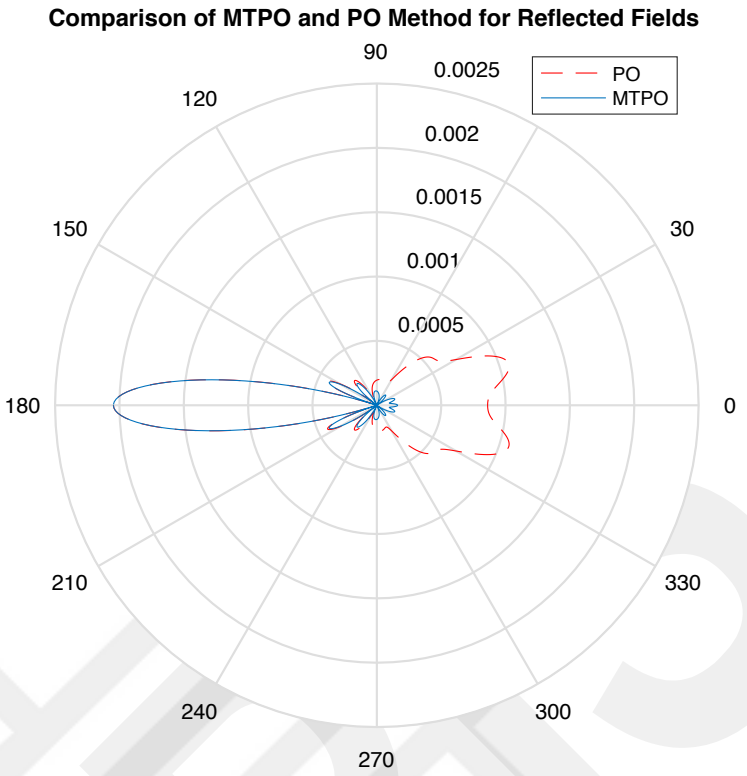

Figure 14. Comparison of MTPO and PO method

As in Section 2, MTPO method and PO method difference is investigated for cylindrical parabolic reflector antenna (CPRA). There is harmony between MTPO and PO method for $\phi \in \left[\frac{\pi}{2}, \frac{3\pi}{2}\right]$. Difference between MTPO and PO methods is investigating for $\phi \in \left[-\frac{\pi}{2}, \frac{\pi}{2}\right]$. PO method includes transmitted scattered fields because of that reflection part of PO integral(3.54) is not equal to 0 at $\beta_s = -\alpha_s$.

CHAPTER 4

4. MODELLING CPRA'S REFLECTED FIELD AS GAUSSIAN BEAM

In this section of thesis, gaussian beam is investigated. CPRA's reflected field will be modeled as Gaussian beam incident GO waves. Scattered fields of Gaussian beam are researched for resistive half screen by Umul, [24]. Umul is used far field approximation method for in order to find geometrical optics and diffracted waves.

Complex point source approach is used to model Gaussian beam, [78]. Figure 15 is the general view for modeling CPRA's reflected field as Gaussian beam.

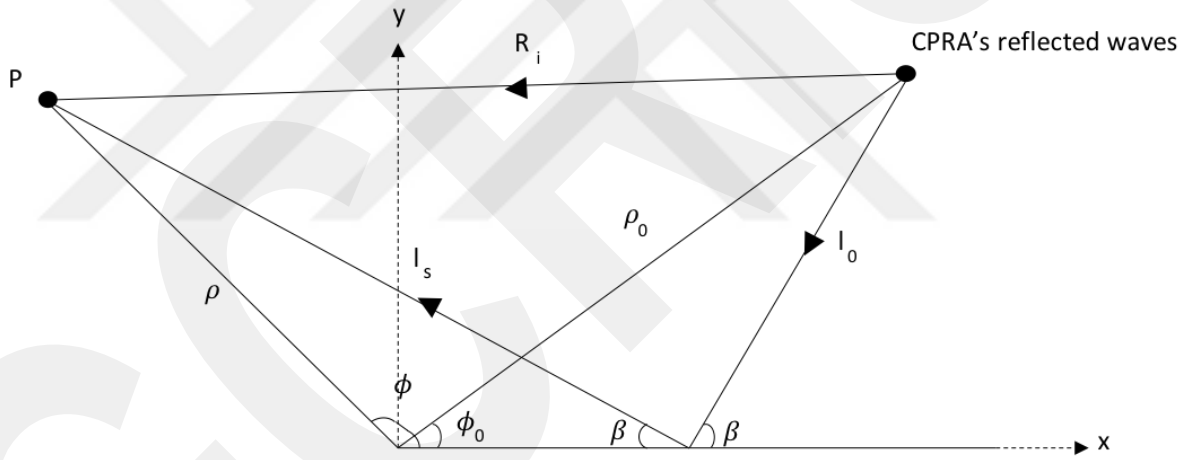

Figure 15. Geometry of the CPRA'S reflected wave diffraction by resistive half-plane, [24].

The complex point source view is shown in Figure 16.

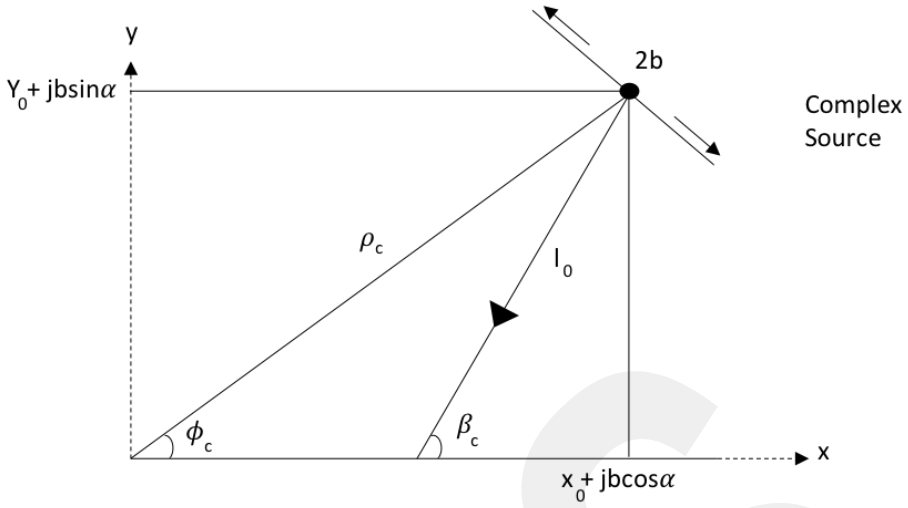

Figure 16. Geometry of complex point source, [24].

In the Umul's journal [24], incident field is taken as line source instead of CPRA's reflected scattered fields. It is shown as

$$U_i = \frac{e^{-jk\,R_i}}{\sqrt{k\,R_i}}. \tag{4.1}$$

R_i and R_r which are distance between source and half plane and distance between image source and observation point respectively can be written as

$$\begin{aligned} R_i &= \sqrt{\rho^2 + {\rho_0}^2 - 2\rho\rho_0\cos(\phi - \phi_0)}, \\ R_r &= \sqrt{\rho^2 + {\rho_0}^2 - 2\rho\rho_0\cos(\phi + \phi_0)}. \end{aligned} \tag{4.2}$$

Then, Umul used far-field approximation. Distance formula can be expressed as

$$\begin{aligned} R_i &\approx \rho - \rho_0\cos(\phi - \phi_0), \\ R_r &\approx \rho - \rho_0\cos(\phi + \phi_0). \end{aligned} \tag{4.3}$$

Umul was first investigated the scattering of line source by resistive half-plane, [24]. GO waves can be written as

$$\begin{aligned} U_{GO} = U_0\frac{e^{jk\rho}}{\sqrt{k\rho}}\Big[e^{jk\rho_0 cos(\emptyset-\emptyset_0)}\ \Big[U(-\zeta_i) + \frac{\sin(\beta)}{\sin(\beta)+\sin(\theta)}U(\zeta_i)\Big] \\ - \frac{\sin(\theta)}{\sin(\beta)+\sin(\theta)}e^{jk\rho_0 cos(\emptyset+\emptyset_0)}U(-\zeta_r)\Big], \end{aligned} \tag{4.4}$$

Where

$$\begin{aligned}\zeta_r &= -2\sqrt{\frac{k\rho\rho_0}{\rho+\rho_0+R_r}}\cos\left(\frac{\emptyset+\emptyset_0}{2}\right),\\ \zeta_i &= -2\sqrt{\frac{k\rho\rho_0}{\rho+\rho_0+R_i}}\cos\left(\frac{\emptyset-\emptyset_0}{2}\right).\end{aligned} \tag{4.5}$$

Then he expressed uniform diffracted fields for resistive half plane as

$$\begin{aligned}&U_d\\ &= \frac{K(\emptyset,\theta)K(\emptyset_0,\theta)}{\sin(\emptyset_0)}\left[\sin\left(\frac{\emptyset-\emptyset_0}{2}\right)\sqrt{\frac{2R_i}{\rho+\rho_0+R_i}}\frac{e^{-jk\,R_i}}{\sqrt{k\,R_i}}sign(\zeta_i\ \ )F(|\zeta_i\ \ |)\right.\\ &\left.-\sin\left(\frac{\emptyset+\emptyset_0}{2}\right)\sqrt{\frac{2R_r}{\rho+\rho_0+R_r}}\frac{e^{-jk\,R_r}}{\sqrt{k\,R_r}}sign(\zeta_r\ \ )F(|\zeta_r\ \ |)\right],\end{aligned} \tag{4.6}$$

Where

$$\begin{aligned}K(\gamma,\theta) = &\frac{4\sqrt{\sin(\theta)}\sin\left(\frac{\gamma}{2}\right)}{\left[1+\sqrt{2}\cos\left(\frac{\frac{\pi}{2}-\gamma+\theta}{2}\right)\right]\left[1+\sqrt{2}\cos\left(\frac{\frac{3\pi}{2}-\gamma-\theta}{2}\right)\right]}x\\ &\left[\frac{\psi_n\left(\frac{3\pi}{2}-\gamma-\theta\right)\psi_n\left(\frac{\pi}{2}-\gamma+\theta\right)}{\left[\psi_n\left(\frac{\pi}{2}\right)\right]^2}\right]^2,\end{aligned} \tag{4.7}$$

And ψ_n is the Malyughinetz funtion [79] which is

$$\psi_n(x) = e^{-\frac{1}{8\pi}\int_0^x(\pi\sin(v)-2\sqrt{2\pi}\sin\left(\frac{v}{2}\right)+2v)/(\cos(v))\partial v}. \tag{4.8}$$

Here $\sin(\theta)$ is equal to Z_0/R_e. R_e is surface resistivity and Z_0 is free space impadence.

Then, Umul expressed the beam diffraction equations. Direct path distance and reflected path distance can be expressed as [24]

$$R_i = \sqrt{\rho^2 + {\rho_0}^2 - b^2 - 2\rho\rho_0\cos(\phi - \phi_0) - j2\rho b\cos(\phi - \alpha) + j2\rho_0 b\cos(\phi_0 - \alpha)},$$
$$R_r = \sqrt{\rho^2 + {\rho_0}^2 - b^2 - 2\rho\rho_0\cos(\phi + \phi_0) - j2\rho b\cos(\phi + \alpha) + j2\rho_0 b\cos(\phi_0 + \alpha)}. \quad (4.9)$$

Far field approximation is used. And distance equations are becoming as

$$R_i = \rho - \rho_0\cos(\phi - \phi_0) - jb\cos(\phi - \alpha),$$
$$R_r = \rho - \rho_0\cos(\phi + \phi_0) - jb\cos(\phi + \alpha). \quad (4.10)$$

Geometrical optic waves can be expressed as [24]

$$U_{GO} = U_{iGO} + U_{tGO} + U_{rGO}, \quad (4.11)$$

where

$$U_{iGO} = U_0\frac{e^{-jk\rho}}{\sqrt{k\rho}}e^{-jk\rho_0\cos(\phi-\phi_0)}e^{-kb\cos(\phi-\alpha)}U(-S_i),$$
$$U_{tGO} = U_0\frac{e^{-jk\rho}}{\sqrt{k\rho}}e^{-jk\rho_0\cos(\phi-\phi_0)}e^{-kb\cos(\phi-\alpha)}U(S_i)\frac{\sin(\beta_c)}{\sin(\beta_c)+\sin(\theta)}, \quad (4.12)$$
$$U_{rGO} = U_0\frac{e^{-jk\rho}}{\sqrt{k\rho}}e^{-jk\rho_0\cos(\phi+\phi_0)}e^{-kb\cos(\phi+\alpha)}U(-S_r)\frac{\sin(\theta)}{\sin(\beta_c)+\sin(\theta)},$$

and

$$\beta_c = \sin^{-1}\left(\frac{\rho\sin(\phi) + \rho_0\sin(\phi_0) + jbsin(\alpha)}{\sqrt{\rho^2 + {\rho_0}^2 - b^2 - 2\rho\rho_0\cos(\phi + \phi_0) - j2\rho b\cos(\phi + \alpha) + j2\rho_0 b\cos(\phi_0 + \alpha)}}\right). \quad (4.13)$$

$$S_{i,r} = Re(\zeta_{i,r}) - Im(\zeta_{i,r}).$$

Uniform diffracted fields are expressed by Umul [24] as

$$U_{id} = \frac{K(\emptyset,\theta)K(\pi-\emptyset_c,\theta)}{\sin(\emptyset_c)}\sin\left(\frac{\emptyset-\emptyset_c}{2}\right)\frac{e^{-jk\rho}}{\sqrt{k\rho}}e^{-jk\rho_0\cos(\phi-\phi_0)}e^{-kb\cos(\phi-\alpha)}x \quad (4.14)$$
$$sign(S_i)F(|S_i| + sign(S_i)\gamma_i),$$

U_{rd}

$$= -\frac{K(\emptyset,\theta)K(\pi-\emptyset_c,\theta)}{\sin(\emptyset_c)}\sin\left(\frac{\emptyset+\emptyset_c}{2}\right)\frac{e^{-jk\,\rho}}{\sqrt{k\,\rho}}\mathrm{e}^{-\mathrm{jk}\rho_0\cos(\phi+\phi_0)}\mathrm{e}^{-\mathrm{kbcos}(\phi+\alpha)}x$$
$$sign(S_r)F(|S_r|+sign(S_r)\gamma_r),$$

where

$$\gamma_{i,r} = \sqrt{2}\,Im(\zeta_{,r})e^{\frac{j\pi}{4}},$$
$$\zeta_i = -\sqrt{2k\rho_c}\cos\left(\frac{\emptyset-\emptyset_c}{2}\right), \quad (4.15)$$
$$\zeta_r = -\sqrt{2k\rho_c}\cos\left(\frac{\emptyset+\emptyset_c}{2}\right).$$

In this thesis, incident GO wave of Gaussian beam will be used. The relationship of Gaussian beam and CPRA's reflected field can be shown in Figure 17. Parameters of simulation can be expressed as,

- $\lambda = 0.03$m,
- $\rho = 9333$km,
- $b = 7\lambda$,
- $\phi_0 = 45^\circ$,
- $\alpha = 0^\circ$.

α is taken as 0 for integrating Gaussian beam location and CPRA location.

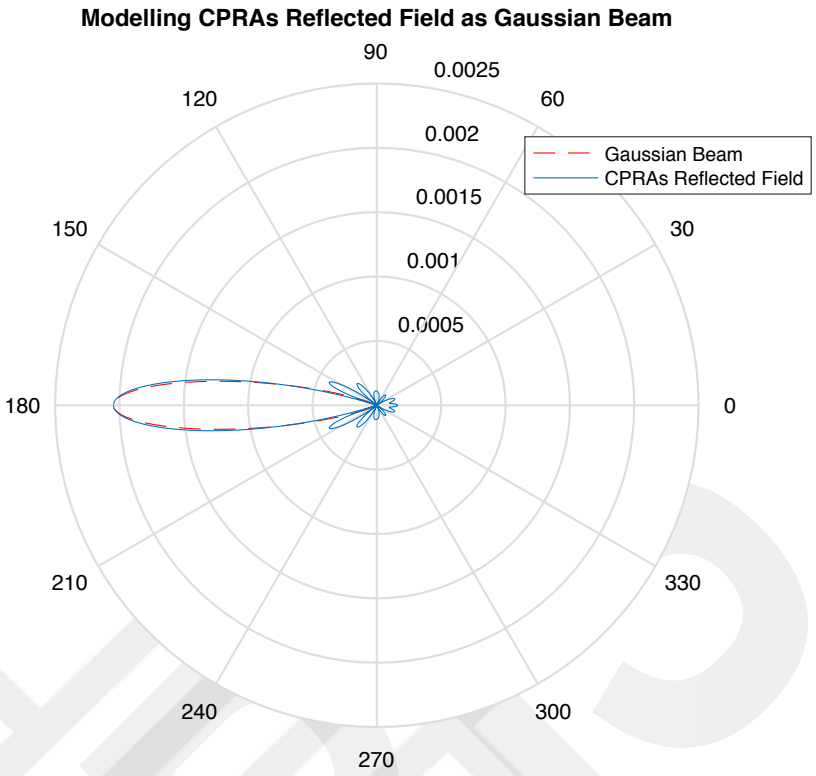

Figure 17. Gaussian beam model of CPRA's reflected field

The graph of electromagnetic wave which will pass through the atmosphere is shown in Figure 18. Parameters of simulation can be expressed as,

- $\lambda = 0.03\text{m}$,
- $\rho = 9333\text{km}$,
- $b = 7\lambda$,
- $\phi_0 = 60^\circ$,
- $\alpha = 45^\circ$.

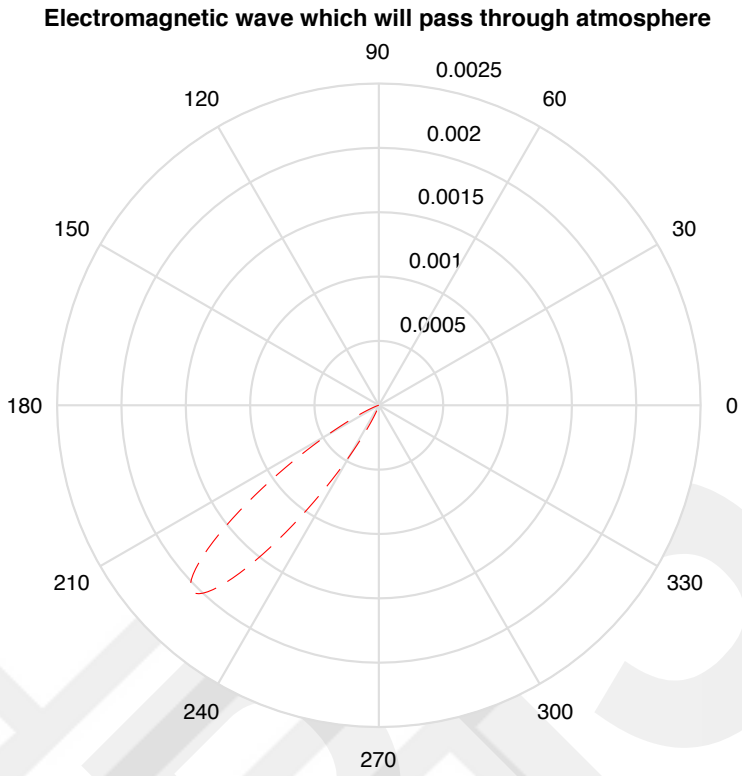

Figure 18. Electromagnetic wave which will pass through atmosphere

Perfect copy of CPRA's reflected field is evaluated with using Gaussian beam.

CHAPTER 5

5. RADIOWAVE PROPAGATION THROUGH SATELLITE TO TARGET

Radiated fields from satellite face impairments on way to plane. Variation of amplitude, phase, and polarization can be caused by these impairments. Frequency of radiowave has significant importance about radiowave propagation through atmosphere. Impairments which wave faces with is generally connected with radiowave's frequency. Radiowave propagation which will be used in this thesis should be chosen high enough to penetrate ionosphere which is the atmosphere layer extending from 15km to 400km. Ionosphere has 3 different layers inside it which are D, E, F layers. These layers can cause reflection and absorption at frequencies below 30 MHz. Reflection from ionosphere layers can be reduced by increasing frequency. Transparency of ionosphere is provided frequencies above 3 GHz with some exceptions, [5]. Ionosphere's magnetic permeability is 1.25664 x 10-6 H m-1 which is same with free space, [80]. Also, ionosphere's dielectric constant [81] can be found as

$$\epsilon_r = 1 - \frac{81N}{f^2}. \tag{5.1}$$

If frequency is chosen high enough, dielectric constant of ionosphere goes to 1. This means that permittivity of ionosphere and free space is same. This arguments about ionosphere proves that ionosphere is transparent at high frequencies.

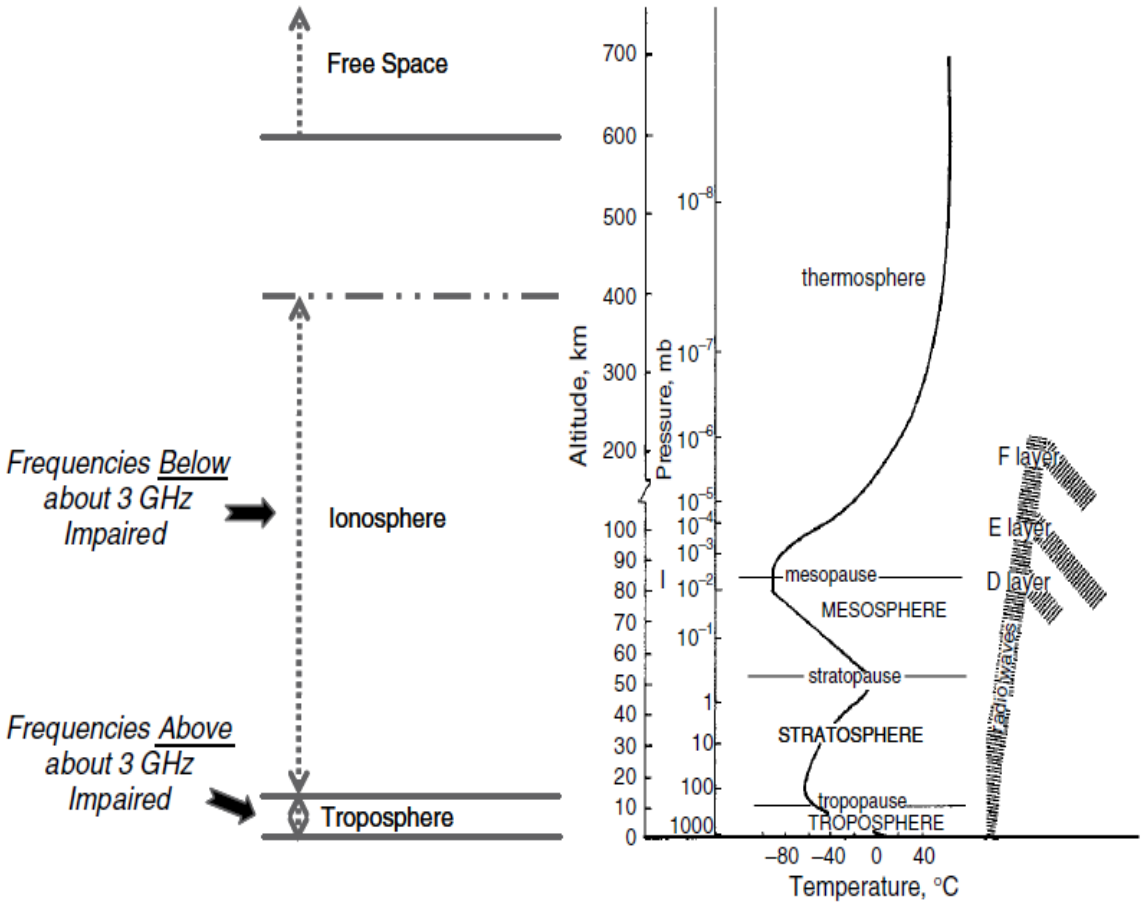

Figure 19. Impairments representations against frequencies taking from [5].

Satellite's link frequencies for most application are chosen above 3 GHz. In this thesis, radiowave frequency is chosen as 10 GHz. There will not be considered impairments below 3 GHz in this study. There are impairments, [25-54]. at Troposphere above 3 GHz. In this thesis, ITU-R standards has used for atmospheric model, [55-59]. Rainless medium is considered. Rain attenuation is neglected. 3 type of impairment will be considered which are gaseous attenuation, cloud attenuation and scintillation.

5.2.Atmospheric Gaseous Attenuation

Permanent dipolar molecules which effects radiowaves are contained by Atmosphere's gases. [86] Signal level's reduction which depends on frequency, temperature, pressure, and water vapor concentration is inevitable for radiowaves, [5]. This occurrence generally results with reduction at signal amplitude.

Components of atmosphere can be shown as [5]

• oxygen (21 %);

• nitrogen (78 %);

• argon (0.9 %);

• carbon dioxide (0.1 %);

• water vapor (variable, ∼1.7% at sea level and 100% relative humidity).

Two components which are oxygen and water vapors is the most dominant terms for Gaseous Attenuation in atmosphere, [4].

5.2.1. ITU-R Line-by-line Calculation for Gaseous Attenuation Model

Annex 1 of the ITU-R Recommendation ITU-R P.676-6 contains The line-by-line procedure, [59].

The procedure contains values for up to 1000 GHz with elevation angles 0 to 90°.

- p : dry air pressure (hPa)
- e : water vapor partial pressure (hPa)
- T : air temperature (°K)
- B_p : barometric pressure
- ρ : water vapor density (g/m3).
- RH =relative humidity in %
- T_c : air temperature measured in °C
- $\theta_c : \frac{300}{(T_c+273.15)}$
- ɣ : specific attenuation
- $ɣ_0$: specific attenuation (dB/Km) value for dry air
- $ɣ_w$: specific attenuation (dB/Km) value for water vapor
- f : frequency (GHz)
- N''(f) : imaginary part of the frequency-dependent complex refractivity
- N_D''(f) : dry air continuum spectra

- N_W''(f) : wet continuum spectra
- S_i : the strength of the ith line
- F_i : line shape factor
- f_i : line frequency
- Δf : width of the line
- δ : correction factor
- d : width parameter for the Debye spectrum
- h : seal level
- θ : elevation angle
- n(H) : atmospheric radio refractive index calculated from pressure, temperature, and water-vapor pressure along the path using [87].
- h_{min} : minimum height
- a_1 and a_2 : path lengths
- δ_1 and δ_2 : layer thicknesses
- n_1 and n_2 : refractive indexes
- α_1 and α_2 : entry incidence angles
- β_1 and β_2 : exiting incidence angles
- r_1 , r_2 and r_3 : radius from the center of the earth to the layers
- γ_i : specific attenuation

Barometric pressure can be expressed as

$$B_p = p + e\ (hPa). \tag{5.2}$$

Water vapor partial pressure and dry air pressure are shown as

$$e = \frac{\rho\ T}{216.7}\ (hPa). \tag{5.3}$$

Water vapor density is

$$\rho = \frac{RH}{5.752}\ {\theta_c}^6\ 10^{(10-9.834\theta)}(hPa). \tag{5.4}$$

Specific attenuation is determined from

$$\gamma = \gamma_0 + \gamma_w = 0.1820\ N''(f), \tag{5.5}$$

$$N''(\mathrm{f}) = \sum_i S_i F_i + N_D''(f) + N_W''(f).$$

The line strength can be introduced as

$$\begin{aligned} S_i &= \mathrm{a}_1 \times 10^{-7}\, e\ \theta^3\ e^{[\mathrm{a}_2(1-\theta]}\ for\ oxygen, \\ S_i &= \mathrm{b}_1 \times 10^{-7}\, e\ \theta^{3.5}\ e^{[\mathrm{a}_2(1-\theta]}\ for\ water\ vapor. \end{aligned} \tag{5.6}$$

The Line-shape factor can be expressed as

$$\begin{aligned} F_i &= \frac{f}{f_i}\left[\frac{\Delta f - \delta(f_i - f)}{(f_i - f)^2 + \Delta f^2} + \frac{\Delta f - \delta(f_i + f)}{(f_i + f)^2 + \Delta f^2}\right], \\ \Delta f &= \mathrm{a}_3 \times 10^{-4}\left(p\,\theta^{(0.8-\mathrm{a}_4)} + 1.1\,e\,\theta\right)\ for\ oxygen, \\ \Delta f &= \mathrm{b}_3 \times 10^{-4}\left(p\,\theta^{(b_4)} + b_5\,e\,\theta^{(b_6)}\right)\ for\ water\ vapor. \end{aligned} \tag{5.7}$$

Correction factor can be estimated as

$$\begin{aligned} \delta &= (\mathrm{a}_5 + \mathrm{a}_6\theta) \times 10^{-4}\, p\ \theta^{0.8}\ for\ oxygen, \\ \delta &= 0\ for\ water\ vapor\ . \end{aligned} \tag{5.8}$$

$N_D''(\mathrm{f})$, dry air continuum spectra and $N_W''(\mathrm{f})$ wet continuum spectra are shown as

$$\begin{aligned} N_D''(f) = f\ p\ \ \theta^2 \Bigg[& \frac{6.14 \times 10^{-5}}{d\left(1 - \left[\frac{f}{d}\right]^2\right)} \\ & + 1.4 \times 10^{12}\left(1 - 1.2 \times 10^{-5} f^{1.5}\right) p\ \ \theta^{1.5} \Bigg], \\ N_W''(f) = f(3.570\,\theta^{7.5} e + 0.113p) e\,\theta^3 \times 10^{-7}. & \end{aligned} \tag{5.9}$$

a_1, a_2, b_1 and b_2 are listed table below

f_0	a_1	a_2	a_3	a_4	a_5	a_6
50.474238	0.94	9.694	8.60	0	1.600	5.520
50.987749	2.46	8.694	8.70	0	1.400	5.520
51.503350	6.08	7.744	8.90	0	1.165	5.520
52.021410	14.14	6.844	9.20	0	0.883	5.520
52.542394	31.02	6.004	9.40	0	0.579	5.520
53.066907	64.10	5.224	9.70	0	0.252	5.520
53.595749	124.70	4.484	10.00	0	−0.066	5.520
54.130000	228.00	3.814	10.20	0	−0.314	5.520
54.671159	391.80	3.194	10.50	0	−0.706	5.520
55.221367	631.60	2.624	10.79	0	−1.151	5.514
55.783802	953.50	2.119	11.10	0	−0.920	5.025
56.264775	548.90	0.015	16.46	0	2.881	−0.069
56.363389	1344.00	1.660	11.44	0	−0.596	4.750
56.968206	1763.00	1.260	11.81	0	−0.556	4.104
57.612484	2141.00	0.915	12.21	0	−2.414	3.536
58.323877	2386.00	0.626	12.66	0	−2.635	2.686
58.446590	1457.00	0.084	14.49	0	6.848	−0.647
59.164207	2404.00	0.391	13.19	0	−6.032	1.858
59.590983	2112.00	0.212	13.60	0	8.266	−1.413
60.306061	2124.00	0.212	13.82	0	−7.170	0.916
60.434776	2461.00	0.391	12.97	0	5.664	−2.323
61.150560	2504.00	0.626	12.48	0	1.731	−3.039
61.800154	2298.00	0.915	12.07	0	1.738	−3.797
62.411215	1933.00	1.260	11.71	0	−0.048	−4.277
62.486260	1517.00	0.083	14.68	0	−4.290	0.238
62.997977	1503.00	1.665	11.39	0	0.134	−4.860
63.568518	1087.00	2.115	11.08	0	0.541	−5.079
64.127767	733.50	2.620	10.78	0	0.814	−5.525
64.678903	463.50	3.195	10.50	0	0.415	−5.520
65.224071	274.80	3.815	10.20	0	0.069	−5.520
65.764772	153.00	4.485	10.00	0	−0.143	−5.520
66.302091	80.09	5.225	9.70	0	−0.428	−5.520
66.836830	39.46	6.005	9.40	0	−0.726	−5.520
67.369598	18.32	6.845	9.20	0	−1.002	−5.520
67.900867	8.01	7.745	8.90	0	−1.255	−5.520
68.431005	3.30	8.695	8.70	0	−1.500	−5.520
68.960311	1.28	9.695	8.60	0	−1.700	−5.520
118.750343	945.00	0.009	16.30	0	−0.247	0.003
368.498350	67.90	0.049	19.20	0.6	0	0
424.763124	638.00	0.044	19.16	0.6	0	0
487.249370	235.00	0.049	19.20	0.6	0	0
715.393150	99.60	0.145	18.10	0.6	0	0
773.839675	671.00	0.130	18.10	0.6	0	0
834.145330	180.00	0.147	18.10	0.6	0	0

Table 1. data for oxygen attenuation (taken from [59])

f_0	b_1	b_2	b_3	b_4	b_5	b_6
22.235080	0.1090	2.143	28.11	0.69	4.80	1.00
67.813960	0.0011	8.735	28.58	0.69	4.93	0.82
119.995941	0.0007	8.356	29.48	0.70	4.78	0.79
183.310074	2.3000	0.668	28.13	0.64	5.30	0.85
321.225644	0.0464	6.181	23.03	0.67	4.69	0.54
325.152919	1.5400	1.540	27.83	0.68	4.85	0.74
336.187000	0.0010	9.829	26.93	0.69	4.74	0.61
380.197372	11.9000	1.048	28.73	0.69	5.38	0.84
390.134508	0.0044	7.350	21.52	0.63	4.81	0.55
437.346667	0.0637	5.050	18.45	0.60	4.23	0.48
439.150812	0.9210	3.596	21.00	0.63	4.29	0.52
443.018295	0.1940	5.050	18.60	0.60	4.23	0.50
448.001075	10.6000	1.405	26.32	0.66	4.84	0.67
470.888947	0.3300	3.599	21.52	0.66	4.57	0.65
474.689127	1.2800	2.381	23.55	0.65	4.65	0.64
488.491133	0.2530	2.853	26.02	0.69	5.04	0.72
503.568532	0.0374	6.733	16.12	0.61	3.98	0.43
504.482692	0.0125	6.733	16.12	0.61	4.01	0.45
556.936002	510.0000	0.159	32.10	0.69	4.11	1.00
620.700807	5.0900	2.200	24.38	0.71	4.68	0.68
658.006500	0.2740	7.820	32.10	0.69	4.14	1.00
752.033227	250.0000	0.396	30.60	0.68	4.09	0.84
841.073593	0.0130	8.180	15.90	0.33	5.76	0.45
859.865000	0.1330	7.989	30.60	0.68	4.09	0.84
899.407000	0.0550	7.917	29.85	0.68	4.53	0.90
902.555000	0.0380	8.432	28.65	0.70	5.10	0.95
906.205524	0.1830	5.111	24.08	0.70	4.70	0.53
916.171582	8.5600	1.442	26.70	0.70	4.78	0.78
970.315022	9.1600	1.920	25.50	0.64	4.94	0.67
987.926764	138.0000	0.258	29.85	0.68	4.55	0.90

Table 2. Data for water vapor attenuation (taken from [59])

Debye spectrum is

$$d = 5.6\ 10^{-4}\ (p + 1.1e\theta). \tag{5.10}$$

Attenuation of the slant path can be expressed as

$$A(h\,,\theta) = \int_h^{\infty} \frac{\text{ɣ}(H)}{\sin \emptyset}\,,$$
$$\emptyset = \cos^{-1}\left(\frac{c}{(r+H)\times n(H)}\right), \tag{5.11}$$
$$c = (r+h)\ \times n(h)\ \times\ \cos\theta.$$

Minimum seal level is shown as

$$(r + h_{min}) \times n(h) = c. \tag{5.12}$$

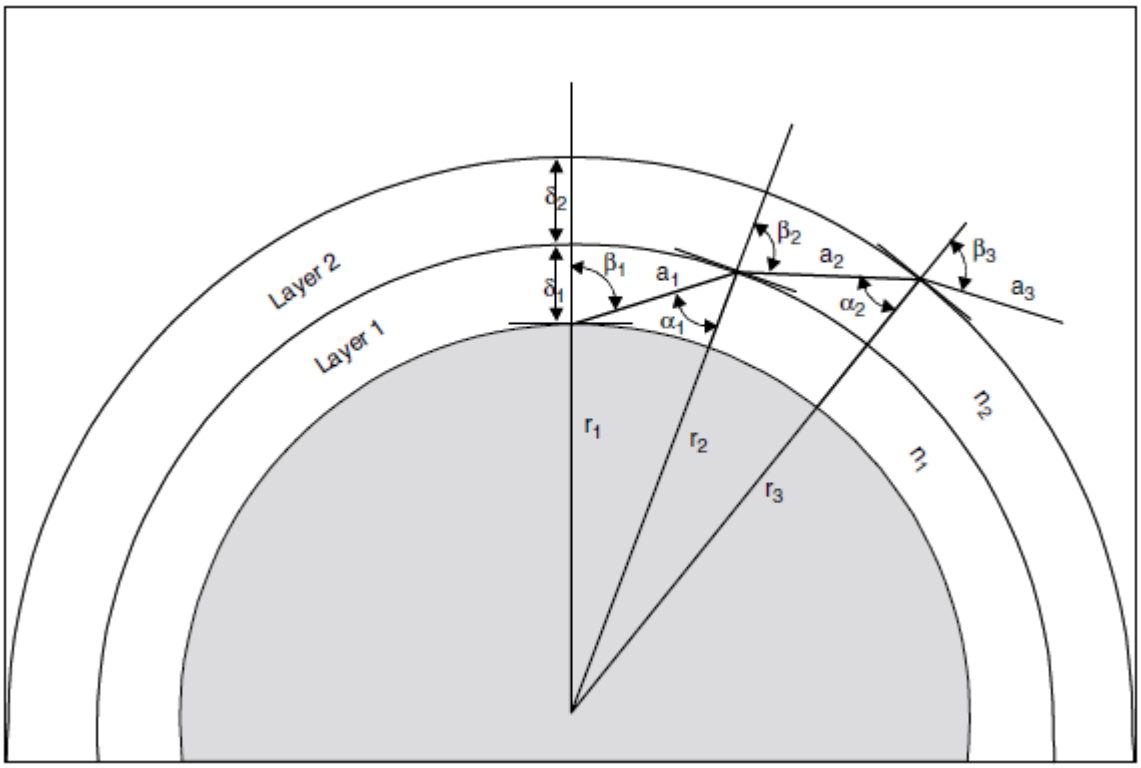

Table 3. Gaseous attenuation layers (taken from [59])

The path lengths can be expressed as

$$\begin{aligned} a_1 &= -r_1 \cos\beta_1 + \frac{1}{2}\sqrt{4{r_1}^2 cos^2\beta_1 + 8r_1\delta_1 + 4{\delta_1}^2}, \\ a_2 &= -r_2 \cos\beta_2 + \frac{1}{2}\sqrt{4{r_2}^2 cos^2\beta_2 + 8r_2\delta_2 + 4{\delta_2}^2}. \end{aligned} \tag{5.13}$$

Angles can be evaluated as

$$\begin{aligned} \alpha_1 &= \pi - \arccos\left(\frac{-{a_1}^2 - 2r_1\delta_1 - {\delta_1}^2}{2a_1r_1 + 2a_1\delta_1}\right), \\ \alpha_2 &= \pi - \arccos\left(\frac{-{a_2}^2 - 2r_2\delta_2 - {\delta_2}^2}{2a_2r_2 + 2a_2\delta_2}\right), \end{aligned} \tag{5.14}$$

$$\beta_2 = \arcsin\left(\frac{n_1}{n_2}\sin\alpha_1\right),$$

$$\beta_3 = \arcsin\left(\frac{n_2}{n_3}\sin\alpha_2\right).$$

The total slant path gaseous attenuation can be expressed as

$$A_{gas} = \sum_{i=1}^{k} a_i \gamma_i \ dB. \tag{5.15}$$

Atmospheric gas attenuation graphic is shown in Figure 20. 10 GHz which is used in this thesis radiowave frequency is pointed. Plotting the figure, atmospheric pressure is taken 101.300 kPa and temperature is taken 15°C. Also, water vapor density is 7.5 $\frac{g}{m^3}$.

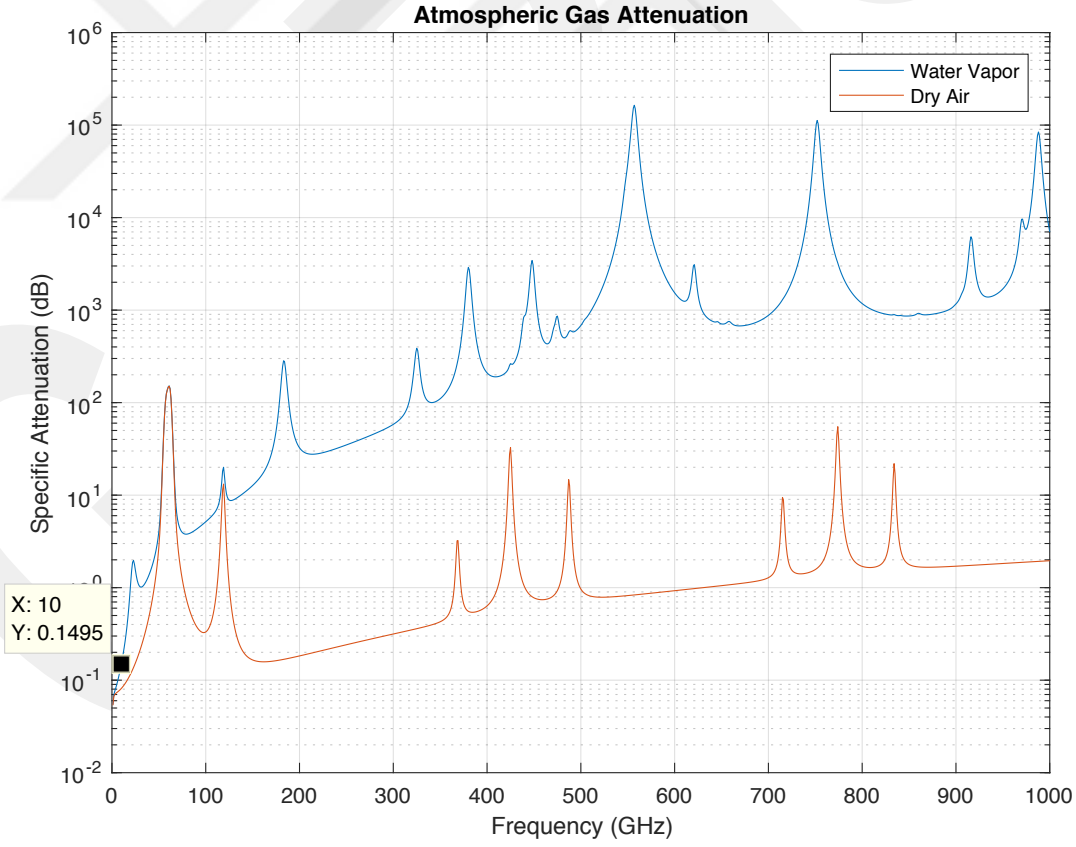

Figure 20. Atmospheric Gas Attenuation

5.3. Cloud Attenuation

Rain is most dominant hydrometeor affecting factor to radiowaves. However, beside the rain cloud effect on radiowave propagation must be considered. Clouds include water droplets with less than 0.1 mm diameter. Raindrop has diameter from 0.1mm to 10 mm. Clouds are not water vapor. They are water droplets. Their relative humidity is near 100%. [5] Broad assumptions should be made for the cloud attenuation model and empirical data should be used as the starting point, [4].

5.3.1. ITU-R Cloud Attenuation Model

A model to calculate the attenuation along an earth-space path for both clouds and fog is provided by the ITU-R in Recommendation ITU-R P.840, [55].

This model valid for up to 200 GHz.

- f: frequency (GHz)
- θ: elevation angle (°)
- T: surface temperature (°K)
- L: total columnar liquid water content (kg/m2)
- ϕ: inverse temperature constant

Inverse temperature constant can be expressed as

$$\phi = \frac{300}{T}. \tag{5.16}$$

T = 273.15 °K for cloud attenuation and inverse temperature constant becomes as

$$\phi = 1.098. \tag{5.17}$$

This method includes 5 steps. Steps are shown as

Step 1: Evaluate the relaxation frequencies

Principal and secondary relaxation frequencies f_p , f_s should be found as

$$\begin{aligned} f_p &= 20.09 - 142(\phi - 1) + 294(\phi - 1^2)\ GHz, \\ f_s &= 590 - 1500(\phi - 1)\ GHz. \end{aligned} \tag{5.18}$$

Step 2: Finding Complex dielectric permittivity

Complex dielectric permittivity's imaginary and real parts should be found as

$$\epsilon''(f) = \frac{f(\epsilon_0 - \epsilon_1)}{f_p\left[1+\left(\frac{f}{f_p}\right)^2\right]} + \frac{f(\epsilon_1 - \epsilon_2)}{f_s\left[1+\left(\frac{f}{f_s}\right)^2\right]},$$
$$\epsilon'(f) = \frac{(\epsilon_0 - \epsilon_1)}{\left[1+\left(\frac{f}{f_p}\right)^2\right]} + \frac{(\epsilon_1 - \epsilon_2)}{\left[1+\left(\frac{f}{f_s}\right)^2\right]} + \epsilon_2, \quad (5.19)$$

where

$$\epsilon_0 = 77.6 + 103.3(\phi - 1),$$
$$\epsilon_1 = 5.48, \quad (5.20)$$
$$\epsilon_2 = 3.51.$$

Step 3: Finding specific attenuation coefficient

- K_1 : specific attenuation coefficient $\frac{(\frac{dB}{km})}{(\frac{g}{m^3})}$

specific attenuation coefficient can be found as

$$K_1 = \frac{0.819\, f}{\epsilon''(1+\eta^2)} \frac{(\frac{dB}{km})}{(\frac{g}{m^3})}, \quad (5.21)$$

where

$$\eta = \frac{2+\epsilon'}{\epsilon''}. \quad (5.22)$$

Step 4: Finding Columnar liquid water content

- L: Cloud's columnar liquid water content $(\frac{kg}{m^2})$

Global maps for cloud liquid water content is published by ITU-R. From Figure 21 to Figure 23 present the cloud liquid water contents.

Step 5: Finding total attenuation

- A_{tc} : Total cloud attenuation (dB)

$$A_{tc} = \frac{L\, K_1}{\sin\theta}\, dB. \quad (5.23)$$

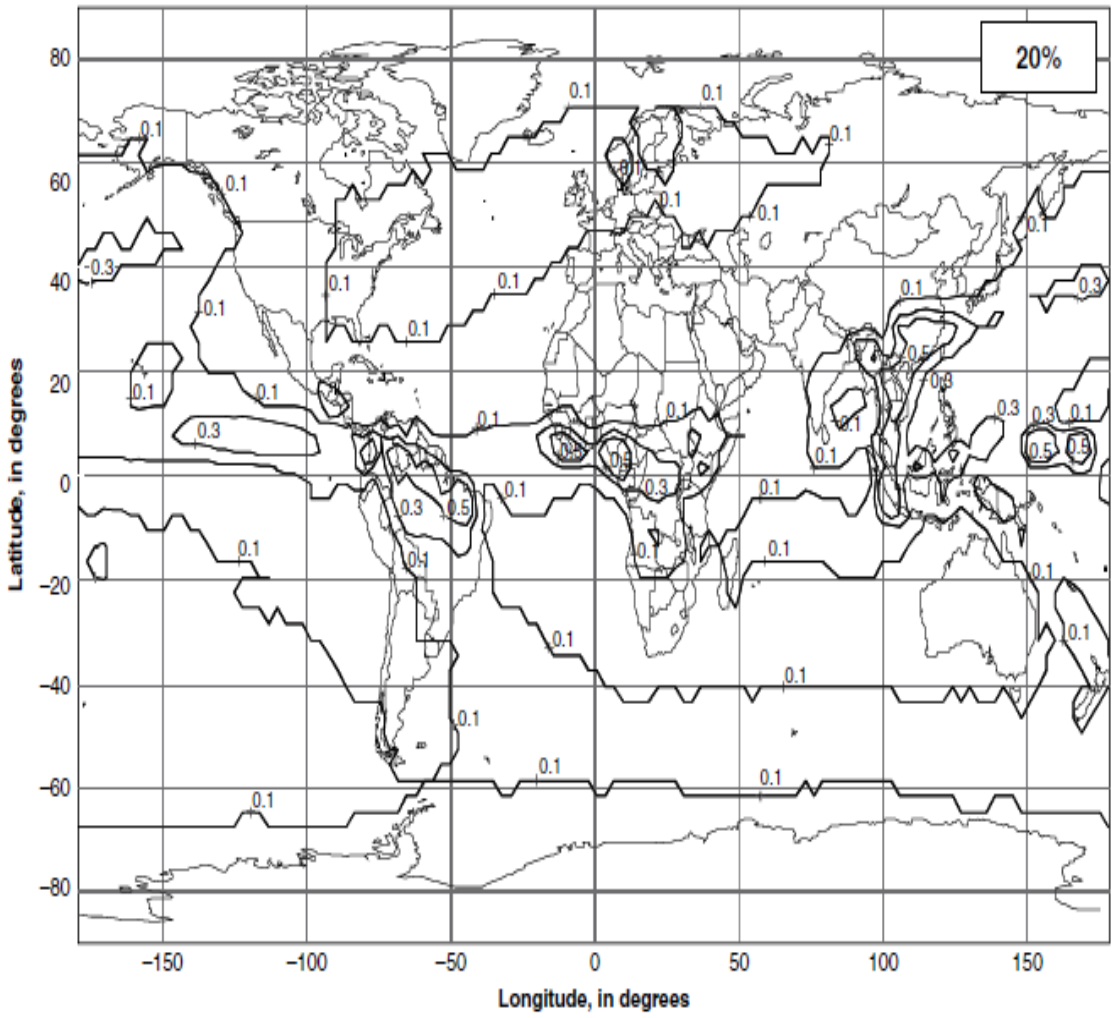

Figure 21. Normalized total columnar content of cloud liquid water exceeded for 20% of the year, in kg/m^2 , (taken from [55]).

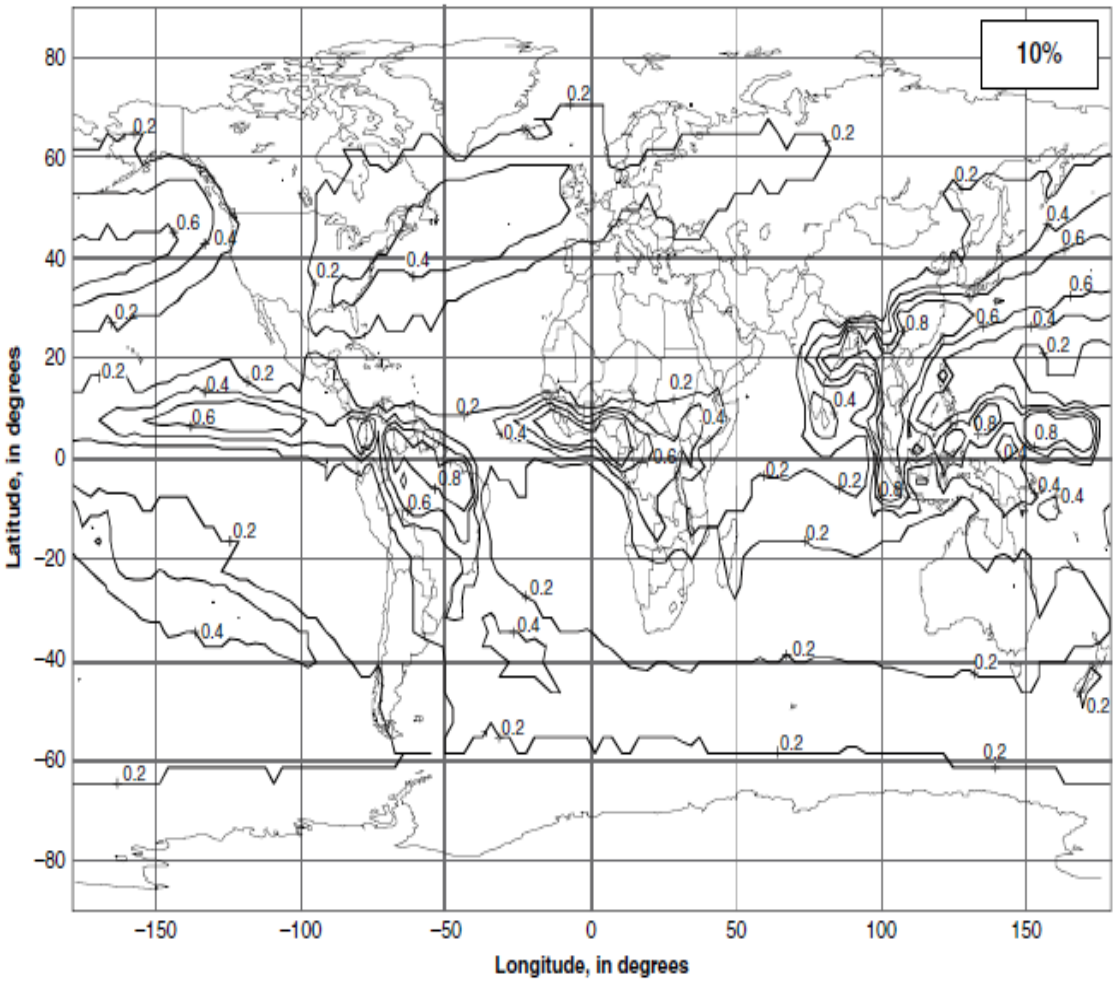

Figure 22. Normalized total columnar content of cloud liquid water exceeded for 10% of the year, in kg/m^2 , (taken from [55]).

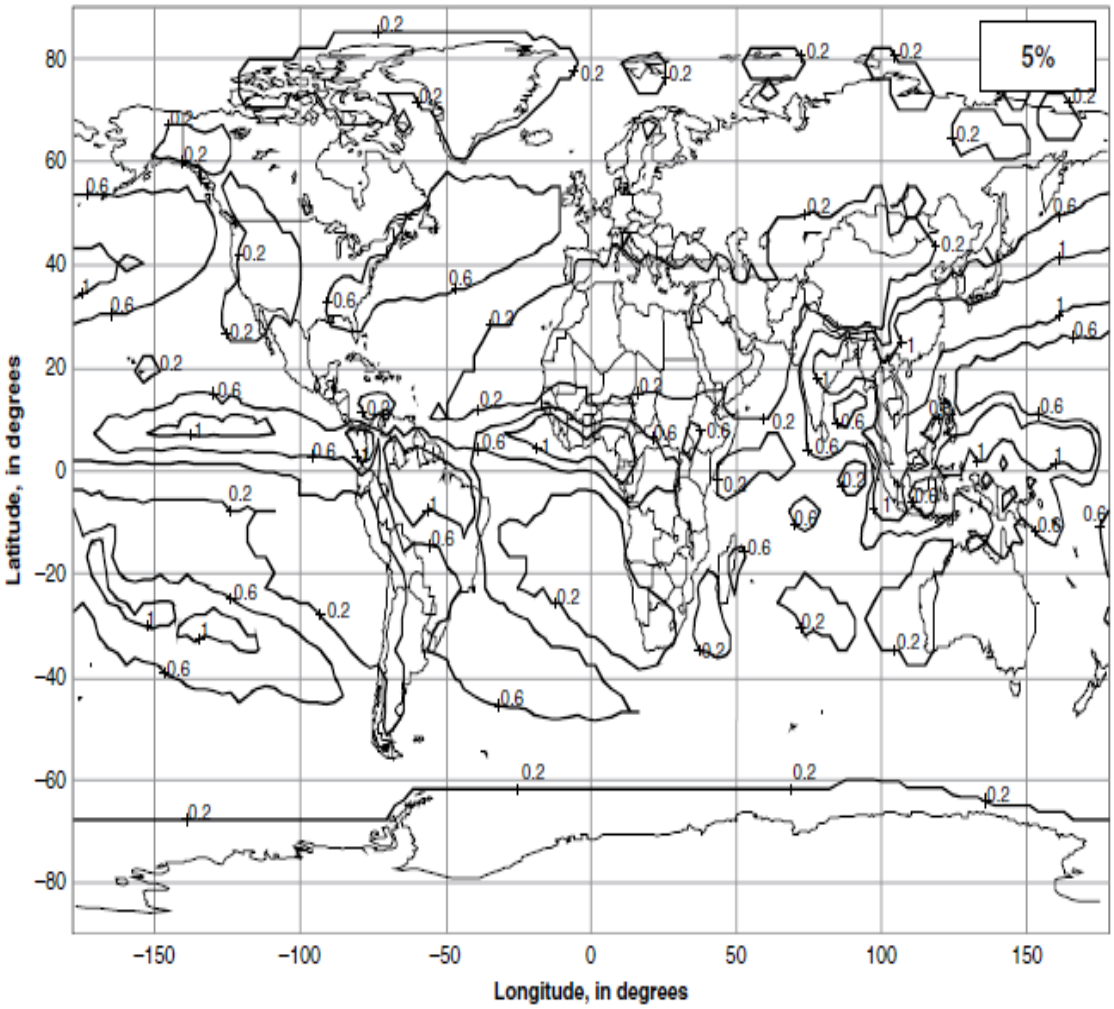

Figure 23. Normalized total columnar content of cloud liquid water exceeded for 5% of the year, in kg/m^2, (taken from [55]).

Cloud attenuation graphic is shown in Figure 24. 10 GHz which is used in this thesis radiowave frequency is pointed. Plotting the figure, temperature is taken 15℃. Also, liquid water density is 7.5 $\frac{g}{m^3}$.

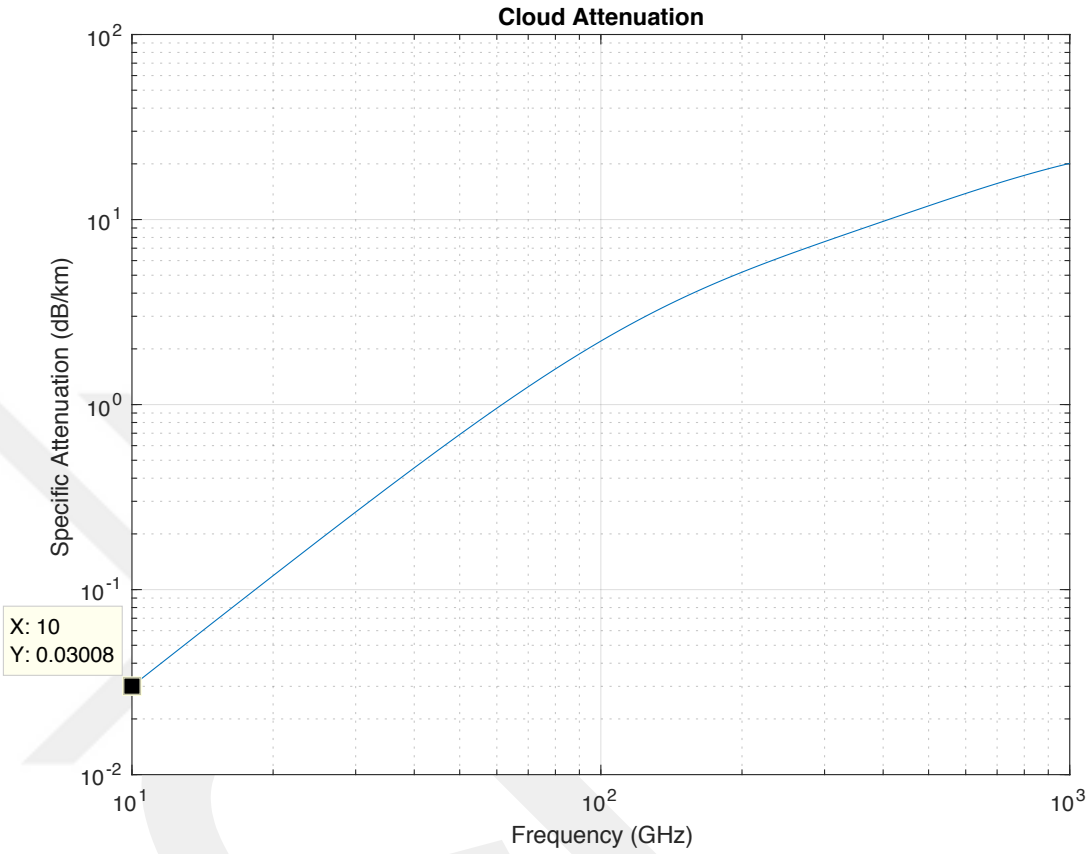

Figure 24. Cloud Attenuation

5.4. Tropospheric Scintillation

Scintillation is the rapid fluctuation on parameters of radiowaves. Amplitude, phase, angle of arrival and polarization can be affected by scintillation. Above 3 GHz, scintillation is occurred by troposphere. With height refractive index can be varied, [4]. Refractive index fluctuations are occurred by Tropospheric scintillation. These effects can change day by day, [5]. With using same equipments and frequency, worst result is taken at low elevation than high elevation about tropospheric scintillation, [4].

5.4.1. ITU-R Scintillation Model

Effective method for estimating the statistics of tropospheric scintillation is provided by ITU-R, [56].

ITU-R tested this procedure between 7 and 14 GHz.

Also, the method described here is valid for slant path elevation angles ≥ 4◦ ,[5].

- T: average surface ambient temperature (◦C) at the site for a period of one month or longer
- H: average surface relative humidity (%) at the site for a period of one month or longer
- f: frequency (GHz),
- θ: path elevation angle, where $\theta \geq 4^\circ$
- D: physical diameter (m) of the earth-station antenna
- η: antenna efficiency
- e_s : saturation water vapor pressure
- N_w : wet term of the radio refractivity
- σ_r : standard deviation of the signal amplitude
- L : effective path length
- D_e : effective antenna diameter
- p: percent outage
- $a(p)$: time percentage %

There are 9 steps for calculating tropospheric scintillation as shown

Step 1: Evaluate the saturation water vapor pressure as

$$e_s = 6.1121\, e^{\frac{17.502T}{T+240.97}}\,(kPa). \tag{5.24}$$

Step 2: Finding the wet term of the radio refractivity as

$$N_w = \frac{3732He_s}{(273+T)^2}. \tag{5.25}$$

Step 3: Finding the standard deviation of the signal amplitude as

$$\sigma_r = 3.6 \times 10^{-3} + N_w \times 10^{-4}\ dB. \tag{5.26}$$

Step 4: Finding the effective path length as

$$L = \frac{2h_L}{\sqrt{sin^2(\theta) + 2.35 \times 10^{-4} + sin\theta}}\ m, \tag{5.27}$$

where h_L is turbulent layer and it is 1 km.

Step 5: Find the effective antenna diameter as

$$D_e = \sqrt{\eta} D \quad m\,. \tag{5.28}$$

Step 6: Finding the antenna averaging factor as

$$g(x) = \sqrt{3.86(x^2+1)^{11/12}.\, sin\left[\frac{11}{6}\arctan\left(\frac{1}{x}\right)\right] - 7.08x^{5/6}}, \tag{5.29}$$

where

$$x = 1.22\frac{{D_e}^2 f}{L}. \tag{5.30}$$

Step 7: Finding the standard deviation as

$$\sigma = \sigma_r\, f^{7/12}\frac{g(f)}{(sin\theta)^{1.2}}. \tag{5.31}$$

Step 8: Finding the time percentage factor as

$$a(p) = -0.061(log_{10}p)^3 + 0.072(log_{10}p)^2 - 1.71log_{10}p + 3. \tag{5.32}$$

Step 9: Calculate the scintillation fade depth as

$$A_s(p) = a(p).\sigma\ dB. \tag{5.33}$$

Scintillation loss is shown in the Figure 25. At 4° elevation angle, scintillation loss is 5dB which will be used in this thesis.

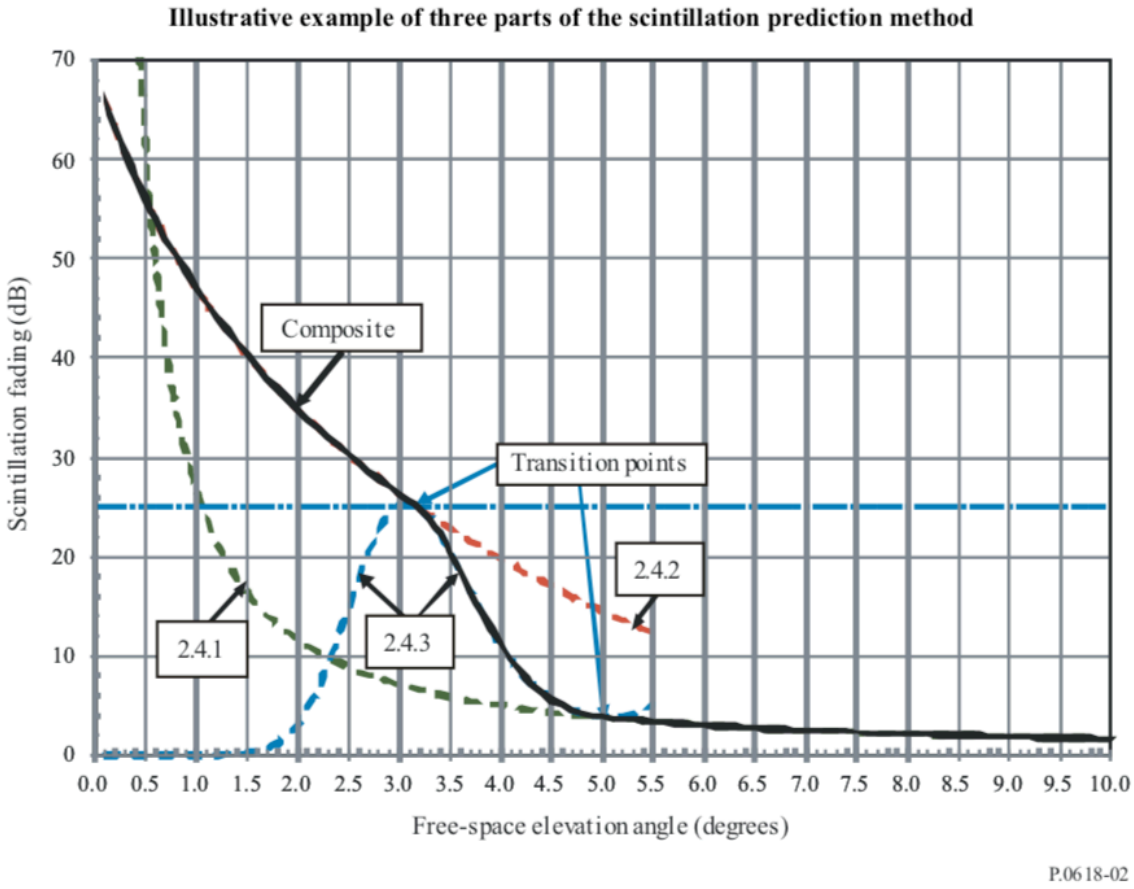

Figure 25. Scintillation Loss (taken from [56])

5.5. Total Loss

Total loss can be calculated by summing the all losses which are expressed above. Coverage zone of Europe of Türksat 4A is 54 dBW, [88].

$$\alpha_{dB} = -(5 + 0.03 + 0.1495) \tag{5.34}$$

In order to add this loss into scattered integral of parabolic reflector antenna, it should be converted to attenuation coefficient. It can be written by

$$\begin{aligned} \alpha_{dB} &= 8.686\alpha, \\ A &= e^{2\alpha z}. \end{aligned} \tag{5.35}$$

CHAPTER 6

6. SCATTERED FIELDS BY CIVILIAN PLANE

Civilian plane is modeled as Boeing 737-900. Plane is manufactured by Boeing which is one of the most important airspace company. Plane's figure is shown in Figure 26.

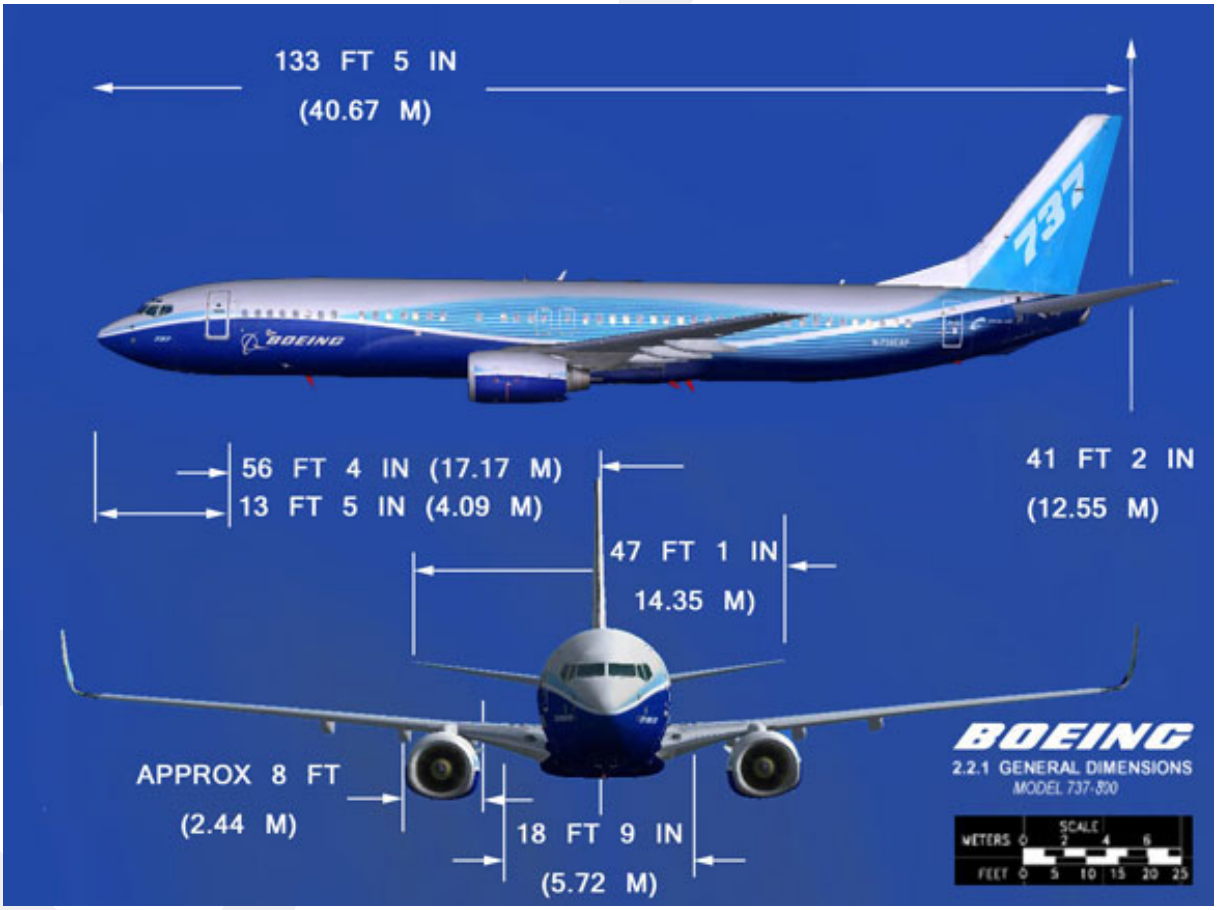

Figure 26. Boeing 737-900 Dimensions, [89].

In the far field, electromagnetic fields which are radiated from satellite will be plane wave. Here, plane is modeled as line strip which defines that half-length of the strip(a) is equal to 20.335m. Geometrical optics fields and diffracted fields are investigated. MTPO method is used in order to find scattered fields.

In this thesis, line strip is divided two parts which are from 0 to +a and from -a to 0. Evaluations are done for these two line strips. Scattered fields by line strip from -a to +a is found by summation of scattered fields by line strip from 0 to +a and scattered fields by line strip from -a to 0.

Scattered fields by plane is found uniform in this section. Attenuations are not implicated in simulations. Attenuation, real ranges are considered in Section 8.1, 8.2.

Simulations are done with parameters of

- $\lambda = 0.1m$,
- $\rho = 6\lambda$,
- $a = \lambda$.

6.1. GO Waves

Figure 27 shows geometry of radiated plane waves through plane.

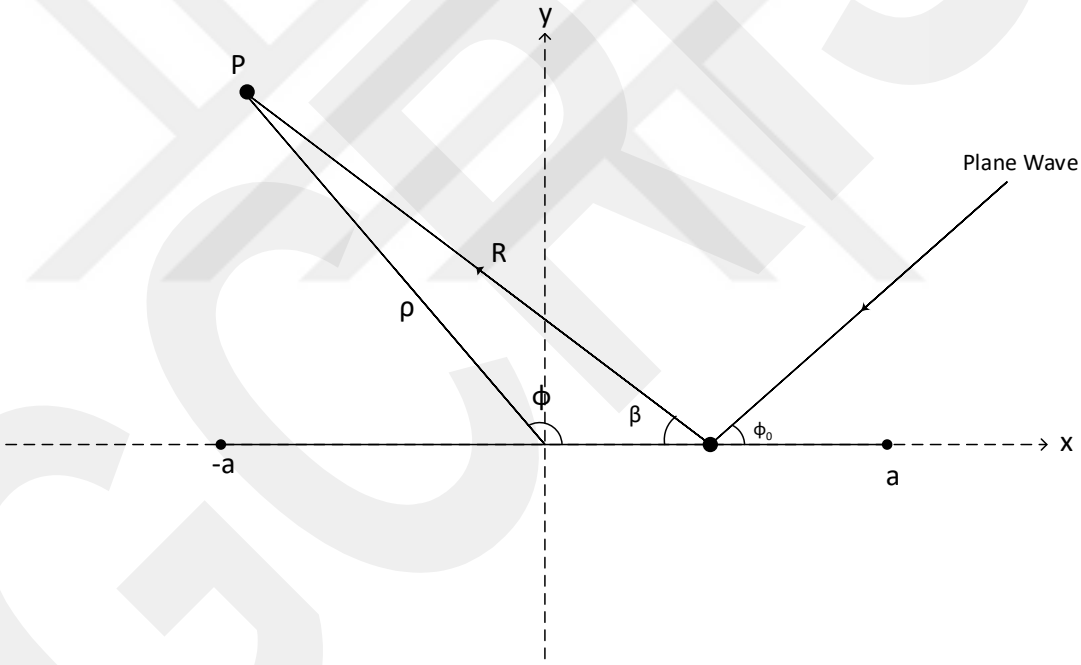

Figure 27. Geometry of Plane with Radiated Plane Waves

R is distance to observation point. R is defined in equation (6.1).

$$R = \sqrt{\rho^2 + x'^2 - 2\rho x' cos\emptyset} \tag{6.1}$$

Incident plane waves can be expressed as

$$\vec{E}_i = E_0 e^{jk[x\cos\emptyset_0 + y\sin\emptyset_0]}. \tag{6.2}$$

In order to find induced current on strip, $\vec{H}_i$ should be expressed. $\vec{H}_i$ is introduced in equation (6.3).

$$\vec{H}_i = -\frac{1}{jw\mu_0}\nabla x\vec{E}_i$$

$$\vec{H}_i = -\frac{E_0}{jw\mu_0}\begin{vmatrix} \overrightarrow{e_x} & \overrightarrow{e_y} & \overrightarrow{e_z} \\ \frac{\partial}{\partial_x} & \frac{\partial}{\partial_y} & 0 \\ 0 & 0 & e^{jk[x'\cos\emptyset_0 + y'\sin\emptyset_0]} \end{vmatrix} \tag{6.3}$$

After calculating matrix, $\vec{H}_i$ is became equation (6.4).

$$\vec{H}_i = -\frac{E_0 k}{w\mu_0}\left[sin\emptyset_0\overrightarrow{e_x} - cos\emptyset_0\overrightarrow{e_y}\right]e^{jk[x'cos\emptyset_0 + y'sin\emptyset_0]} \tag{6.4}$$

Normal vector for reflected surface in MTPO method can be expressed as

$$\overrightarrow{n_1} = \sin\left(\frac{\beta - \emptyset_0}{2}\right)\overrightarrow{e_x} + \cos\left(\frac{\beta - \emptyset_0}{2}\right)\overrightarrow{e_y}. \tag{6.5}$$

After finding normal vector and magnetic field intensity, reflected induced current (J_{rmtpo}) is showed in (6.6).

$$J_{rmtpo} = \overrightarrow{n_1}\, x\, \vec{H}_i\big|_{y'=0} \tag{6.6}$$

Reflected induced current can be evaluated using (6.4) and (6.5) as

$$J_{rmtpo} = \frac{E_0 k}{w\mu_0}\sin\left(\frac{\beta + \emptyset_0}{2}\right)e^{jkx'cos\emptyset_0}\overrightarrow{e_z}. \tag{6.7}$$

Normal vector for incident surface in MTPO method can be expressed as (6.8).

$$\overrightarrow{n_2} = \sin\left(\frac{\beta - \emptyset_0}{2}\right)\overrightarrow{e_x} - \cos\left(\frac{\beta - \emptyset_0}{2}\right)\overrightarrow{e_y} \tag{6.8}$$

After finding normal vector and magnetic field intensity, incident induced current (J_{imtpo}) is showed in (6.9).

$$J_{imtpo} = \overrightarrow{n_2}\, x\, \vec{H}_i\big|_{y'=0} \tag{6.9}$$

Incident induced current can be evaluated using (6.7) and (6.8) as

$$J_{imtpo} = \frac{E_0 k}{w\mu_0} \sin\left(\frac{\beta - \emptyset_0}{2}\right) e^{jkx' cos\emptyset_0}. \tag{6.10}$$

Scattering integral can be written by using (6.6) and (6.10) as

$$U(P) = -\frac{E_0 k}{2\pi w} \oiint e^{jkx' cos\emptyset_0} \frac{e^{-jkR}}{kR} \left[\sin\left(\frac{\beta - \emptyset_0}{2}\right) + \sin\left(\frac{\beta + \emptyset_0}{2}\right)\right] dS'. \tag{6.11}$$

R is equal to $R = \sqrt{(x - x')^2 + y^2 + (z - z')^2}$. Umul [7] is calculated directly to z' part. Expression can be showed as

$$U(P) = -\frac{E_0 k}{2\pi w} \int_{-a}^{a} e^{jkx' cos\emptyset_0} \left[-\frac{\pi}{j} H_0(kR_1)\right] \left[\sin\left(\frac{\beta - \emptyset_0}{2}\right) + \sin\left(\frac{\beta + \emptyset_0}{2}\right)\right] dx'. \tag{6.12}$$

$H_0(kR_1)$ is second kind zero order Hankel function. And it can be expressed as

$$-\frac{\pi}{j} H_0(kR_1) = -\frac{\pi}{j} \sqrt{\frac{2}{\pi}} e^{-\frac{j\pi}{4}} \frac{e^{-jkR_1}}{\sqrt{kR_1}}. \tag{6.13}$$

R_1 is equal to $R_1 = \sqrt{(x - x')^2 + y^2}$. By using equation (6.13), integral can be expressed as

$$U(P) = \frac{E_0 k e^{-\frac{j\pi}{4}}}{\sqrt{2\pi} j} \int_{-a}^{a} e^{jkx' cos\emptyset_0} \frac{e^{-jkR_1}}{\sqrt{kR_1}} \left[\sin\left(\frac{\beta - \emptyset_0}{2}\right) + \sin\left(\frac{\beta + \emptyset_0}{2}\right)\right] dx'. \tag{6.14}$$

Here, stationary phase method is used to find geometrical optic waves. Phase function of stationary phase method is shown in (6.15), [60].

$$g(x') = x' cos\emptyset_0 - R_1 \tag{6.15}$$

First and second derivative of the phase function can be expressed as

$$g'(x') = cos\emptyset_0 - co\beta, \tag{6.16}$$

$$g''(x') = -\frac{sin^2(\beta)}{R_{1s}}.$$

$g'(x')$ is equal to 0 for finding stationary phase point. Stationary phase points are equal to $\beta = \pm\emptyset_0$. Reflected GO can be calculated at $\beta = \emptyset_0$. Figure 28 is showing the stationary phase point geometry.

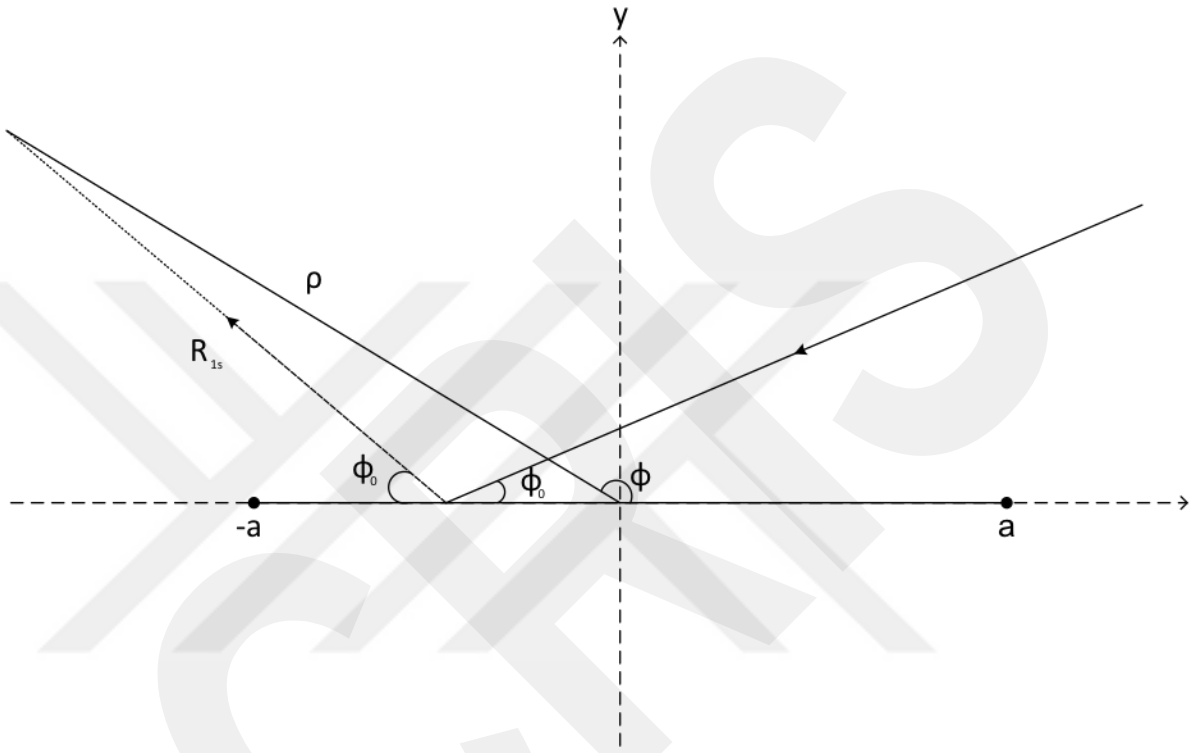

Figure 28. Geometry of Stationary Phase Point in Order to Find Reflected GO Wave

Stationary distance to observation point is R_{1s}. It can be expressed as

$$R_{1s} = -\rho cos(\emptyset + \emptyset_0) + x' cos(\emptyset_0). \quad (6.17)$$

Stationary phase function can be gathered for reflected GO waves as

$$\varphi|_{\beta=\emptyset_0} = x' cos\emptyset_0 - R_{1s} + \frac{1}{2}\left(-\frac{sin^2(\emptyset_0)}{R_{1s}}\right)(x - x')^2 . \quad (6.18)$$

Integral is evaluated as (6.19).

$$E_r^{GO} = -jw\frac{E_0 k e^{-\frac{j\pi}{4}}}{w\sqrt{2\pi}j}\frac{e^{jk\rho cos(\emptyset+\emptyset_0)}}{\sqrt{kR_{1s}}}\, sin(\emptyset_0)\int_{-a}^{a} e^{-jk\frac{1}{2}\frac{sin^2(\emptyset_0)}{R_{1s}}(x-x')^2}\, dx' \quad (6.19)$$

Error function is used to calculate integral in (6.19).

$$\int_{-a}^{a} e^{-jk\frac{1}{2}\frac{sin^2(\emptyset_0)}{R_{1s}}(x-x')^2}\, dx' \cong \sqrt{2\pi}\sqrt{\frac{R_{1s}}{k}}\,\frac{e^{\frac{j\pi}{4}}}{sin(\emptyset_0)} \tag{6.20}$$

Reflected GO wave is represented in equation (6.21) without limitation.

$$E_r^{GO} = -E_0 e^{jk\rho cos(\emptyset+\emptyset_0)} \tag{6.21}$$

Incident GO can be calculated at $\beta = -\emptyset_0$. Figure 29 is showing the stationary phase point geometry.

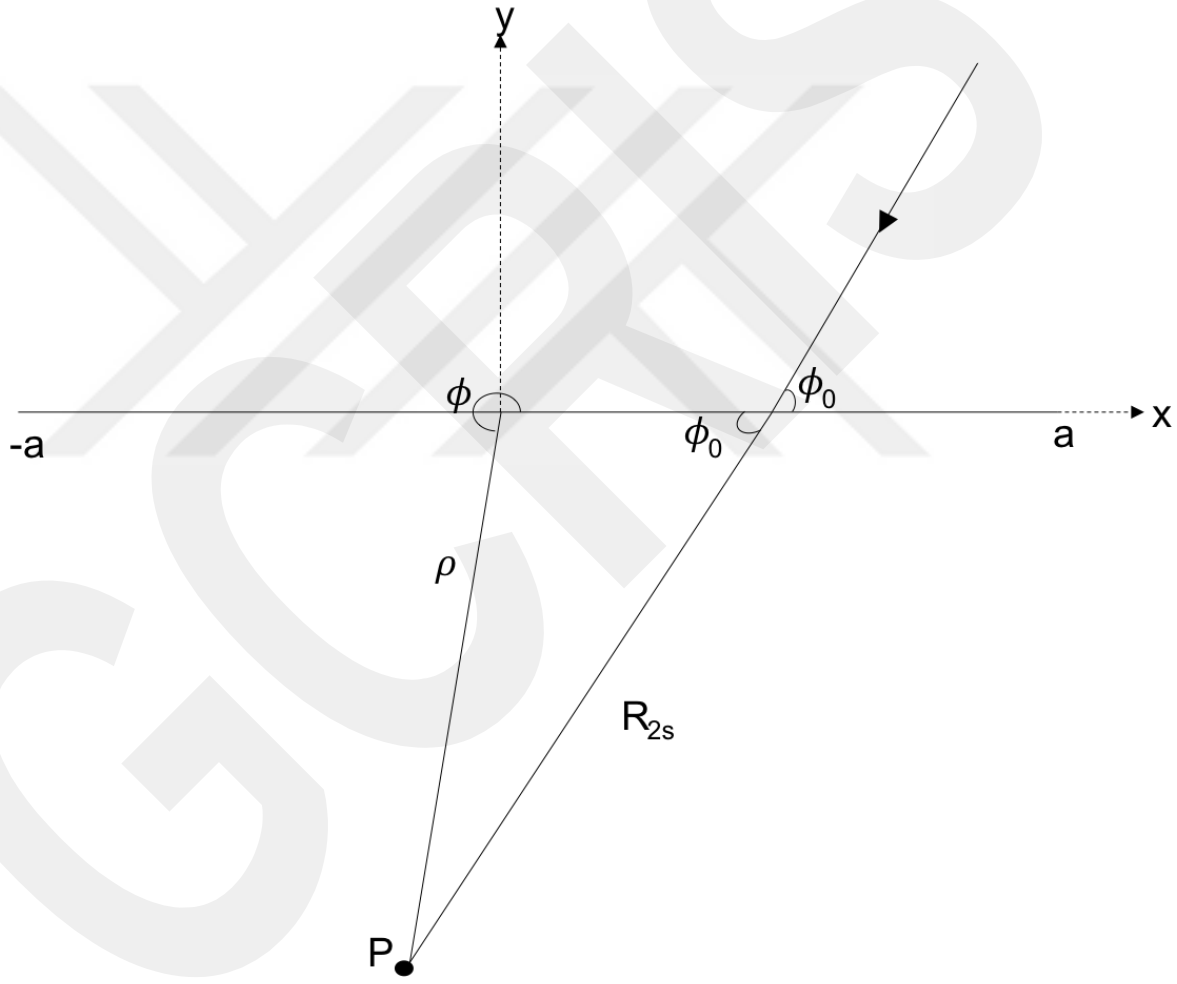

Figure 29. Geometry of Stationary Phase Point in Order to Find Incident GO Wave

Stationary distance to observation point is R_{2s}. It can be expressed as

$$R_{2s} = -\rho cos(\emptyset - \emptyset_0) + x' cos(\emptyset_0)\,. \tag{6.22}$$

Stationary phase function can be gathered for reflected GO waves as

$$\varphi|_{\beta=-\emptyset_0} = x'cos\emptyset_0 - R_{2s} + \frac{1}{2}\frac{sin^2(\emptyset_0)}{R_{2s}}(x-x')^2. \quad (6.23)$$

Integral is evaluated as (6.24).

$$E_i^{GO} = -jw\frac{E_0 k e^{-\frac{j\pi}{4}}}{w\sqrt{2\pi}j}\frac{e^{jk\rho cos(\emptyset-\emptyset_0)}}{\sqrt{kR_{2s}}}\, sin(\emptyset_0)\int_{-a}^{a} e^{-jk\frac{1}{2}\frac{sin^2(\emptyset_0)}{R_{2s}}(x-x')^2}\, dx' \quad (6.24)$$

Error function is used to calculate integral in (6.24).

$$\int_{-a}^{a} e^{-jk\frac{1}{2}\frac{sin^2(\emptyset_0)}{R_{1s}}(x-x')^2}\, dx' \cong \sqrt{2\pi}\sqrt{\frac{R_{1s}}{k}}\frac{e^{\frac{j\pi}{4}}}{sin(\emptyset_0)} \quad (6.25)$$

Reflected GO wave is represented in equation (6.26) without limitations.

$$E_i^{GO} = E_0 e^{jk\rho cos(\emptyset-\emptyset_0)} \quad (6.26)$$

6.1.1. GO Waves by Line Strip from 0 to +a

GO waves should be limited. In this thesis, detour parameters will be used to limit GO waves. Detour parameter for +a point is defined in Section 6.3.2. Reflected GO waves with limitation can be expressed as

$$E_r^{GO} = -E_0 e^{jk\rho cos(\emptyset+\emptyset_0)} U(-\zeta_{rd+a}). \quad (6.27)$$

Incident GO waves with limitation can be defined as

$$E_i^{GO} = E_0 e^{jk\rho cos(\emptyset-\emptyset_0)}\, U(-\zeta_{id+a}). \quad (6.28)$$

ζ_{rd+a} and ζ_{id+a} are detour parameters at +a point. Total GO waves can be shown as

$$E_t^{GO} = E_0 e^{jk\rho cos(\emptyset-\emptyset_0)}\, U(-\zeta_{id+a}) - E_0 e^{jk\rho cos(\emptyset+\emptyset_0)} U(-\zeta_{rd+a}). \quad (6.29)$$

Uniform reflected GO waves are showed in Figure 30.

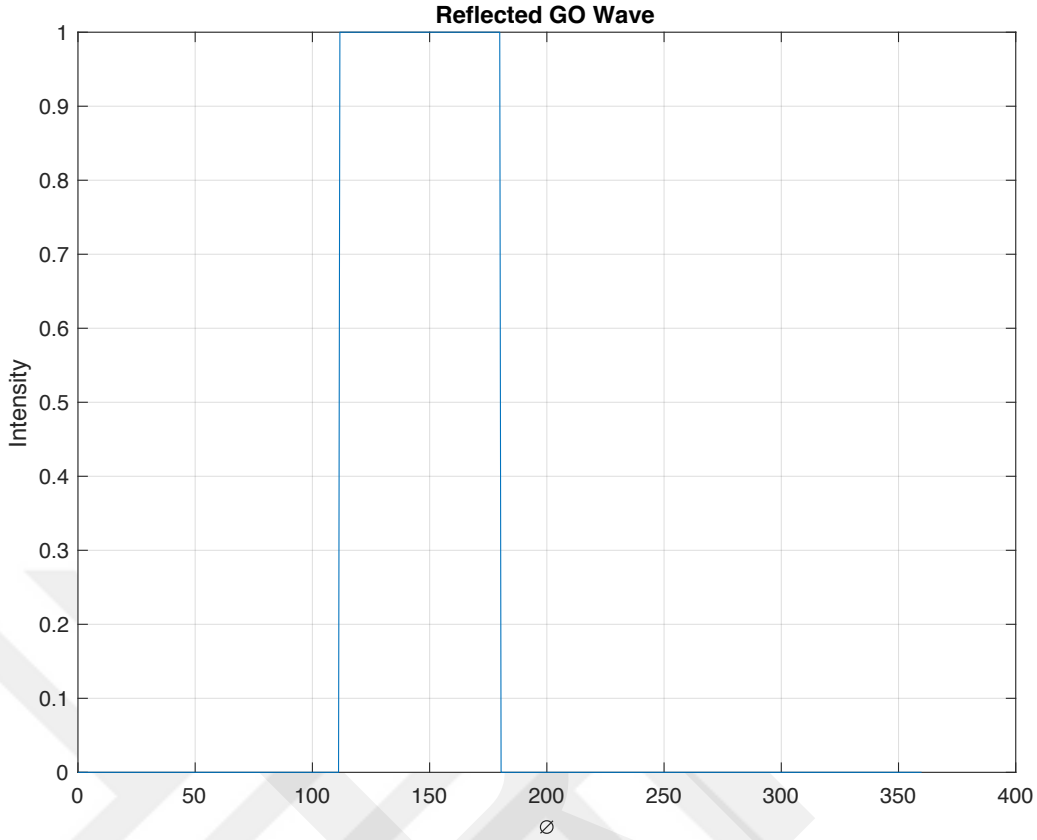

Figure 30. Reflected GO Wave

Uniform incident GO waves are showed in Figure 30.

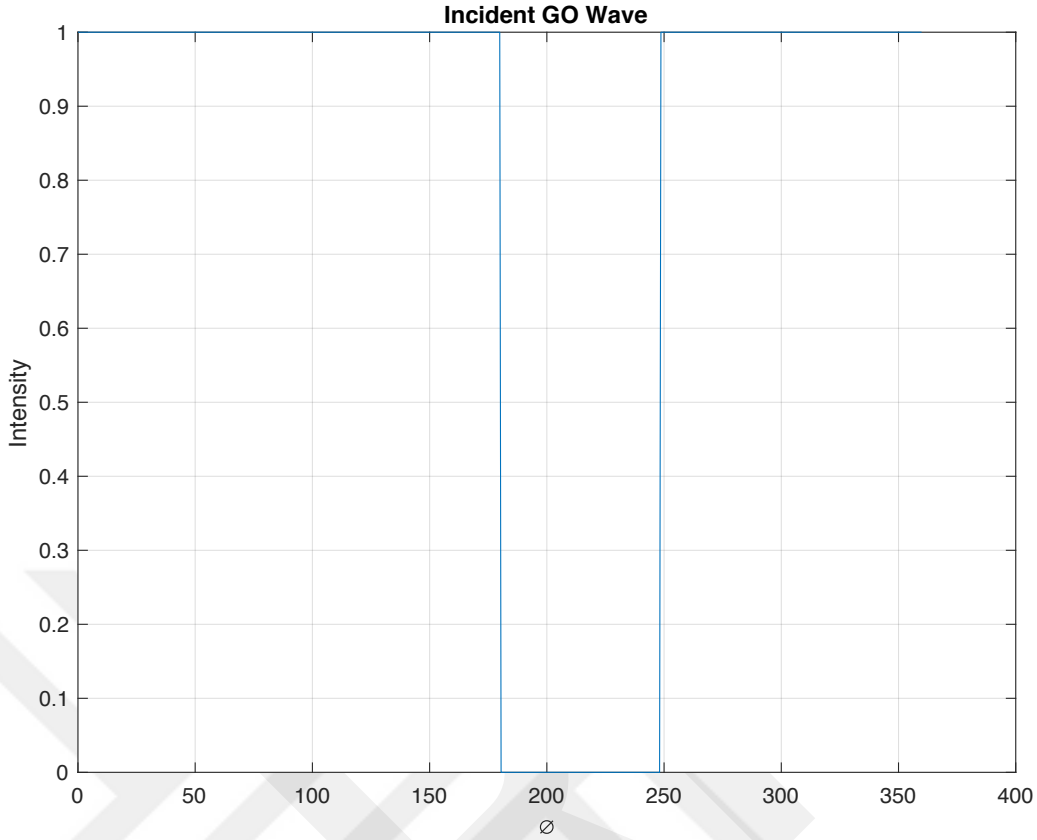

Figure 31. Incident GO Wave

Total uniform GO waves are shown in Figure 32.

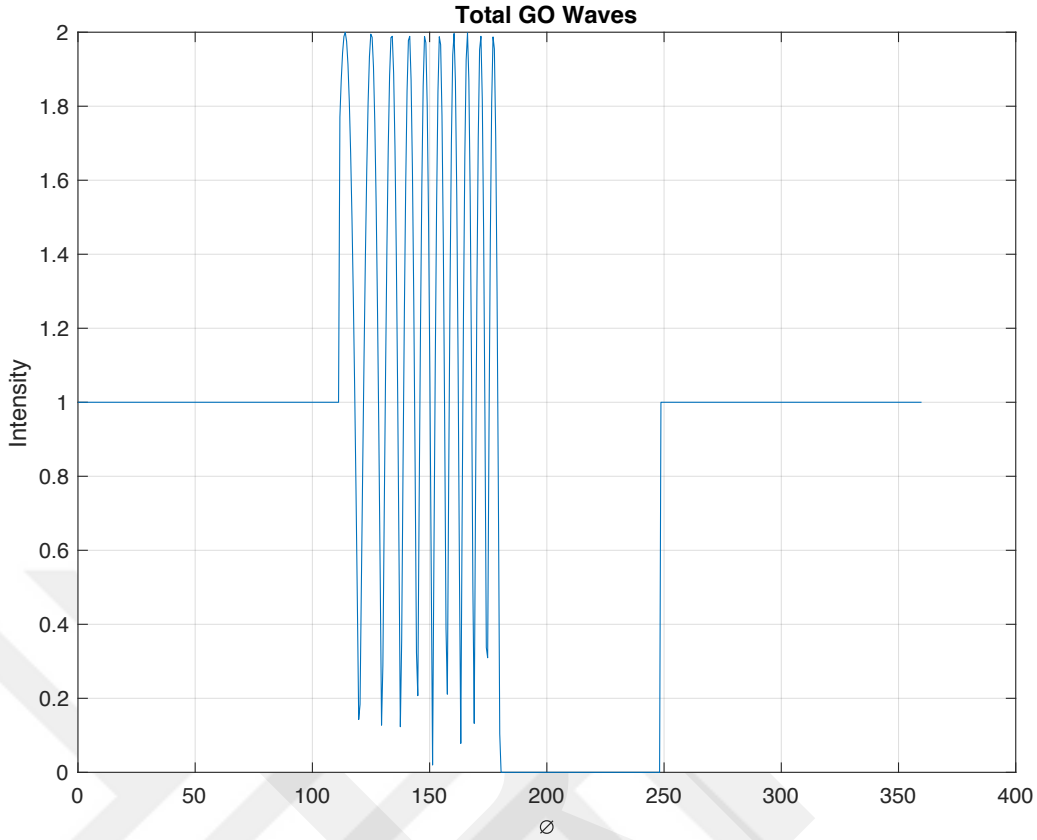

Figure 32. Total GO Waves

6.1.2. GO Waves by Line Strip from -a to 0

GO waves should be limited. In this thesis, detour parameters will be used to limit GO waves. Detour parameter for -a point is defined in Section 6.3.3. Reflected GO waves with limitation can be expressed as

$$E_r^{GO} = -E_0 e^{jk\rho cos(\emptyset+\emptyset_0)} U(-\zeta_{rd-a}). \quad (6.30)$$

Incident GO waves with limitation can be defined as

$$E_i^{GO} = E_0 e^{jk\rho cos(\emptyset-\emptyset_0)} \; U(-\zeta_{id-a}). \quad (6.31)$$

ζ_{rd-a} and ζ_{id-a} are detour parameters at –a point. Total GO waves can be shown as

$$E_t^{GO} = E_0 e^{jk\rho cos(\emptyset-\emptyset_0)} \; U(-\zeta_{id-a}) - E_0 e^{jk\rho cos(\emptyset+\emptyset_0)} U(-\zeta_{rd-a}). \quad (6.32)$$

Uniform reflected GO waves are showed in Figure 33.

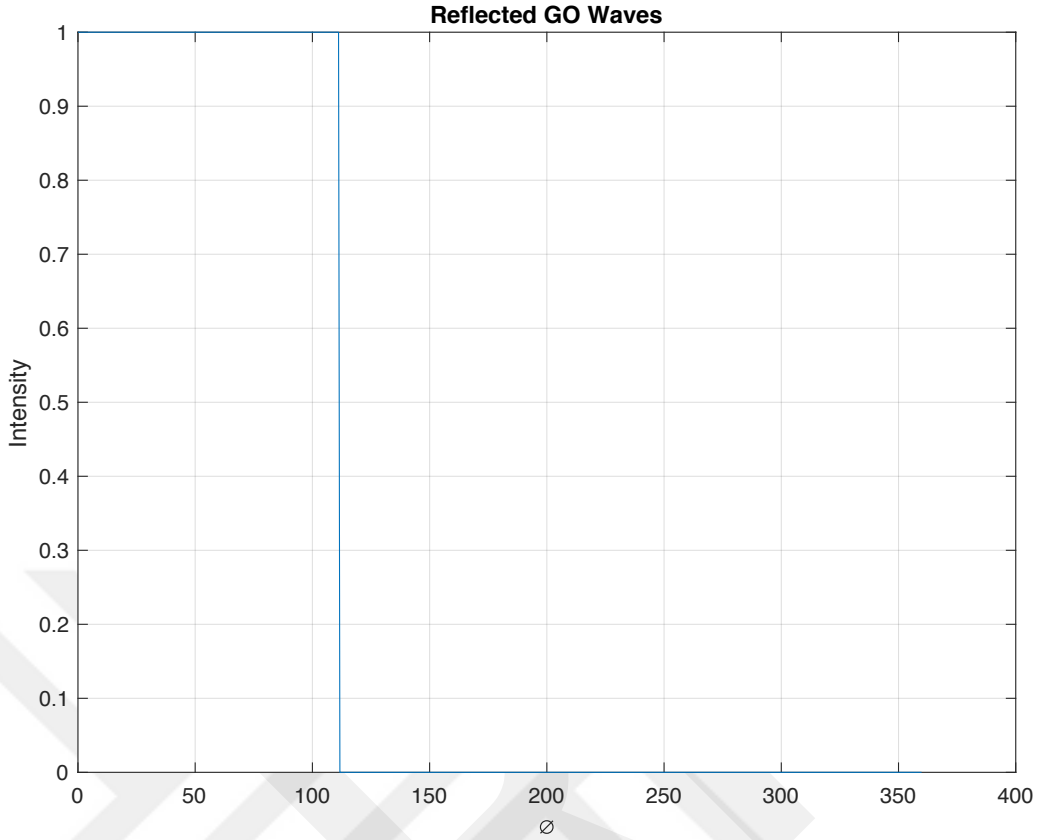

Figure 33. Reflected GO Wave

Uniform incident GO waves are showed in Figure 34.

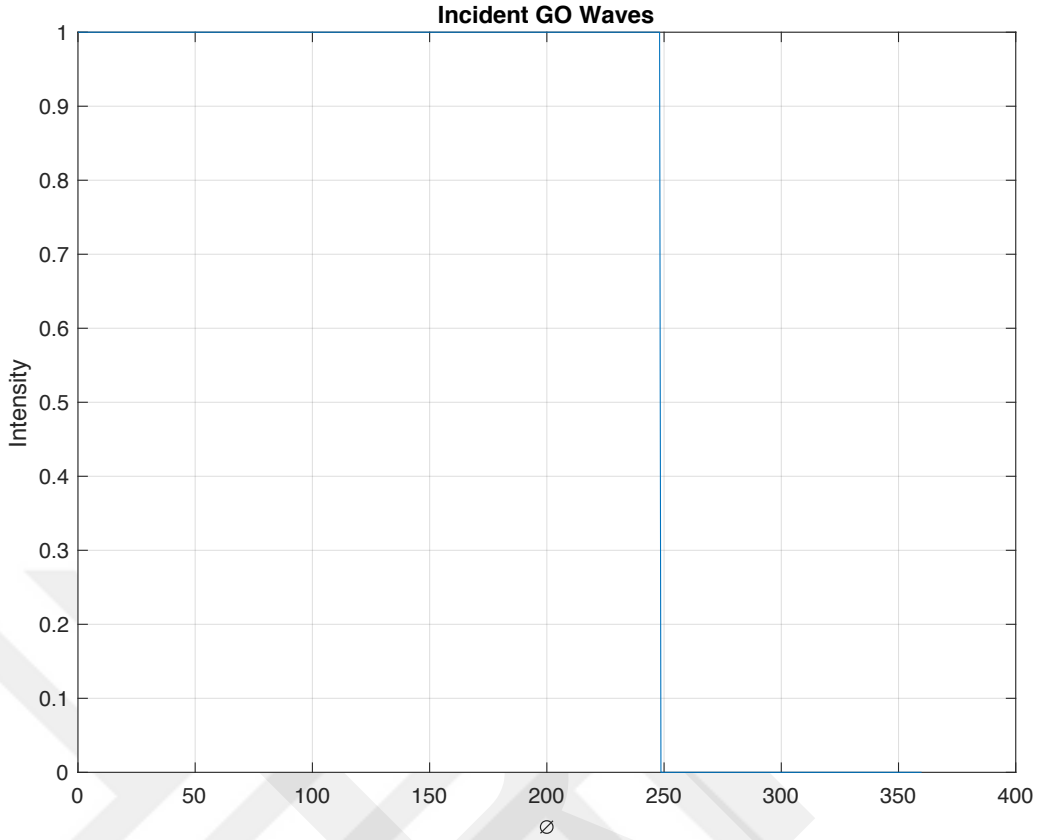

Figure 34. Incident GO Wave

Total uniform GO waves are shown in Figure 35.

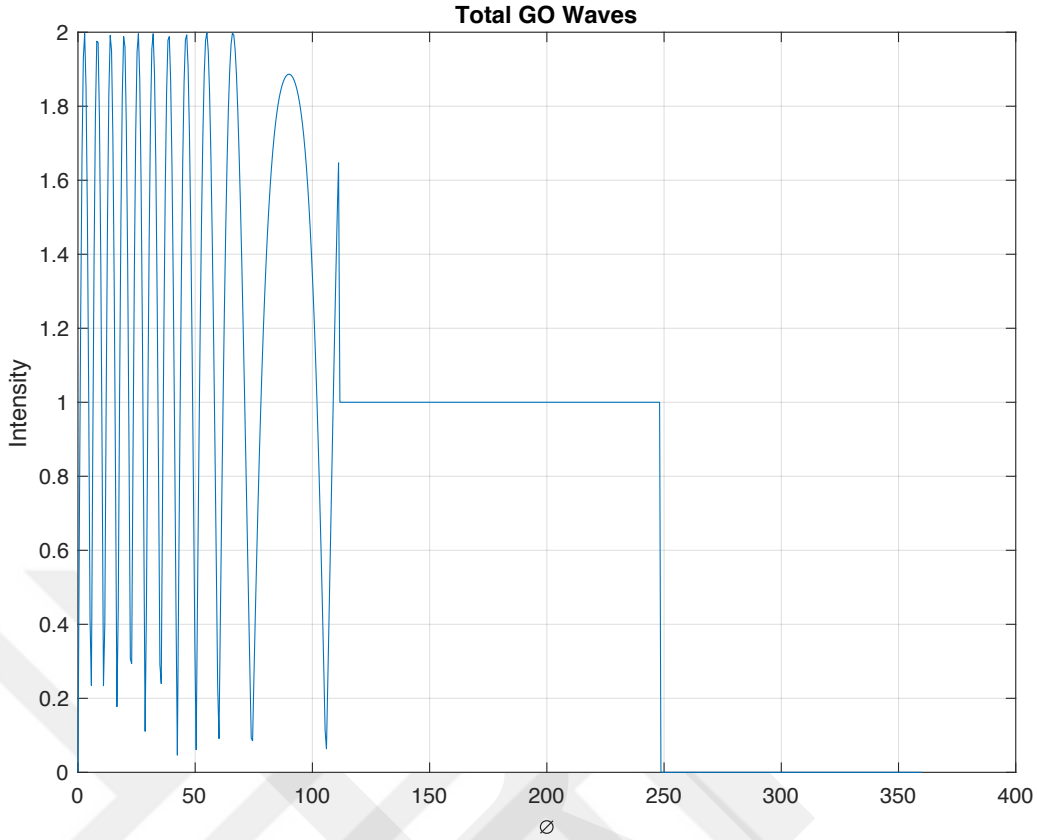

Figure 35. Total GO Waves

6.2. Diffracted Fields Calculation

Geometrical Theory of Diffraction (GTD) [8] is used to calculate diffracted fields by edge points.

6.2.1. Diffracted Fields From +a Point

General GTD formulation for +a point is represented in equation (6.33).

$$E_{d+a} = -\frac{E_0 e^{-\frac{j\pi}{4}}}{2\sqrt{2\pi}}\left[\frac{1}{\cos\left(\frac{\beta_a - \emptyset_0}{2}\right)} - \frac{1}{\cos\left(\frac{\beta_a + \emptyset_0}{2}\right)}\right]\frac{e^{-jkR_a}}{\sqrt{kR_a}}\, Ei(Q) \qquad (6.33)$$

Where

$$Ei(Q) = e^{jkacos(\emptyset_0)}\,. \qquad (6.34)$$

Figure 36 shows the geometry of reflected diffracted fields at +a point.

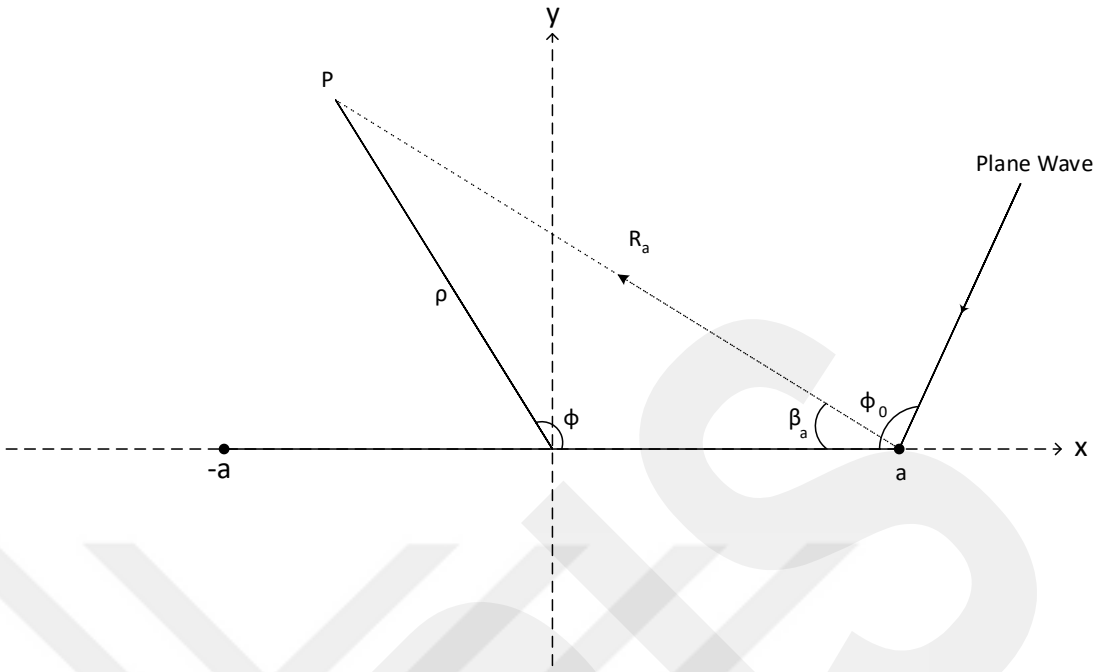

Figure 36. Geometry of Reflected Diffracted Fields

Figure 37 shows the non-uniform diffracted fields at +a point which's equation is showed in equation (6.33).

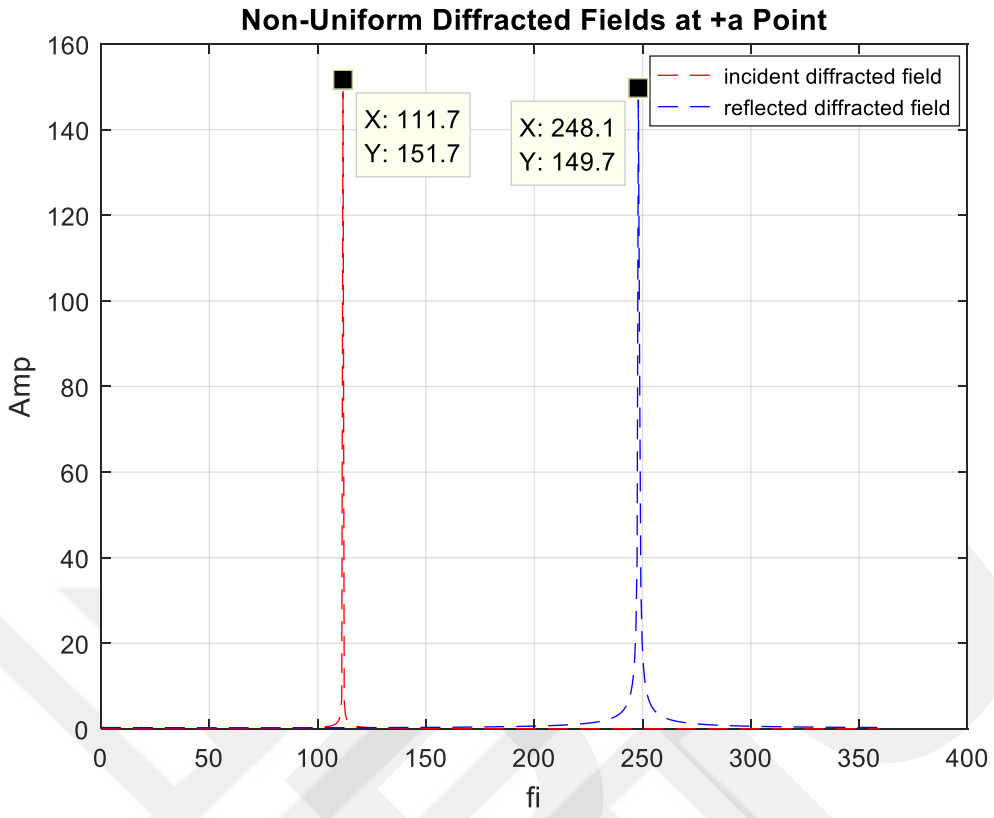

Figure 37. Non-Uniform Diffracted Fields at +a Point

Figure 36 shows that geometry of reflected diffracted fields from +a point. Reflection diffraction formulation is expressed as

$$E_{rd+a} = -\frac{E_0 e^{-\frac{j\pi}{4}}}{2\sqrt{2\pi}} \frac{1}{\cos\left(\frac{\beta_a + \emptyset_0}{2}\right)} \frac{e^{-jkR_a}}{\sqrt{kR_a}}\, e^{jkacos(\emptyset_0)}. \tag{6.35}$$

Where

$$R_a = \sqrt{\rho^2 + a^2 - 2\rho a cos\emptyset}.$$

$$\beta_1 = cos^{-1}\left(\frac{R^2 + a^2 - \rho^2}{2Ra}\right). \tag{6.36}$$

$$\beta_a = \beta_1[U(\emptyset) - U(\emptyset - \pi)] + (-\beta_1 + 2\pi)U(\emptyset - \pi).$$

β_a is introduced in Figure 36. $\emptyset_0$ is angle of incidence at +a point. β_a is angle of scattering at +a point. β_1 is used to find the final form of β_a.

Figure 38 shows the graph of angle of scattering at +a point.

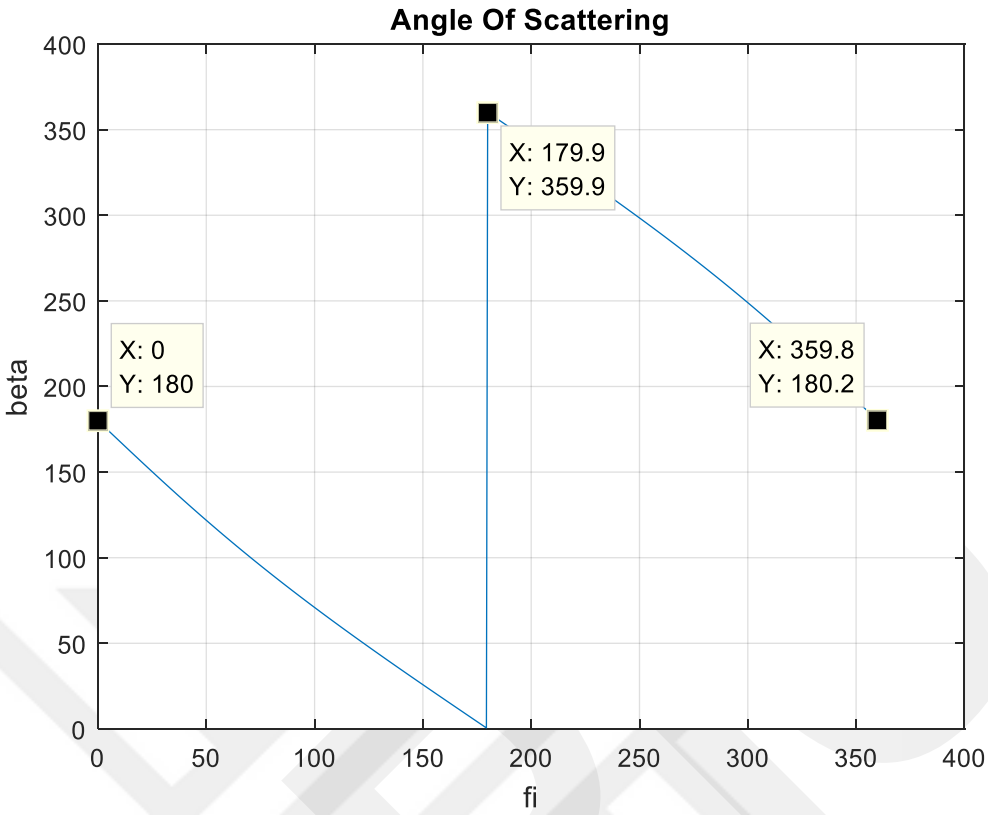

Figure 38. Angle of Scattering

Non-uniform reflected diffracted field at +a point is represented in Figure 39.

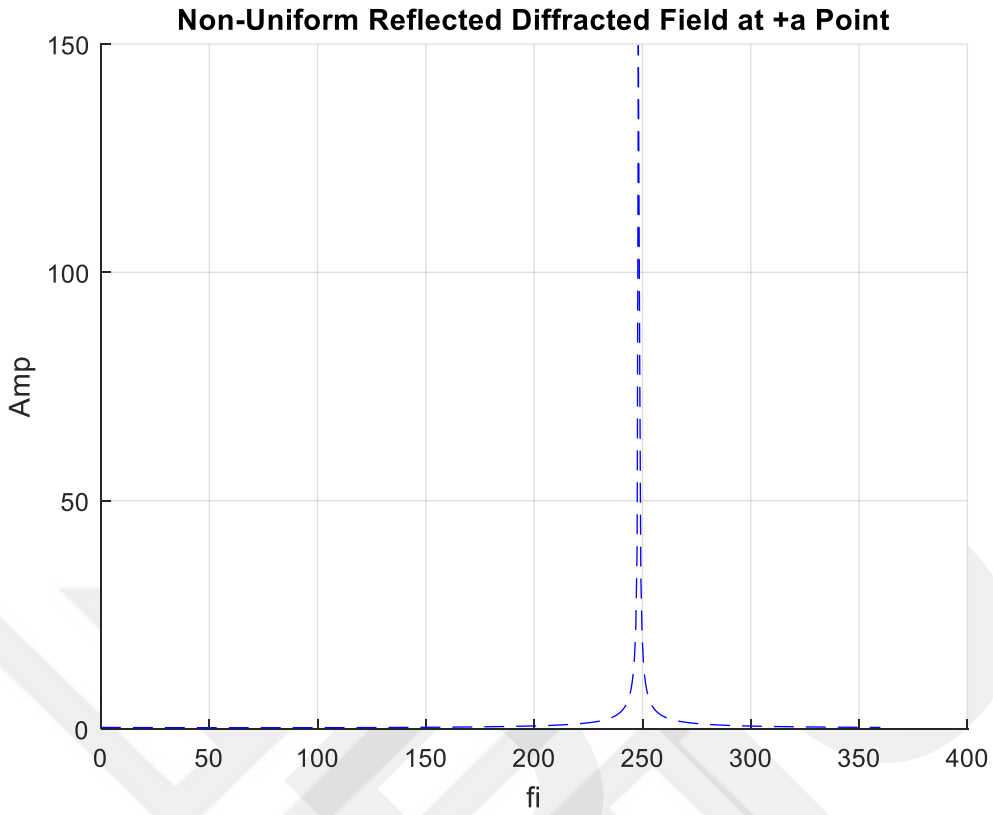

Figure 39. Non-Uniform Reflected Diffracted Field at +a Point

Figure 40 shows that geometry of incident diffracted fields from +a point. Incident diffraction formulation is expressed as

$$E_{id+a} = \frac{E_0 e^{-\frac{j\pi}{4}}}{2\sqrt{2\pi}} \frac{1}{\cos\left(\frac{\beta_a - \emptyset_0}{2}\right)} \frac{e^{-jkR_a}}{\sqrt{kR_a}} e^{jkacos(\emptyset_0)}. \quad (6.37)$$

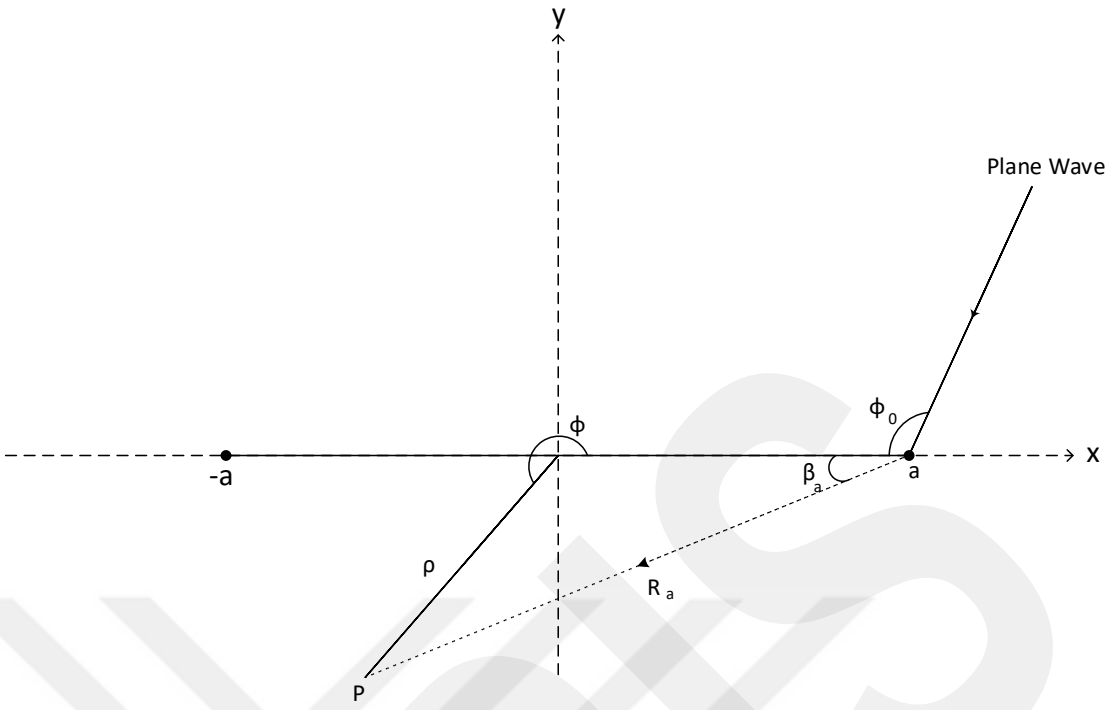

Figure 40. Geometry of Incident Diffracted Fields

Non-uniform reflected diffracted field at +a point is represented in Figure 41.

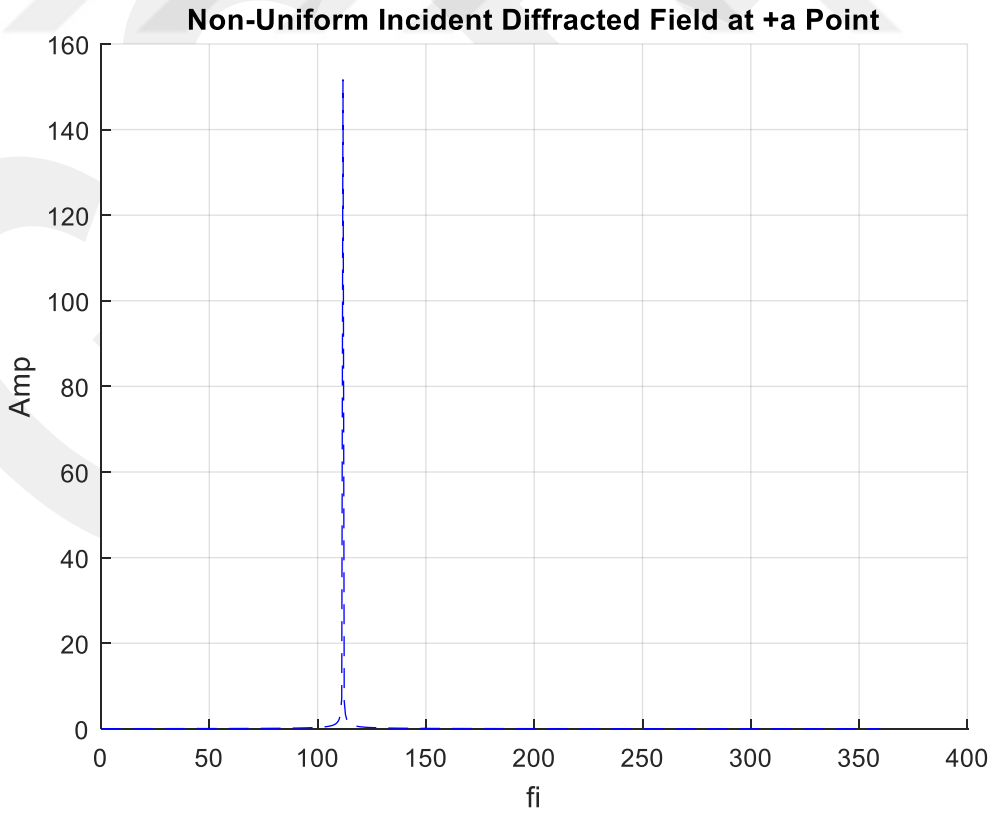

Figure 41. Non-Uniform Incident Diffracted Field at +a Point

6.2.2. Diffracted Fields From -a Point

General GTD formulation for -a point is represented in equation (6.38).

$$E_{d-a} = -\frac{E_0 e^{-\frac{j\pi}{4}}}{2\sqrt{2\pi}}\left[\frac{1}{\cos\left(\frac{\beta_{-a}-\emptyset_0}{2}\right)}-\frac{1}{\cos\left(\frac{\beta_{-a}+\emptyset_0}{2}\right)}\right]\frac{e^{-jkR_{-a}}}{\sqrt{kR_{-a}}}\,Ei(Q) \qquad (6.38)$$

Where

$$Ei(Q) = e^{-jkacos(\emptyset_0)}. \qquad (6.39)$$

Figure 42 shows the geometry of reflected diffracted fields at –a point.

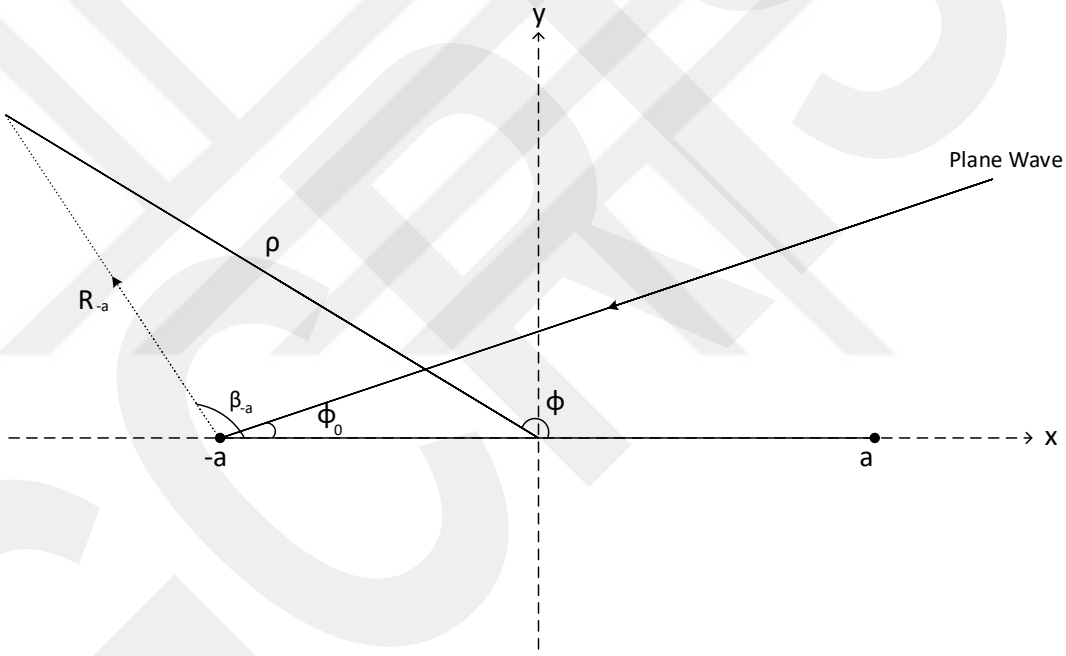

Figure 42. Geometry of Reflected Diffracted Fields

Figure 43 shows the non-uniform diffracted fields at -a point which's equation is showed in equation (6.38).

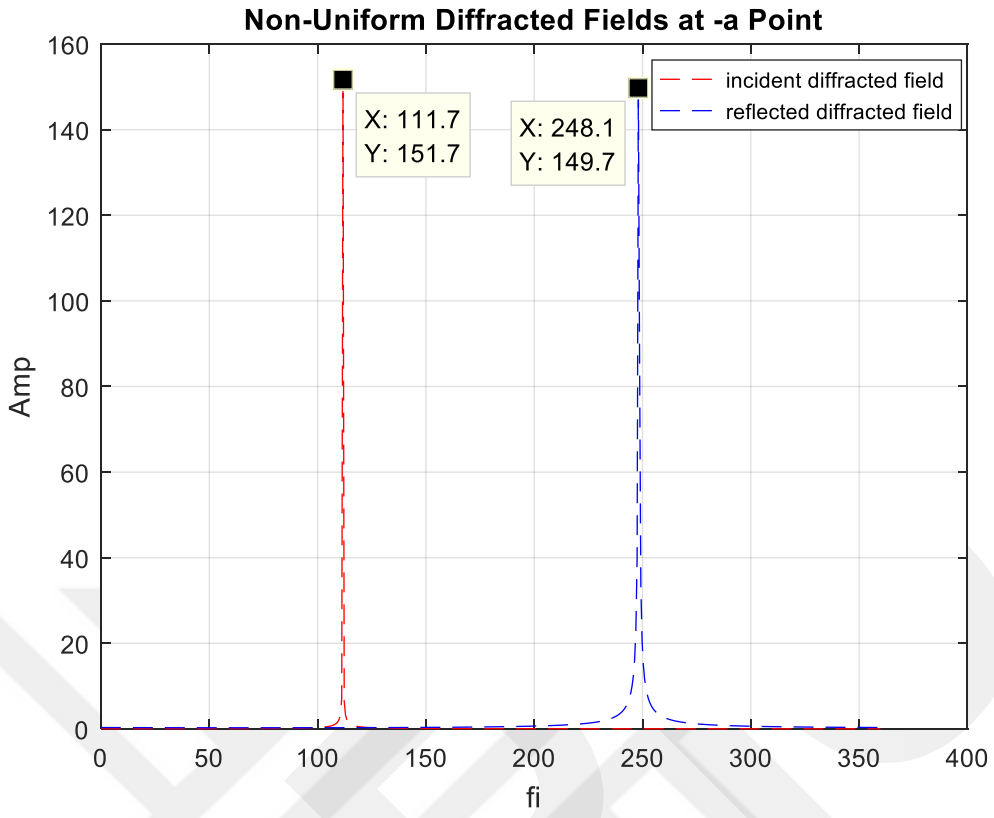

Figure 43. Non-Uniform Diffracted Fields at -a Point

Figure 42 shows that geometry of reflected diffracted fields from -a point. Reflection diffraction formulation is expressed as

$$E_{rd-a} = -\frac{E_0 e^{-\frac{j\pi}{4}}}{2\sqrt{2\pi}} \frac{1}{\cos\left(\frac{\beta_{-a} + \emptyset_0}{2}\right)} \frac{e^{-jkR_{-a}}}{\sqrt{kR_{-a}}} e^{-jkacos(\emptyset_0)}. \tag{6.40}$$

Where

$$R_{-a} = \sqrt{\rho^2 + a^2 + 2\rho a\cos(\pi - \emptyset)}.$$

$$\beta_2 = cos^{-1}\left(-\frac{{R_{-a}}^2 + a^2 - \rho^2}{2R_{-a}a}\right). \tag{6.41}$$

$$\beta_{-a} = \beta_2[U(\emptyset) - U(\emptyset - \pi)] + (-\beta_2 + 2\pi)U(\emptyset - \pi).$$

β_{-a} is introduced in Figure 44. $\emptyset_0$ is angle of incidence at -a point. β_{-a} is angle of scattering at -a point. β_2 is used to find the final form of β_{-a}.

Figure 44 shows the graph of angle of scattering at -a point.

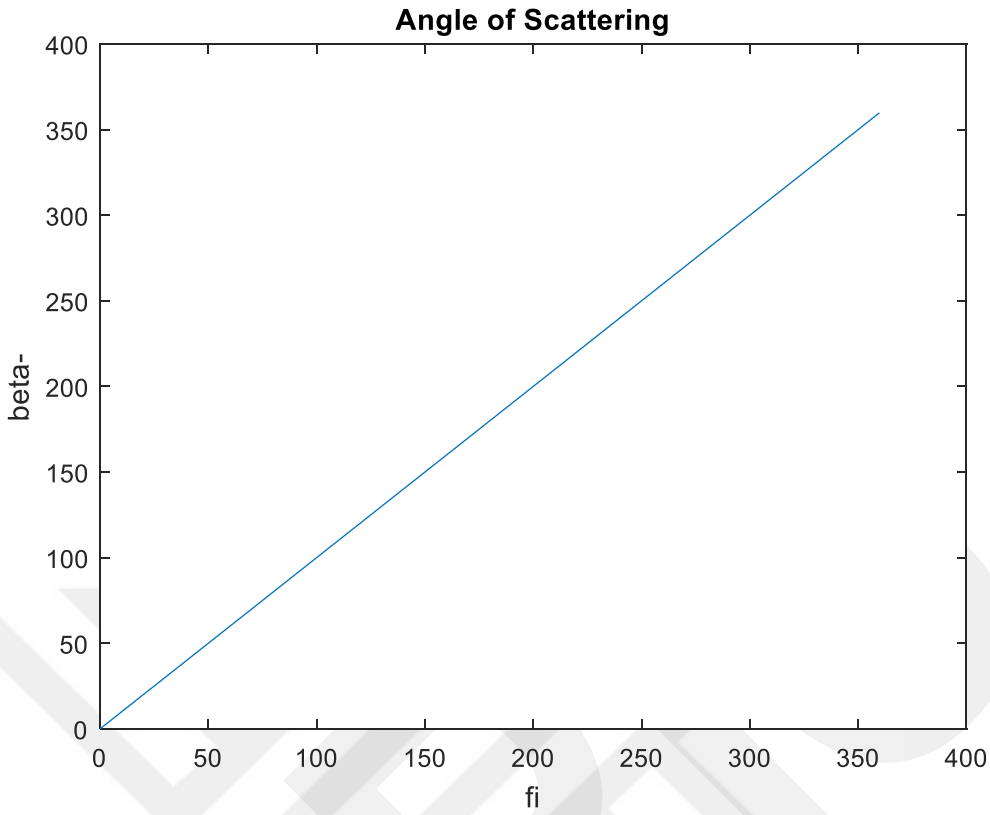

Figure 44. Angle of Scattering

Non-uniform reflected diffracted field at -a point is represented in Figure 45.

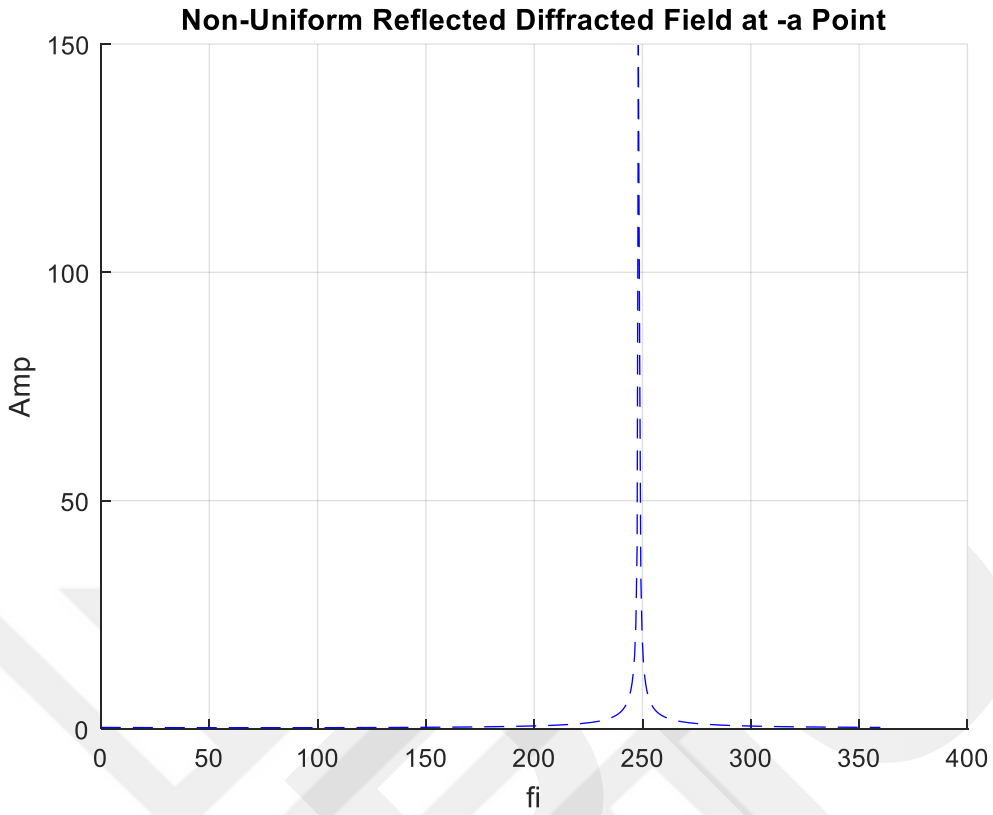

Figure 45. Non-Uniform Reflected Diffracted Field at –a Point

Figure 46 shows that geometry of incident diffracted fields from -a point. Incident diffraction formulation is expressed as

$$E_{id-a} = \frac{E_0 e^{-\frac{j\pi}{4}}}{2\sqrt{2\pi}} \frac{1}{\cos\left(\frac{\beta_{-a} - \emptyset_0}{2}\right)} \frac{e^{-jkR_{-a}}}{\sqrt{kR_{-a}}}\, e^{-jkacos(\emptyset_0)}. \qquad (6.42)$$

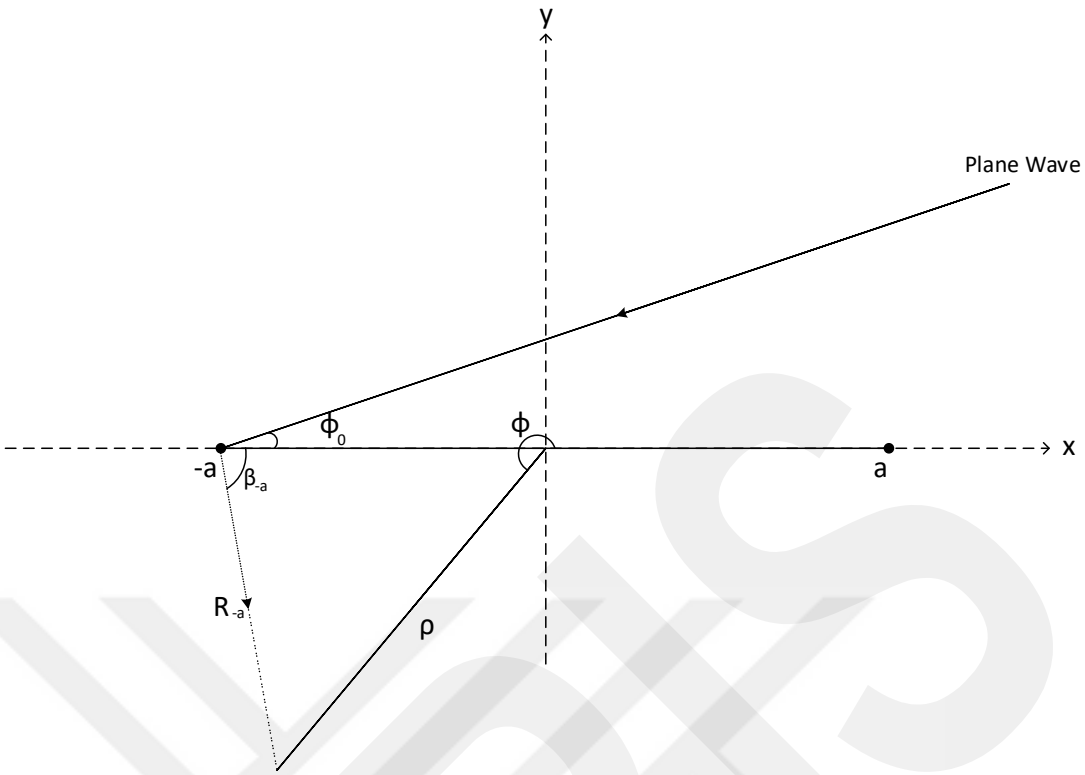

Figure 46. Geometry of Incident Diffracted Fields

Non-uniform reflected diffracted field at -a point is represented in Figure 47.

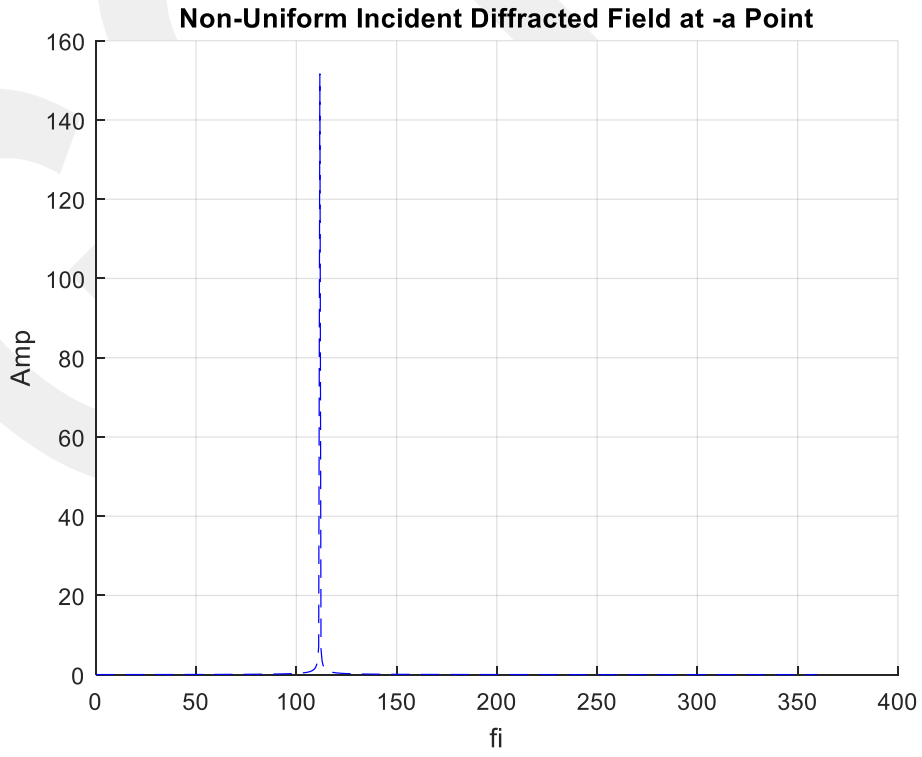

Figure 47. Non-Uniform Incident Diffracted Field at -a Point

6.3. Uniform Diffracted Fields Calculation

Diffracted fields are transient. This problem can be solved with making diffracted fields uniform. Fresnel functions are using to make diffracted fields uniform. Diffracted fields go to infinity which is not appropriate. This problem is solved with Fresnel function.

6.3.1. Fresnel Function

Fresnel function can be expressed as

$$F(x) = \frac{e^{\frac{j\pi}{4}}}{\sqrt{\pi}} \int_{x}^{\infty} e^{-jt^2}\, \partial t. \tag{6.43}$$

When x is equal to $-\infty$, $F(-\infty) = 1$.

$$F(x) - U(-x) = \begin{cases} F(x) & x > 0 \\ F(x) - 1 & x < 0 \end{cases} \tag{6.44}$$

Fresnel function in equation (6.43) is represented in Figure 48.

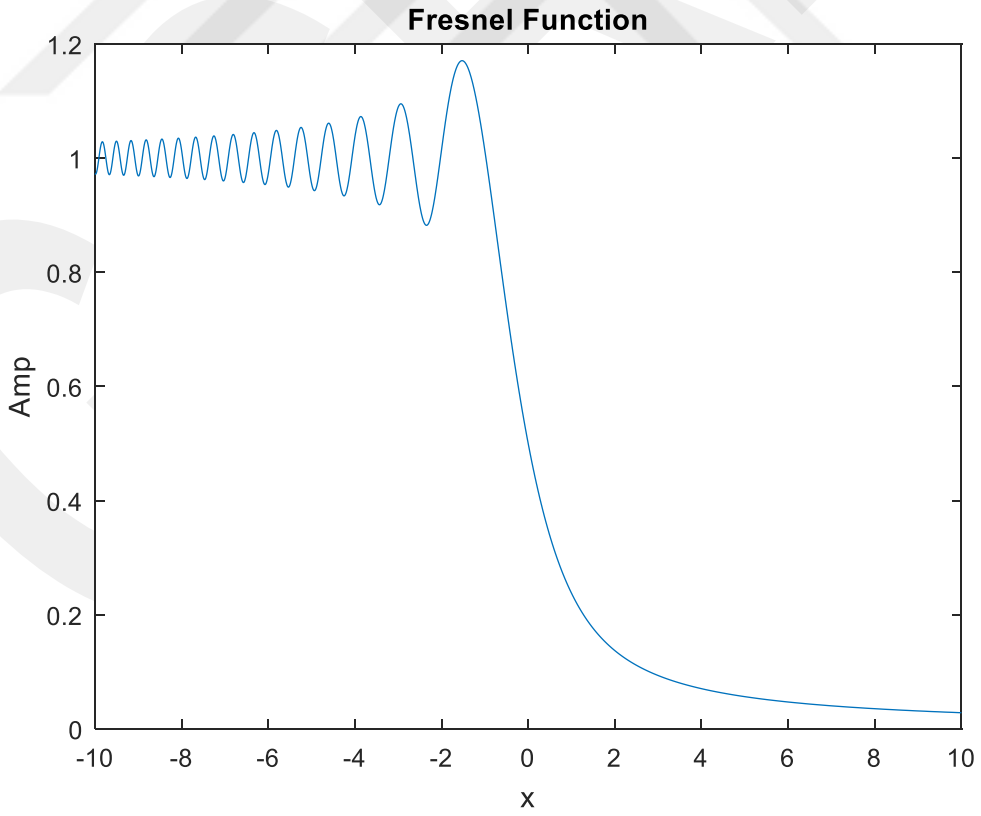

Figure 48. Fresnel Function Graph

Then Fresnel function can be defined as

$$F(x) - 1 = \frac{e^{\frac{j\pi}{4}}}{\sqrt{\pi}} \left[\int_{x}^{\infty} e^{-jt^2}\, \partial t - \int_{-\infty}^{\infty} e^{-jt^2}\, \partial t \right]. \tag{6.45}$$

It becomes as

$$F(x) - 1 = -\frac{e^{\frac{j\pi}{4}}}{\sqrt{\pi}} \int_{-x}^{\infty} e^{-jt^2}\, \partial t = -F(-x). \tag{6.46}$$

Equation (6.44) can be expressed as

$$F(x) - U(-x) = \begin{cases} F(x) & x > 0 \\ -F(-x) & x < 0 \end{cases}. \tag{6.47}$$

This leads us to define Fresnel function as

$$\hat{\mathrm{F}}(\mathrm{x}) = U(-x) + \mathrm{sign(x)F[|x|]}. \tag{6.48}$$

6.3.2. Uniform Diffracted Fields From +a Point

Equation (6.35) and (6.37) can be opened with using trigonometric equation of

$$\cos^2(x) = \frac{1}{2}\,(1 + \cos(2x)). \tag{6.49}$$

Then for using in equation (6.35)

$$e^{-jkR_a} = e^{-jkR_a\left(-\cos(\beta_a+\emptyset_0)+2\cos^2\left(\frac{\beta_a+\emptyset_0}{2}\right)\right)}. \tag{6.50}$$

Using equation (6.50) and equation (6.35) reflected diffracted field can be expressed as

$$E_{rd+a} = -\frac{E_0 e^{-\frac{j\pi}{4}}}{2\sqrt{\pi}} e^{jkR_a(\cos(\beta_a+\emptyset_0))} \frac{e^{-jkR_a 2\cos^2\left(\frac{\beta_a+\emptyset_0}{2}\right)}}{\sqrt{2kR_a}\cos\left(\frac{\beta_a+\emptyset_0}{2}\right)}\, e^{jkacos(\emptyset_0)}. \tag{6.51}$$

Detour parameter for reflected diffracted field at +a can be defined as

$$\zeta_{rd_{+a}} = -\sqrt{2kR_a}\cos\left(\frac{\beta_a+\emptyset_0}{2}\right). \tag{6.52}$$

Then using equation (6.52) uniform reflected diffracted at +a point can be expressed as

$$E_{urd+a} = -e^{jkacos(\emptyset_0)} e^{jkR_a \cos(\beta_a+\emptyset_0)} sign\left(\zeta_{rd_{+a}}\right) F\left(\left|\zeta_{rd_{+a}}\right|\right). \quad (6.53)$$

Figure 49 shows the uniform reflected diffracted field at +a point and it is graph of equation (6.53).

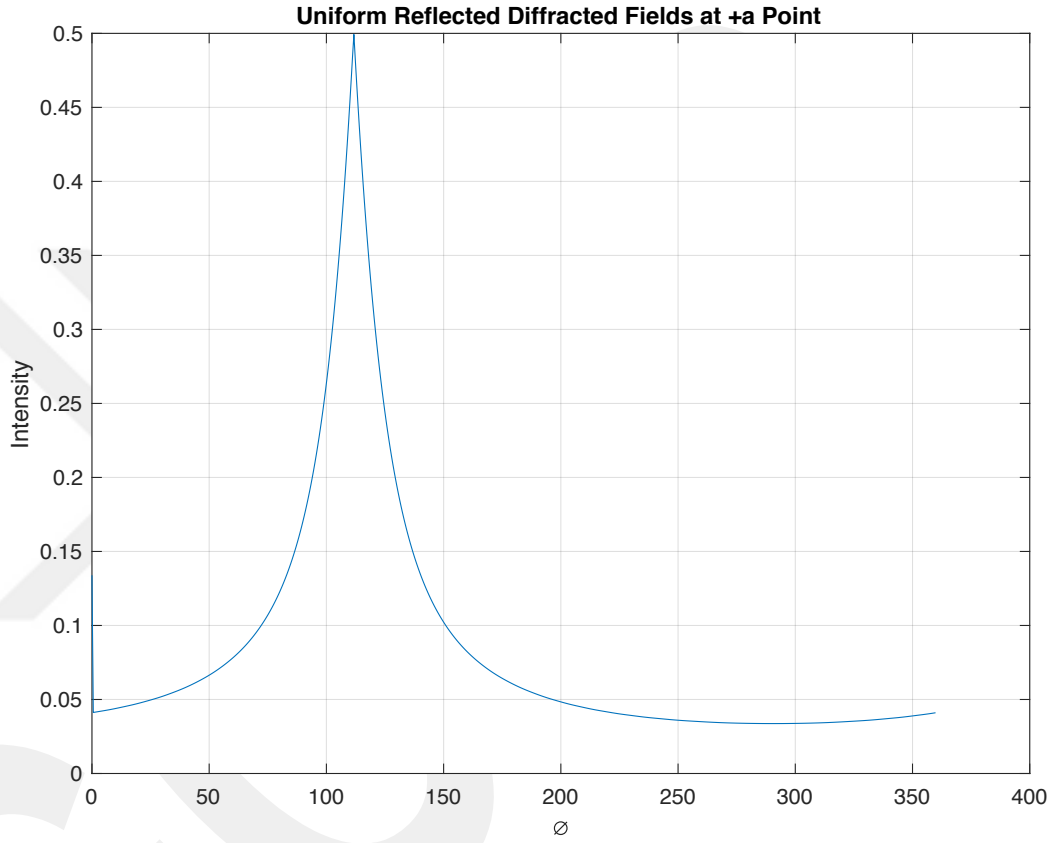

Figure 49. Uniform Reflected Diffracted Field at +a Point

For incident diffracted field

$$e^{-jkR_a} = e^{-jkR_a\left(-\cos(\beta_a-\emptyset_0)+2\cos^2\left(\frac{\beta_a-\emptyset_0}{2}\right)\right)}. \quad (6.54)$$

Using equation (6.54) and equation (6.37) incident diffracted field can be expressed as

$$E_{id+a} = \frac{E_0 e^{-\frac{j\pi}{4}}}{2\sqrt{\pi}} e^{jkR_a(\cos(\beta_a - \emptyset_0))} \frac{e^{-jkR_a 2\cos^2\left(\frac{\beta_a - \emptyset_0}{2}\right)}}{\sqrt{2kR_a}\cos\left(\frac{\beta_a - \emptyset_0}{2}\right)} e^{jkacos(\emptyset_0)}. \quad (6.55)$$

Detour parameter for incident diffracted field at +a can be defined as

$$\zeta_{id+a} = -\sqrt{2kR_a}\cos\left(\frac{\beta_a - \emptyset_0}{2}\right). \quad (6.56)$$

Then using equation (6.52) uniform incident diffracted at +a point can be expressed as

$$E_{uid+a} = e^{jkacos(\emptyset_0)} e^{jkR_a\cos(\beta_a - \emptyset_0)} sign(\zeta_{id+a}) F(|\zeta_{id+a}|). \quad (6.57)$$

Figure 50 shows the uniform incident diffracted field at +a point and it is graph of equation (6.57).

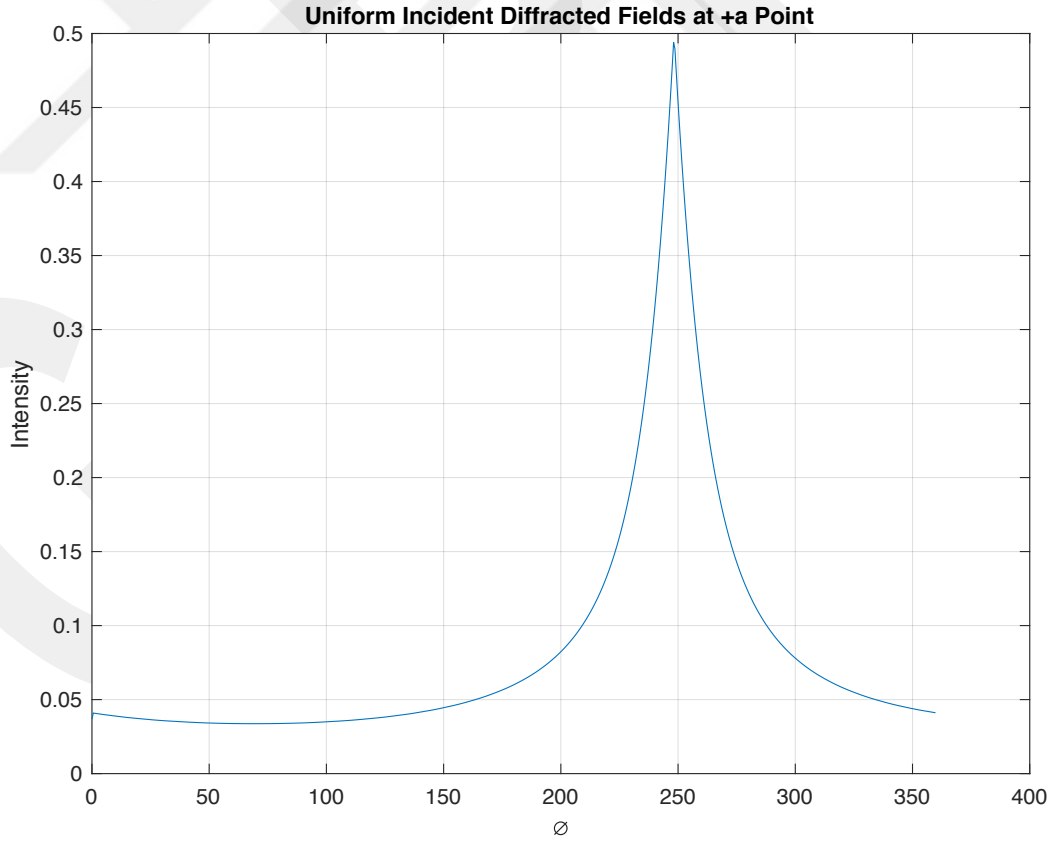

Figure 50. Uniform Incident Diffracted Field at +a Point

Equation (6.53) and equation (6.57) shows the uniform diffracted fields from +a point. The total uniform diffracted fields can be expressed with summing these two fields. Equation (6.58) shows the total diffracted fields from +a point.

$$E_{ud+a} = e^{jkacos(\emptyset_0)} e^{jkR_a \cos(\beta_a - \emptyset_0)} sign(\zeta_{id+a}) F(|\zeta_{id+a}|) - e^{jkacos(\emptyset_0)} e^{jkR_a \cos(\beta_a + \emptyset_0)} sign(\zeta_{rd+a}) F(|\zeta_{rd+a}|) \quad (6.58)$$

Figure 51 shows the uniform total diffracted field at +a point and it is graph of equation (6.58).

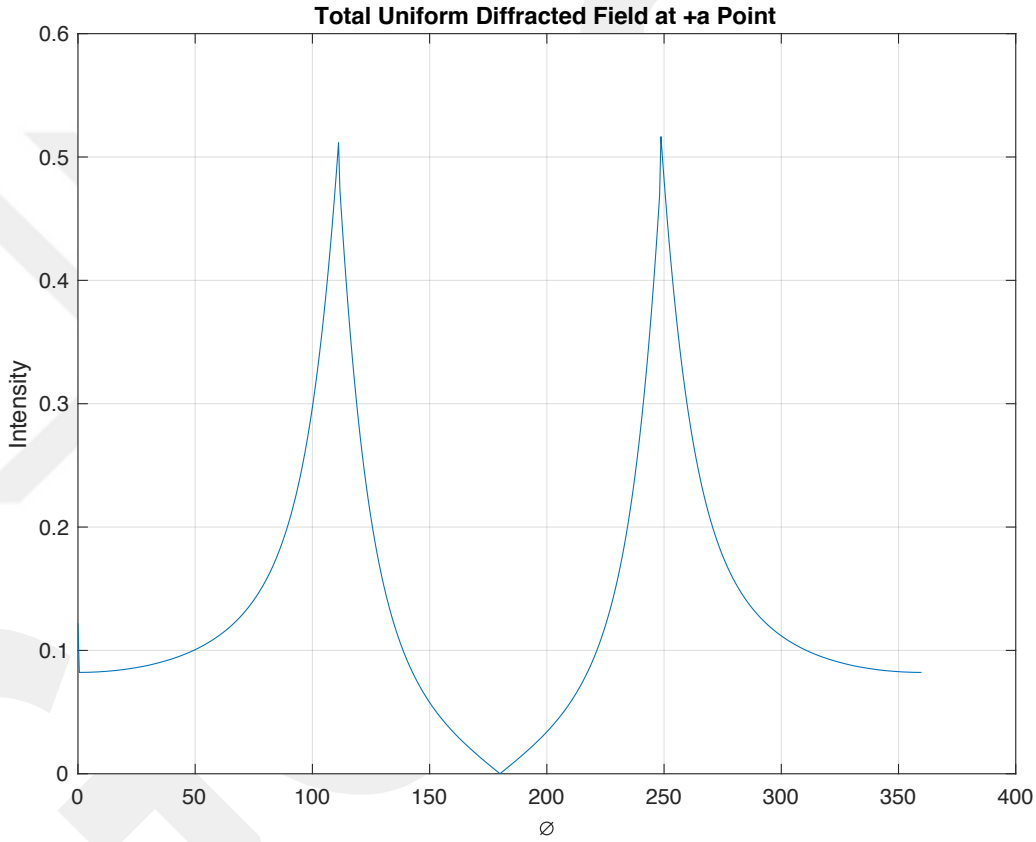

Figure 51. Total Uniform Diffracted Field at +a Point

6.3.3. Uniform Diffracted Fields From -a Point

Equations (6.40) and (6.42) can be opened with using trigonometric equation in equation

$$\cos^2(x) = \frac{1}{2}\,(1 + \cos(2x)). \tag{6.59}$$

Then for using in equation (6.40)

$$e^{-jkR_{-a}} = e^{-jkR_{-a}\left(-\cos(\beta_{-a}+\emptyset_0)+2\cos^2\left(\frac{\beta_{-a}+\emptyset_0}{2}\right)\right)}. \tag{6.60}$$

Using equation (6.60) and equation (6.40) reflected diffracted field can be expressed as

$$E_{rd-a}$$
$$= -\frac{E_0 e^{-\frac{j\pi}{4}}}{2\sqrt{\pi}}\, e^{jkR_{-a}(\cos(\beta_{-a}+\emptyset_0))}\, \frac{e^{-jkR_{-a}2\cos^2\left(\frac{\beta_{-a}+\emptyset_0}{2}\right)}}{\sqrt{2kR_{-a}}\cos\left(\frac{\beta_{-a}+\emptyset_0}{2}\right)}\, e^{-jkacos(\emptyset_0)}. \tag{6.61}$$

Detour parameter for reflected diffracted field at -a can be defined as

$$\zeta_{rd_{-a}} = \sqrt{2kR_{-a}}\cos\left(\frac{\beta_{-a}+\emptyset_0}{2}\right). \tag{6.62}$$

Then using equation (6.62) uniform reflected diffracted at -a point can be expressed as

$$E_{urd-a} = -e^{-jkacos(\emptyset_0)} e^{jkR_{-a}\cos(\beta_{-a}+\emptyset_0)} sign\left(\zeta_{rd_{-a}}\right) F\left(\left|\zeta_{rd_{-a}}\right|\right). \tag{6.63}$$

Figure 52 shows the uniform reflected diffracted field at -a point and it is graph of equation (6.63).

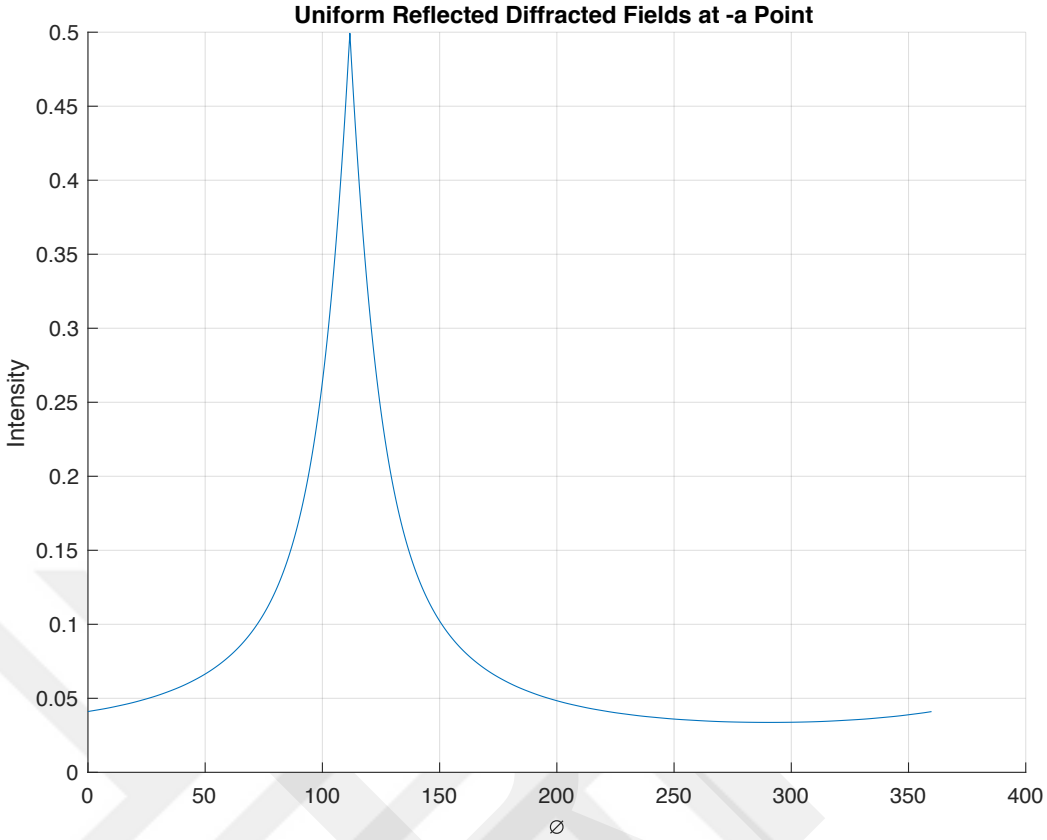

Figure 52. Uniform Reflected Diffracted Field at -a Point

For incident diffracted field

$$e^{-jkR_{-a}} = e^{-jkR_{-a}\left(-\cos(\beta_{-a}-\emptyset_0)+2\cos^2\left(\frac{\beta_{-a}-\emptyset_0}{2}\right)\right)}. \tag{6.64}$$

Using equation (6.64) and equation (6.42) incident diffracted field can be expressed as

$$E_{id-a} = \frac{E_0 e^{-\frac{j\pi}{4}}}{2\sqrt{\pi}} e^{jkR_{-a}(\cos(\beta_{-a}-\emptyset_0))} \frac{e^{-jkR_{-a}2\cos^2\left(\frac{\beta_{-a}-\emptyset_0}{2}\right)}}{\sqrt{2kR_{-a}}\cos\left(\frac{\beta_{-a}-\emptyset_0}{2}\right)} e^{-jkacos(\emptyset_0)}. \tag{6.65}$$

Detour parameter for incident diffracted field at -a can be defined as

$$\zeta_{id_{-a}} = \sqrt{2kR_{-a}}\cos\left(\frac{\beta_{-a}-\emptyset_0}{2}\right). \tag{6.66}$$

Then using equation (6.66) uniform incident diffracted at -a point can be expressed as

$$E_{uid-a} = e^{-jkacos(\emptyset_0)} e^{jkR_{-a}\cos(\beta_{-a}-\emptyset_0)} sign(\zeta_{id_{-a}}) F(|\zeta_{id_{-a}}|). \quad (6.67)$$

Figure 53 shows the uniform reflected diffracted field at -a point and it is graph of equation (6.67).

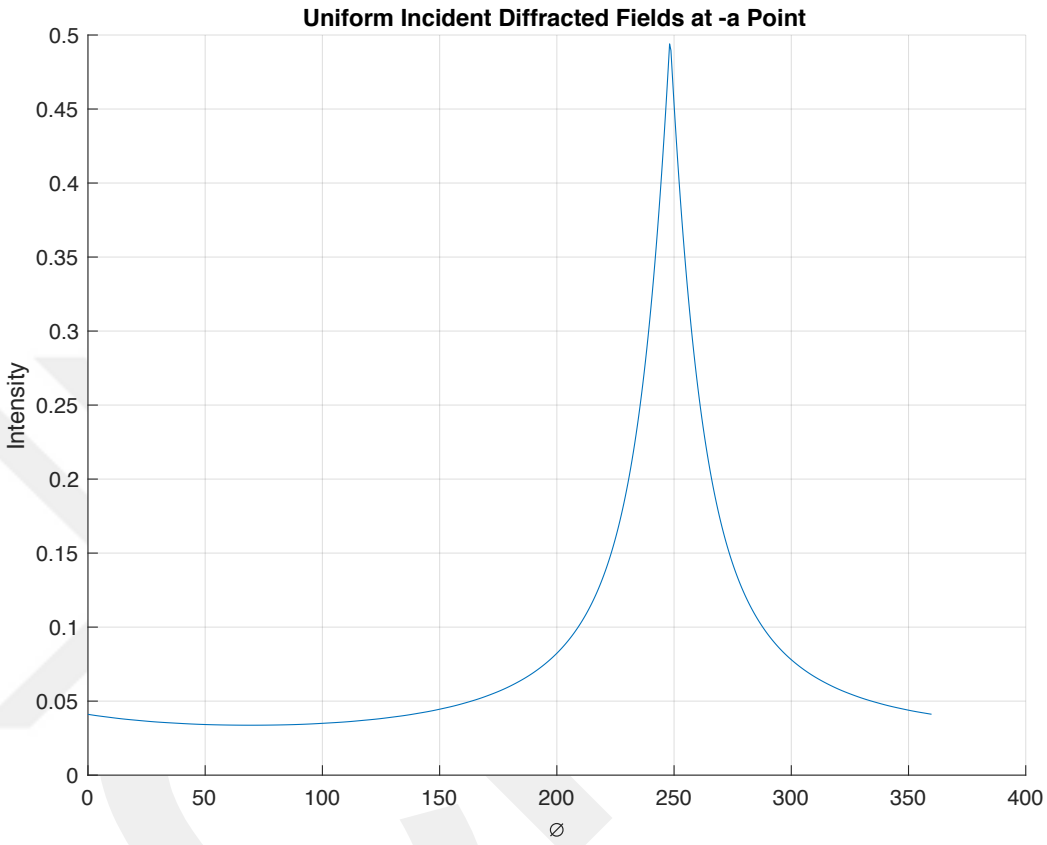

Figure 53. Uniform Incident Diffracted Field at -a Point

Equation (6.63) and equation (6.67) shows the uniform diffracted fields from -a point. The total uniform diffracted fields can be expressed with summing these two fields. Equation (6.68) shows the total diffracted fields from -a point.

$$\begin{aligned} E_{ud-a} = {} & e^{-jkacos(\emptyset_0)} e^{jkR_{-a}\cos(\beta_{-a}-\emptyset_0)} sign(\zeta_{id_{-a}}) F(|\zeta_{id_{-a}}|) \\ & - e^{-jkacos(\emptyset_0)} e^{jkR_{-a}\cos(\beta_{-a}+\emptyset_0)} sign(\zeta_{rd_{-a}}) F(|\zeta_{rd_{-a}}|) \end{aligned} \quad (6.68)$$

Figure 54 shows the uniform reflected diffracted field at -a point and it is graph of equation (6.68)

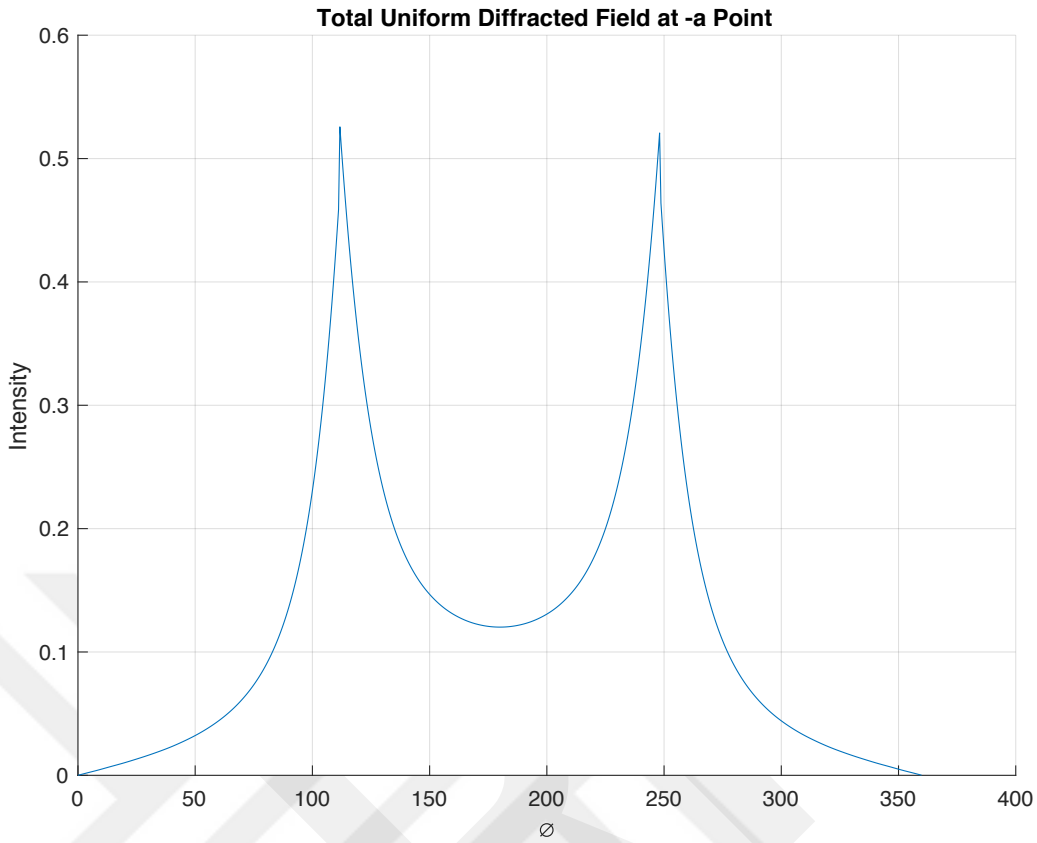

Figure 54. Total Uniform Diffracted Field at -a Point

6.4. Scattered Fields

In order to find total scattered fields, diffracted fields and GO waves should be summed.

6.4.1. Total Scattered Fields by Line Strip from 0 to +a

Total scattered field can be calculated by gathering equation (6.29) and equation (6.58) for line strip from 0 to +a. It is expressed as

$$\begin{aligned} E_{ts+a} = {} & E_0 e^{jk\rho cos(\emptyset-\emptyset_0)}\ U(-\zeta_{id+a}) - E_0 e^{jk\rho cos(\emptyset+\emptyset_0)} U(-\zeta_{rd+a}) \\ & + e^{jkacos(\emptyset_0)} e^{jkR_a \cos(\beta_a-\emptyset_0)} sign(\zeta_{id+a}) F(|\zeta_{id+a}|) \\ & - e^{jkacos(\emptyset_0)} e^{jkR_a \cos(\beta_a+\emptyset_0)}\ sign(\zeta_{rd+a}) F(|\zeta_{rd+a}|). \end{aligned} \tag{6.69}$$

Figure 55 shows the uniform total scattered fields by line strip from 0 to a and it is graph of equation (6.69).

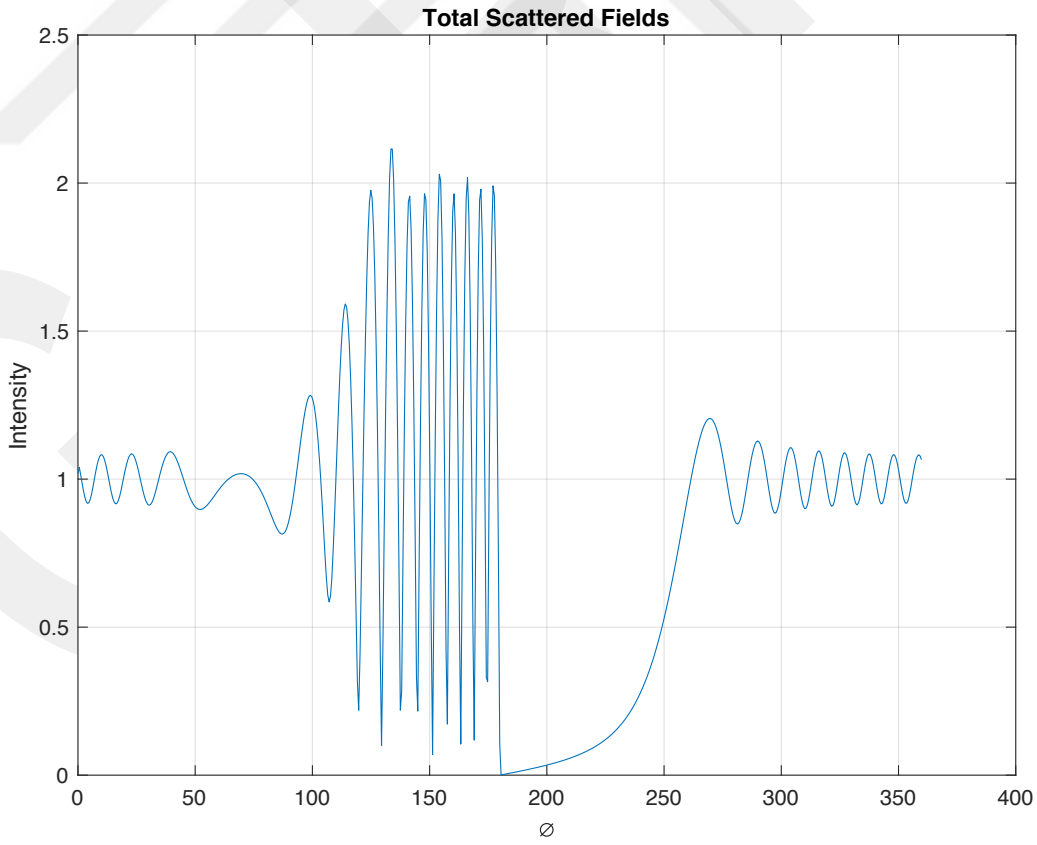

Figure 55. Total Scattered Fields by Line Strip from 0 to a

The polar figure for total scattered fields by line strip from 0 to a is shown in Figure 56.

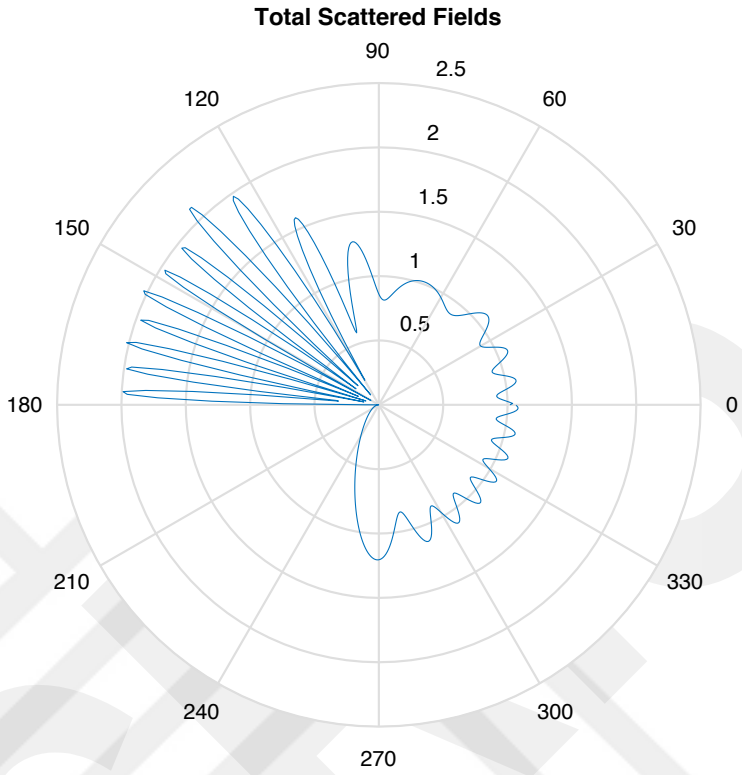

Figure 56. Total Scattered Fields by Line Strip from 0 to a

In Figure 55 and Figure 56, it is clearly seen that incident GO wave is appearing between 0° and 180° and between 248.1° and 360°. Reflected GO field is appearing between 111.7° and 180°. The interference of incident and reflected GO fields is observed between 111.7° and 180°. Also, as can be seen from Figure 51 that the uniform diffracted fields are interfering with GO waves between 0° and 360°. The maximum amplitude value of reflected diffracted field is observed at 111.7°. Incident diffracted field takes the maximum amplitude value is observed at 248.1°. There is a shadow region between 180° and 248.1°.

6.4.2. Total Scattered Fields by Line Strip from -a to 0

Total scattered fields can be calculated by gathering equation (6.32) and equation (6.68) for line strip from -a to 0. It is expressed as

$$\begin{aligned} E_{ts+a} = {} & E_0 e^{jk\rho cos(\emptyset-\emptyset_0)}\ U(-\zeta_{id-a}) - E_0 e^{jk\rho cos(\emptyset+\emptyset_0)} U(-\zeta_{rd-a}) \\ & + e^{-jkacos(\emptyset_0)} e^{jkR_{-a}\cos(\beta_{-a}-\emptyset_0)} sign(\zeta_{id_{-a}}) F(|\zeta_{id_{-a}}|) \\ & - e^{-jkacos(\emptyset_0)} e^{jkR_{-a}\cos(\beta_{-a}+\emptyset_0)} sign(\zeta_{rd_{-a}}) F(|\zeta_{rd_{-a}}|). \end{aligned} \tag{6.70}$$

Figure 57 shows the uniform total scattered fields by line strip from -a to 0 and it is graph of equation (6.70).

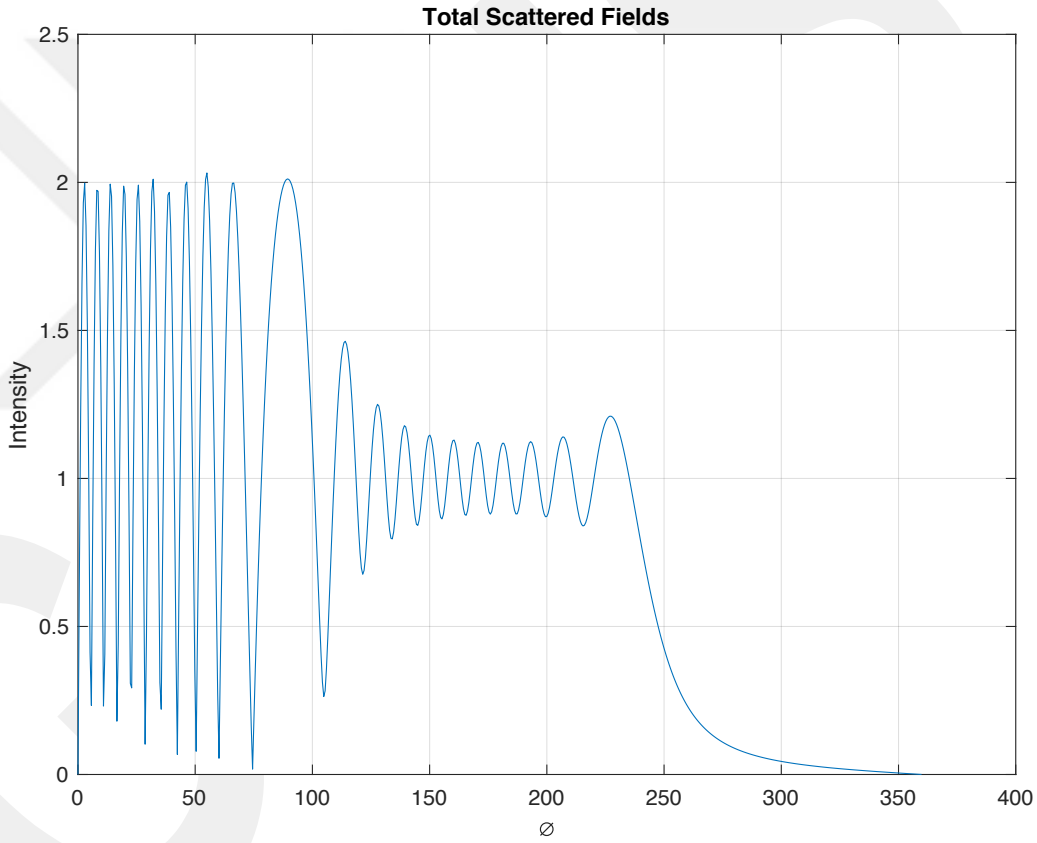

Figure 57. Total Scattered Fields by Line Strip from -a to 0

The polar figure for total scattered fields by line strip from -a to 0 is shown in Figure 58.

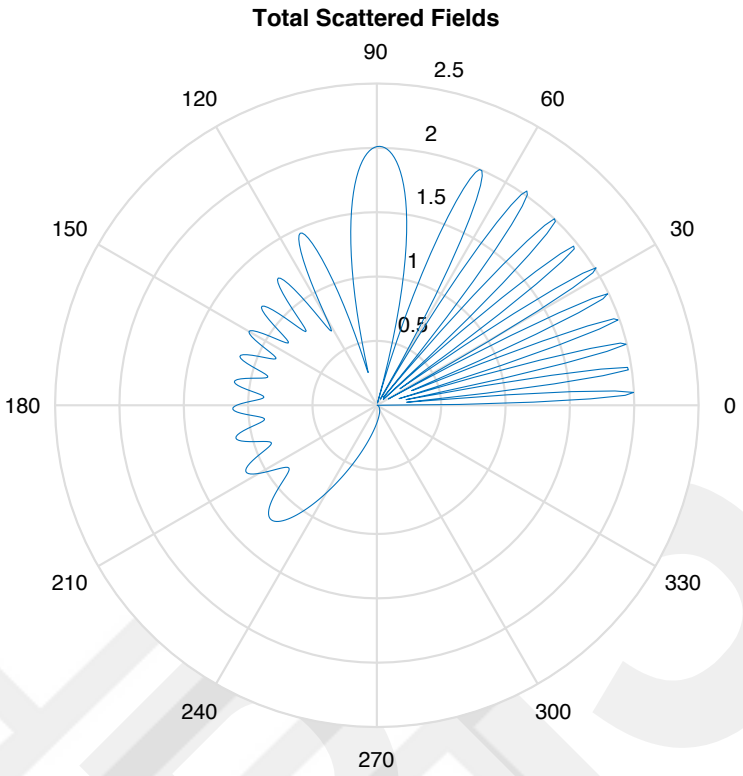

Figure 58. Total Scattered Fields by Line Strip from -a to 0

In Figure 57 and Figure 58, it is clearly seen that incident GO waves is appearing between 0° and 248.1°. Reflected GO field is appearing between 0° and 111.7°. The interference of incident and reflected GO fields is observed between 0° and 111.7°. Also, as can be seen Figure 54 that the diffracted fields are interfering with GO waves between 0° and 360°. The maximum amplitude value of reflected diffracted field is observed at 111.7°. Incident diffracted field takes the maximum amplitude value is observed at 248.1°. There is a shadow region between 248.1° and 360°.

6.4.3. Total Scattered Fields

Total scattered fields can be calculated by gathering equation (6.69) and equation (6.70). It is expressed as

$$E_{ts+a} = E_{ts+a} + E_{ts-a}. \tag{6.71}$$

The polar figure for total scattered fields is shown in Figure 59.

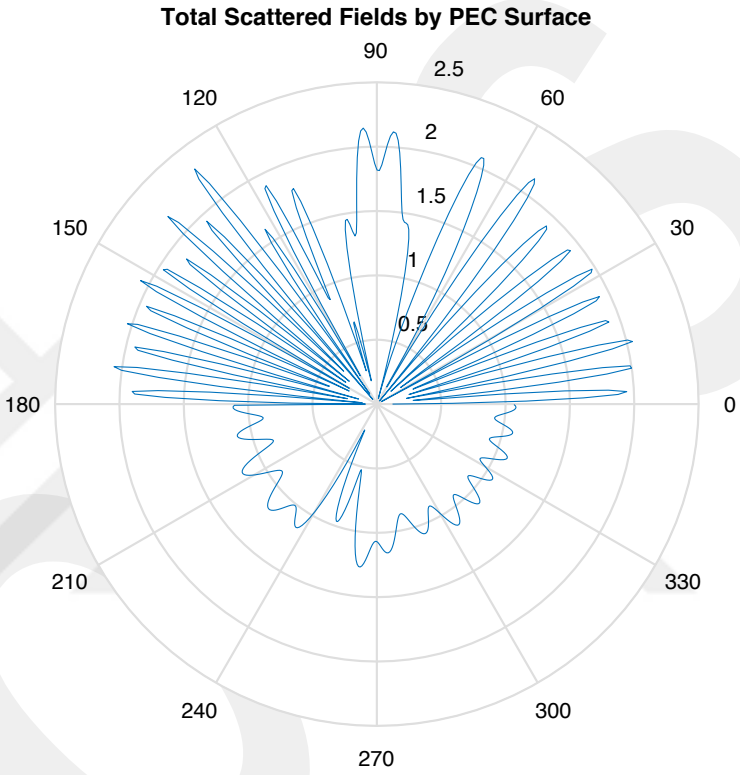

Figure 59. Total Scattered Field by PEC Surface

In Figure 59, it is shown that incident GO wave and reflected GO wave which are scattering by line strip from -a to a and uniform diffracted fields which are scattered by edge points are interfered between 0° and 180°. Incident GO wave which is scattering by line strip from -a and a and uniform diffracted fields which are scattered by edge points are interfered between 180° and 360°. Also, it is apparent that incident GO wave exists between 0° and 360°. There is shadow region around 244.7°.

CHAPTER 7

7. SCATTERED FIELDS BY STEALTH AIRCRAFT

Stealth aircrafts are coated by absorbing materials. Stealth aircraft's body will be modeled as perfectly absorbing strip. Lockheed Martin which is one of the biggest aircraft company in USA has manufactured Lockheed F-117 Nighthawk as stealth aircraft. We will model stealth aircraft dimensions as Lockheed F-117 Nighthawk's dimensions which is shown in Figure 60.

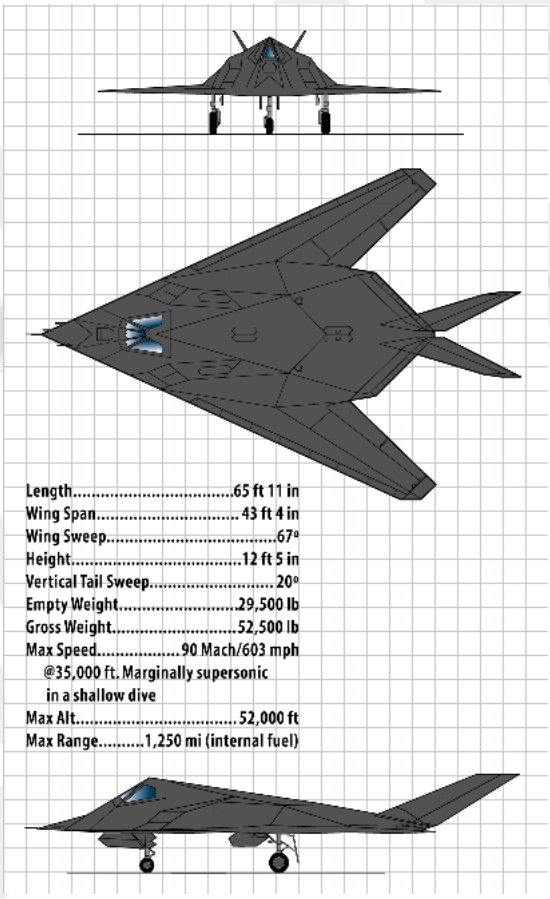

Figure 60. Lockheed F-117 Nighthawk's dimensions, [90].

In the far field, electromagnetic fields which are radiated from satellite will be plane wave. Here, plane is modeled as strip which defines that half-length of the strip(a) is equal to 10.0407m. Geometrical optics fields and diffracted fields are investigated. MTPO method is used in order to find fields.

In this thesis, line strip is divided two parts which are from 0 to +a and from -a to 0. Evaluations are done for these two line strips. Scattered fields by line strip from -a to +a is found by summation of scattered fields by line strip from 0 to +a and scattered fields by line strip from -a to 0.

Scattered fields by stealth aircraft is found uniform in this section. Attenuations are not implicated in simulations. Attenuation, real ranges are considered in Section 8.1, 8.3.

Simulations are done with parameters of

$\lambda = 0.1$m.

$\rho = 6\lambda$.

$a = \lambda$.

A perfectly absorbing surface neither reflects nor transmits the incident radiation, [72]. Perfectly absorbing surface is actually summation of soft and hard surface. In this thesis soft surface line strip is investigated in Section 6. Also, Umul is investigated soft and hard surface solution for strip, [66]. In the journal, it is apparent that,

$$\begin{aligned} {U_{GO}}^{s} &= {U_{GO}}^{h}, \\ {U_{id}}^{s} &= {U_{id}}^{h}, \\ {U_{rd}}^{s} &= -{U_{rd}}^{h}. \end{aligned} \tag{7.1}$$

In perfectly absorbing surface(PAS), there is no reflected GO wave, [73]. By using equation (7.1), perfectly absorbing surface can be evaluated as

$$\begin{aligned} {U_{GO}}^{PAS} &= U_{igo}, \\ {U_{d}}^{PAS} &= U_{id}. \end{aligned} \tag{7.2}$$

Also, Umul's journal about the new representation of the Kirchhof Diffraction Integral is proof. It is apparent that soft (total field is equal to zero on the surface) surface integral can be shown as

$$U(P) = \frac{jk}{4\pi} \oiint U_i(Q) \frac{e^{-jkR}}{R} \left[\sin\left(\frac{\beta - \emptyset_0}{2}\right) - \sin\left(\frac{\beta + \emptyset_0}{2}\right)\right] dS'. \tag{7.3}$$

And hard (normal derivative of the total field is equal to zero on the surface) surface scattering integral can be expressed as

$$U(P) = \frac{jk}{4\pi} \oiint U_i(Q) \frac{e^{-jkR}}{R} \left[\sin\left(\frac{\beta - \emptyset_0}{2}\right) + \sin\left(\frac{\beta + \emptyset_0}{2}\right) \right] dS'. \quad (7.4)$$

Summation of (7.3) and (7.4) is giving another perspective for (7.2).

7.1. GO Waves by Line Strip from 0 to +a

Scattered GO waves from PAS with limitation for line strip from 0 to +a is shown as

$$E_i^{GO} = E_0 e^{jk\rho cos(\emptyset - \emptyset_0)} \; U(-\zeta_{id+a}). \quad (7.5)$$

Scattered GO waves can be shown in Figure 61.

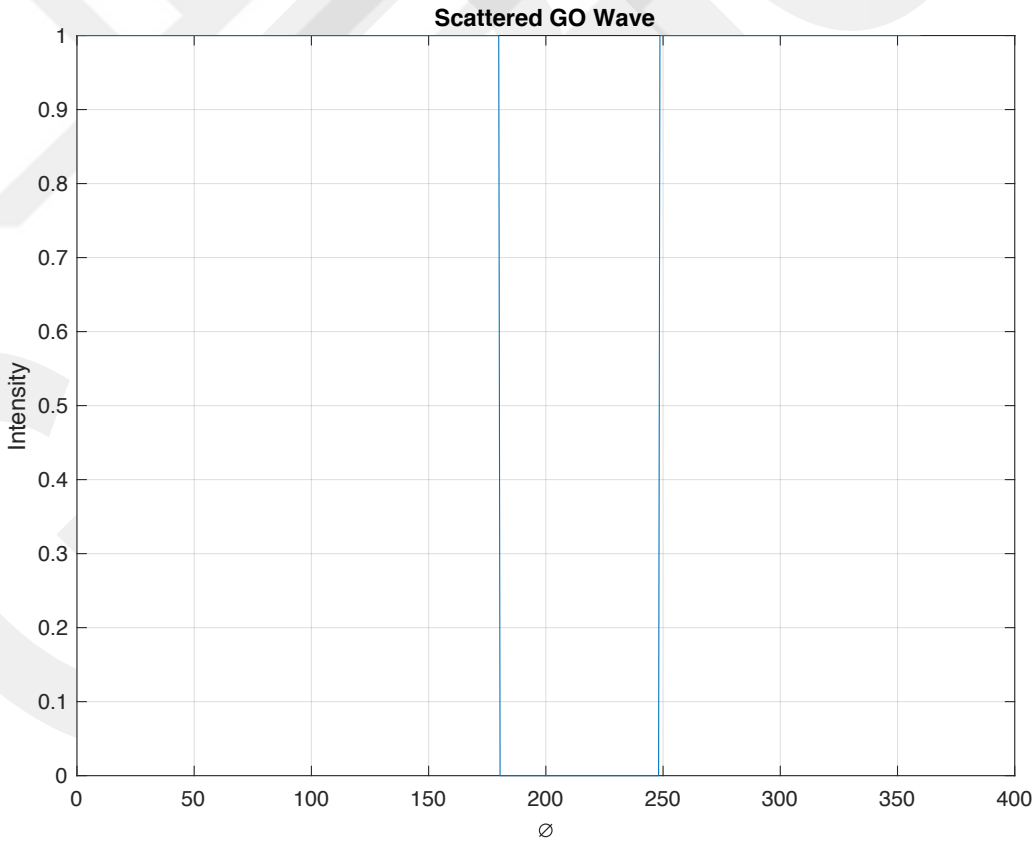

Figure 61. Scattered GO Wave

7.2. GO Waves by Line Strip from -a to 0

Scattered GO waves from PAS with limitation for line strip from -a to 0 is shown as

$$E_i^{GO} = E_0 e^{jk\rho cos(\emptyset - \emptyset_0)} \; U(-\zeta_{id-a}). \tag{7.6}$$

Scattered GO waves can be shown in Figure 62.

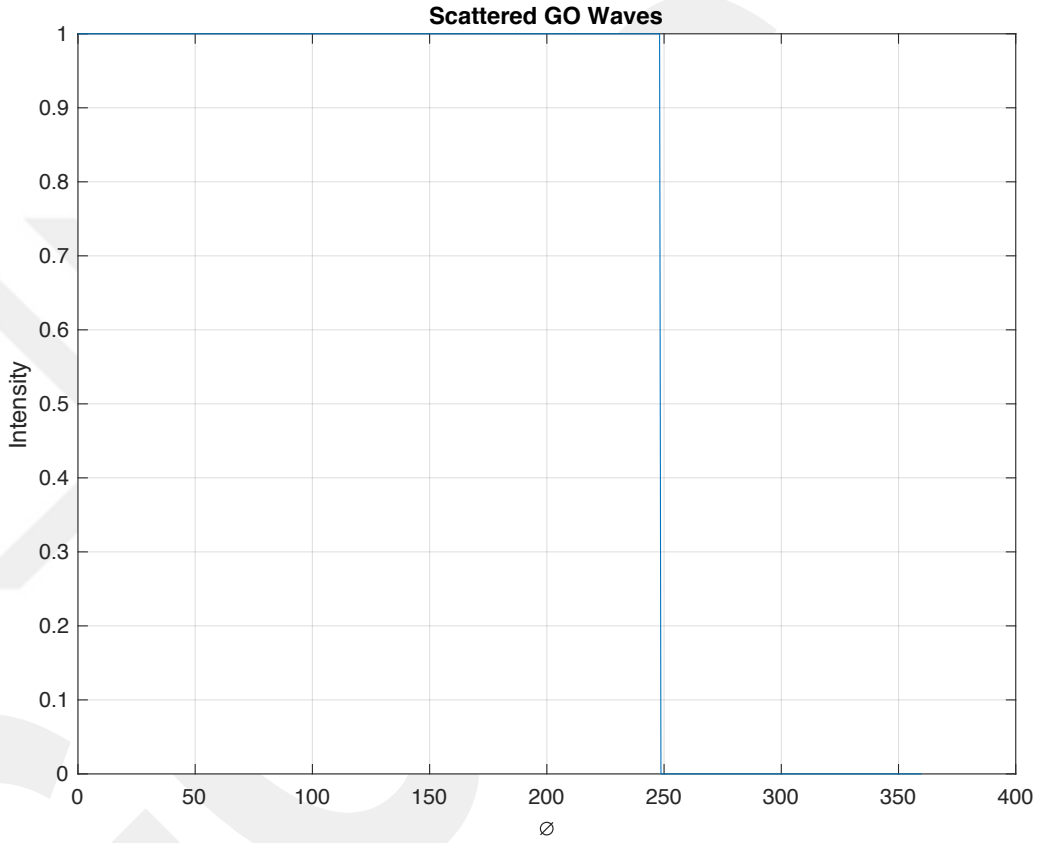

Figure 62. Scattered GO Wave

7.3. Uniform Diffracted Fields From +a Point

Diffracted GO waves by PAS at +a is shown as

$$E_{ud}^{+a} = e^{jkacos(\emptyset_0)} e^{jkR_a \cos(\beta_a - \emptyset_0)} \, sign(\zeta_{id+a}) F(|\zeta_{id+a}|). \quad (7.7)$$

Total uniform diffracted wave at +a can be shown in Figure 63.

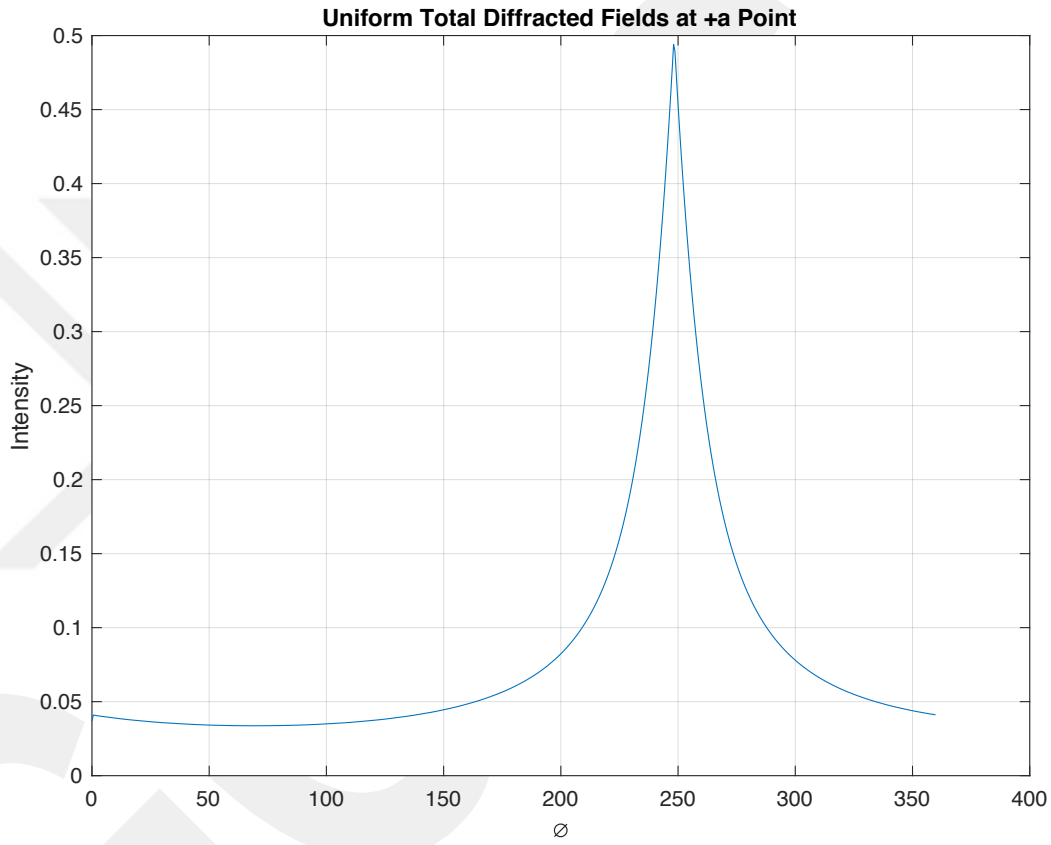

Figure 63. Total uniform diffracted wave at +a Point

7.4. Uniform Diffracted Fields From -a Point

Diffracted GO waves by PAS at -a is shown as

$$E_{ud}^{-a} = e^{-jkacos(\emptyset_0)} e^{jkR_{-a}\cos(\beta_{-a}-\emptyset_0)}\, sign\left(\zeta_{id\,-a}\right) F\left(\left|\zeta_{id\,-a}\right|\right). \qquad (7.8)$$

Total uniform diffracted wave at -a point can be shown in Figure 64.

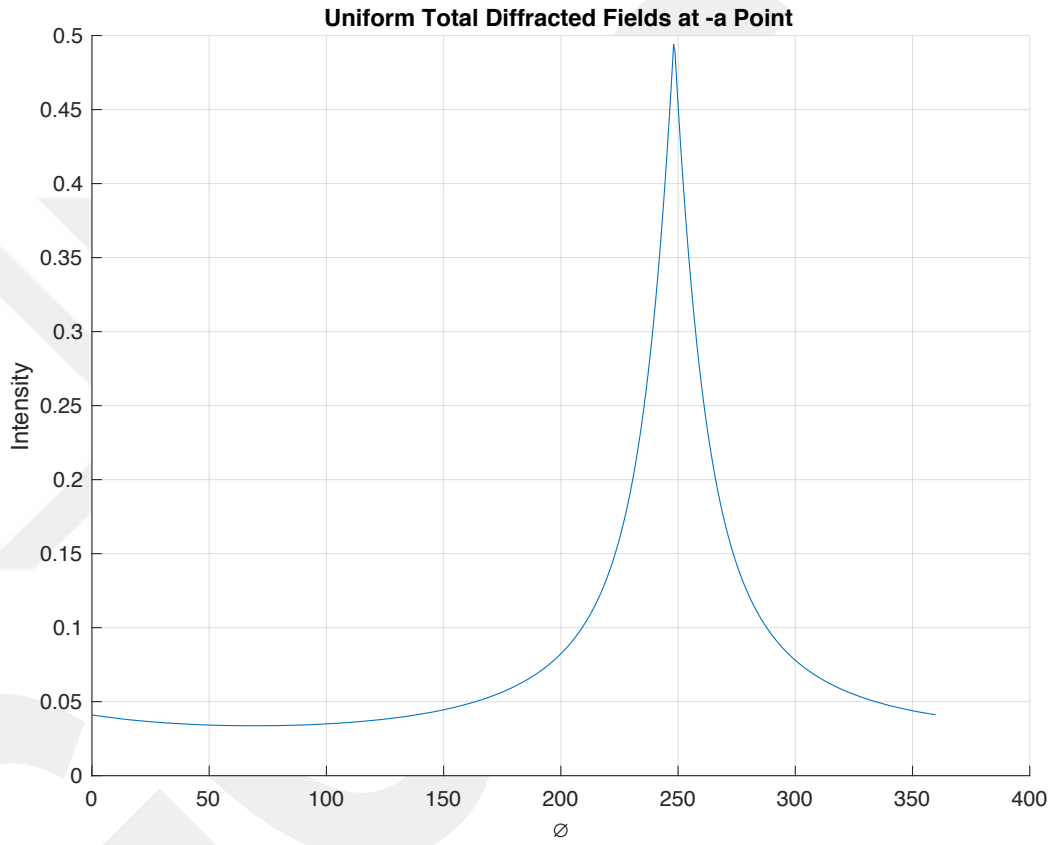

Figure 64. Total uniform diffracted wave at -a Point

7.5. Total Scattered Fields

Total scattered fields by PAS can be expressed as

$$E_{ts} = E_i + E_{ud}^{-a} + E_{ud}^{+a}. \tag{7.9}$$

Total scattered fields by PAS can be shown in Figure 65.

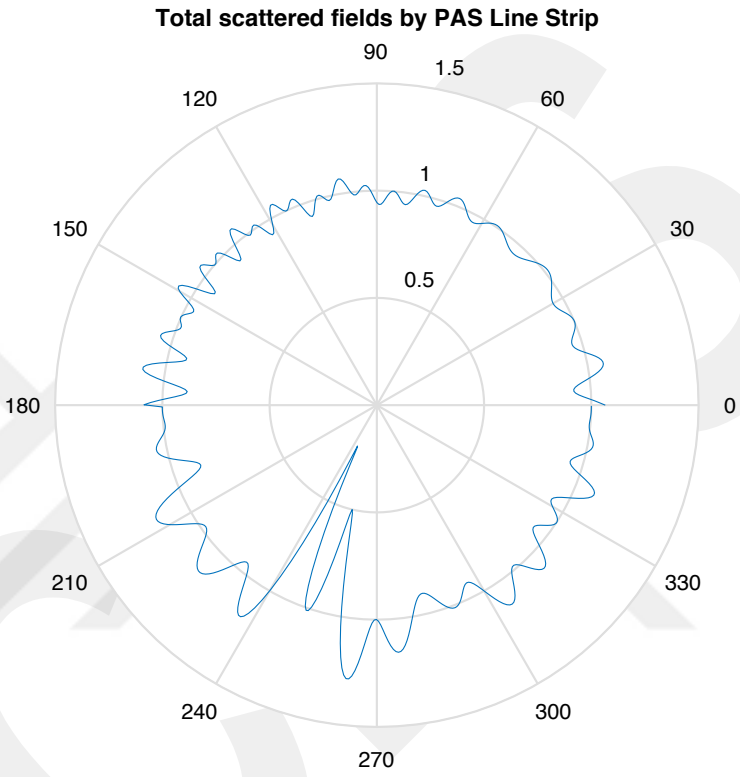

Figure 65. Total scattered fields by PAS strip

In Figure 65, it is shown that incident GO wave which is scattering by line strip from -a to a is appearing between 0° and 360°. Difference between civilian plane and stealth aircraft is that there are no interference caused by reflected GO wave and uniform reflected diffracted waves between 0° and 360°. Incident GO wave which is scattering between -a and a and uniform incident diffracted waves which are scattered by edge points are interfered between 0° and 360°. However, uniform incident diffracted field is taken maximum amplitude at 248.1°. There is shadow region around 244.7°.

CHAPTER 8

8. NUMERICAL ANALYSIS

Until this section, all evaluations are done uniformly. This section attenuations, dimensions of planes, satellite carrier frequency will be considered.

8.1. Applying Attenuations to Satellite's Radiated Field

Radiated field from satellite is modeled as Gaussian beam in Section 4. In Figure 66, electromagnetic wave which is radiating from satellite antenna and including attenuations of atmospheric effects is shown.

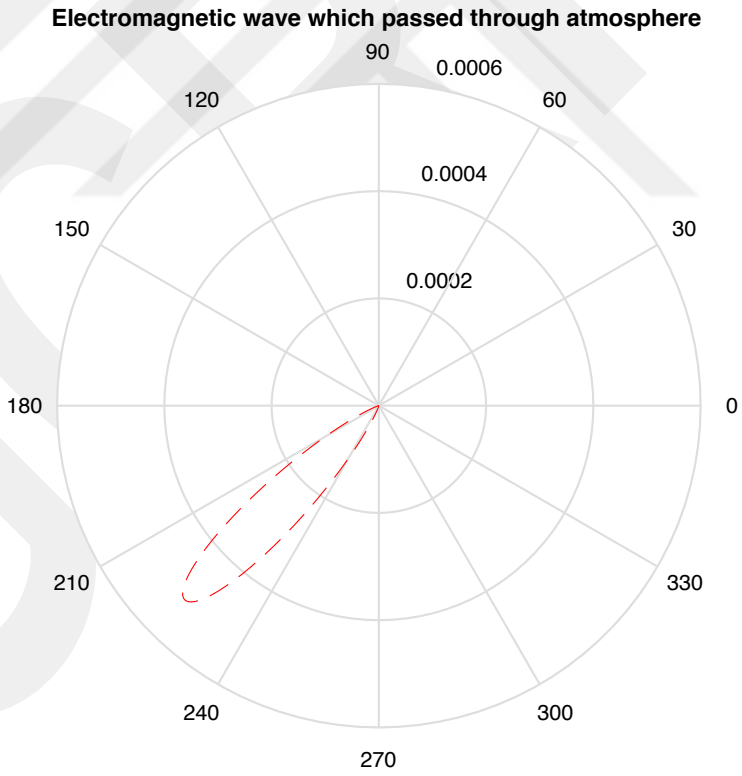

Figure 66. Electromagnetic wave which passed through atmosphere

8.2.Applying Dimensions of Civilian Plane

In this section, a is equal to 20.335m. λ is equal to 0.03m which is carrier frequency of satellite. ρ is equal to 122m. Total scattered field by civilian plane is shown in Figure 67.

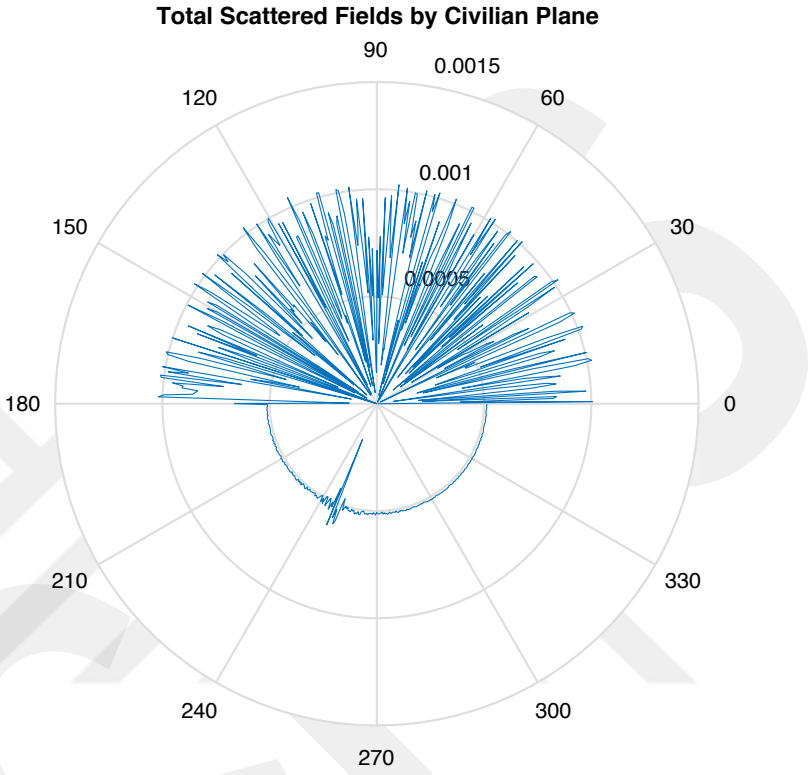

Figure 67. Total scattered fields by civilian plane

In Figure 67, it is shown that incident GO wave and reflected GO wave which are scattering by line strip from -a to a and uniform diffracted fields which are scattered from edge points are interfered between 0° and 180°. Incident GO wave which is scattering between -a and a and uniform diffracted waves which are scattered by edge points are interfered between 180° and 360°. Incident GO wave exists between 0° and 360°. There is shadow region around 244.7°.

8.3. Applying Dimensions of Stealth Aircraft

In this section, a is equal to 10.04m. λ is equal to 0.03m which is carrier frequency of satellite. ρ is equal to 60.24m. Total scattered field by stealth aircraft is shown in Figure 68.

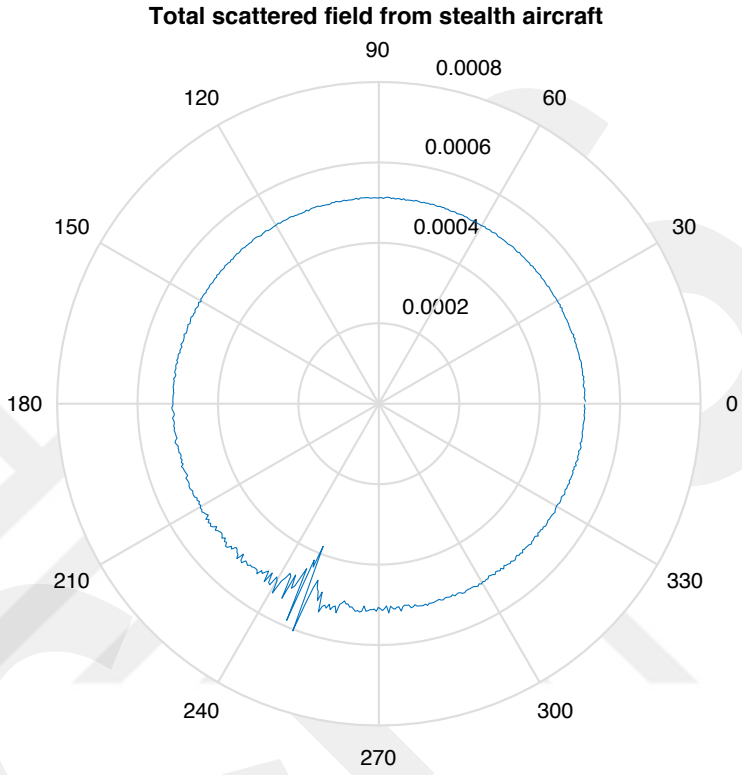

Figure 68. Total scattered fields by stealth aircraft

In Figure 68, it is shown that incident GO wave which is scattering by line strip from -a to a is appearing between 0° and 360°. Difference between civilian plane and stealth aircraft is that there are no interference of reflected GO wave and uniform reflected diffracted waves between 0° and 360°. Incident GO wave which is scattering between -a and a and uniform incident diffracted field which is scattered by edge points are interfered between 0° and 360°. There is shadow region around 244.7°.

CHAPTER 9

9. RESULTS

Electromagnetic fields are investigated at Section 3, Section 6 and Section 7. In this section, results are discussed radar point of view. Observed electromagnetic fields by ground-based receiver radar system and difference between the unaffected satellite signal and the affected satellite signal by target will be represented.

Civilian plane's total scattered fields are shown at Figure 67. Ground-based receiver radar is receiving plane wave from satellite if there is no target above country. The general view is becoming apparent with applying the real dimensions to the strip. Plane is looking as point from location of satellite. This is observing very well between 180° and 360°. It is apparent that there are scintillations where uniform incident diffracted fields and incident GO wave are interfered around 248.1°. These scintillations can be used to detect targets in satellite based passive radar system. Difference between unaffected satellite electromagnetic fields and affected satellite electromagnetic fields by target is shown at Figure 69. Ground-based receiver radar system receives the electromagnetic fields between 180° and 360°. So, target can be detected by using scintillations around the 244.7° which is called as shadow region.

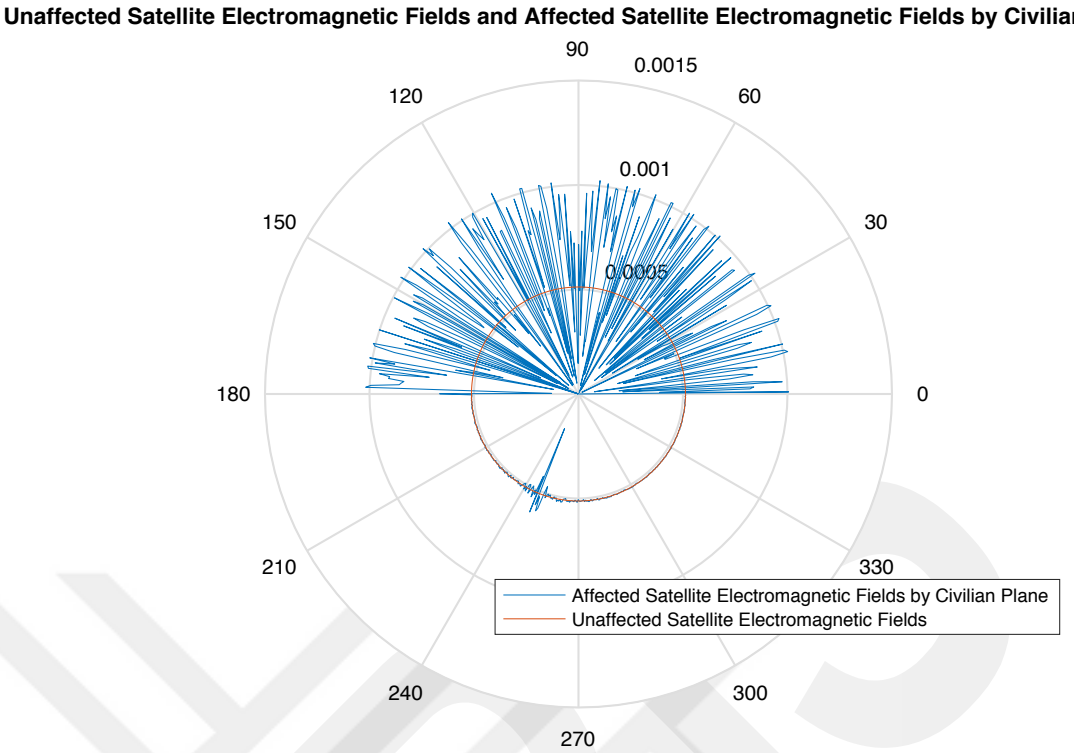

Figure 69. Unaffected satellite electromagnetic fields and affected satellite electromagnetic fields by civilian plane

Stealth aircraft's total scattered fields are shown at Figure 68. Ground-based receiver radar is receiving plane wave from satellite if there is no target above country. The general view is becoming apparent with applying the real dimensions to the strip. Plane is looking as point from location of satellite. This is observing very well between 180° and 360°. It is apparent that there are scintillations where uniform incident diffracted fields and incident GO wave are interfered around 248.1°. These scintillations can be used to detect targets in satellite based passive radar system. Difference between unaffected satellite electromagnetic fields and affected satellite electromagnetic fields by target is shown at Figure 70. Ground-based receiver radar system receives the electromagnetic fields between 180° and 360°. So, target can be detected by using scintillations around the 244.7° which is called as shadow region.

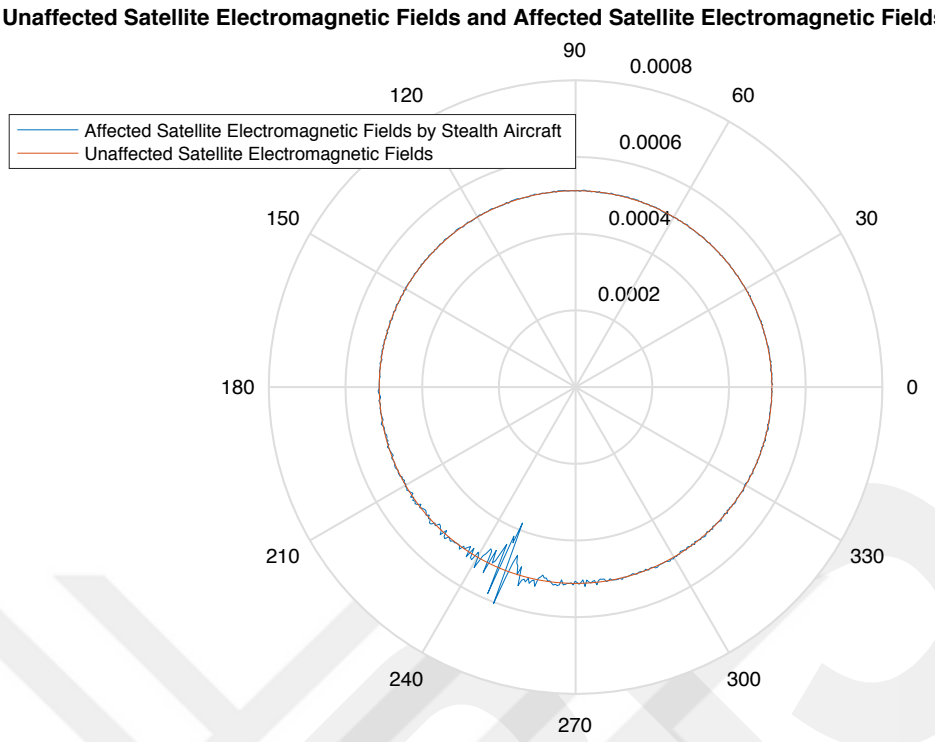

Figure 70. Unaffected satellite electromagnetic fields and affected satellite electromagnetic fields by stealth aircraft

As a result, detection way using electromagnetic fields difference for satellite based passive radar system is represented. Effect of target to the electromagnetic fields which is radiated from satellite is indicated clearly at Figure 69 and Figure 70. Electromagnetic fields differences are represented.

CHAPTER 10

10. CONCLUSION

As a conclusion, the one of the most important agenda topic in the world which is satellite based passive radar system is researched in point of electromagnetic propagation. There are six important key point in this thesis. These are that MTPO method is investigated, reflected scattered fields by CPRA is found, these reflected scattered fields are modeled as Gaussian beam, atmospheric impairments are modeled, scattering fields by civilian plane which is modeled as PEC surface line strip is evaluated, scattering fields by stealth aircraft which is modeled as PAS line strip is expressed.

MTPO method is used instead of PO Method, [7]. This provide to find exact solution of the scattering integral. PO method has weakness about diffracted fields. This weakness is extinguished. Better solutions are obtained.

CPRA is investigated, [9]. Satellite antenna is modeled as CPRA. MTPO method is used to find scattered fields by CPRA. Incident GO wave, reflected GO wave, uniform incident diffracted and uniform reflected diffracted fields are represented. CPRA's reflected scattered field is used in this thesis as radiated field from satellite antenna.

Gaussian beam is used as model of CPRA reflected scattered field, [24]. Gaussian beam's scattered fields are investigated. Umul's Gaussian beam solutions are implemented, [91]. Incident GO wave of Gaussian beam is used for model of CPRA's reflected scattered field. Result of modelling is shared.

Atmospheric impairments are studied. ITU-R Recommendation for atmospheric model is used in this thesis, [55-59]. Total attenuation because of atmospheric impairments is represented. It is used in numerical analysis part.

Scattered fields by PEC line strip which is model of civilian plane is evaluated, [60]. Incident GO wave, reflected GO wave, uniform reflected diffracted wave and uniform incident diffracted wave is found. Results are represented. Graph of fields are plotted uniformly. Calculations are done without Boeing 737-900 dimensions.

Scattered fields by PAS line strip which is model of stealth aircraft is evaluated. Kirchhoff integral method is used to define that PAS is summation of soft and hard surface, [68,72,75]. Incident GO wave and uniform incident diffracted wave is observed. Results are represented. Graph of fields are plotted uniformly. Calculations are done without Lockheed F-117 Nighthawk's dimensions.

In the numerical analysis part of this thesis, all details take into consideration when simulations are running. Atmospheric attenuations, target dimensions, path lengths are implemented to simulations.

Results show that detection of target with using satellite based passive radar is possible because of the anomaly which is occurred by interference of diffracted fields and incident GO wave. Difference between receiving signal from satellite without target interception and receiving signal with target interception is represented. If there is no target, ground-based receiver radar system will receive plane wave. However, if there is a target, there will be scintillations in plane wave. This issue is well investigated. All results are shared clearly.

11. REFERENCES

[1] L. L. Yik, "The Modelling and Simulation of Passive Bistatic Radar," March 2013. [Online]. Available: https://digital.library.adelaide.edu.au/dspace/bitstream/2440/80577/8/02whole.pdf.

[2] Y. Miyazaki and W. Asano, "Electromagnetic wave scattering by buildings and objects in radio and mobile communication,"," in *IEEE 1991 International Symposium on Electromagnetic Compatibility*, New Jersey, 1991.

[3] P. Valtr and F. Perez-Fontan, "Modeling of Wave Scattering from Rough Building," in *2008 IEEE International Workshop on Satellite and Space Communications*, Edinburgh, 2008.

[4] J. E. Allnut, Satellite-to-Ground Radiowave Propagation, London: The Institution of Engineering and Technology, 2011.

[5] J. Louis and J. Ippolito, Satellite Communications Systems Engineering, West Sussex: A John Wiley & Sons, 2008.

[6] D. Roddy, Satellite Communications, Chicago: McGraw-Hill, 2006.

[7] Y. Z. Umul, "Modified theory of physical optics," *J. Opt. Soc. Of America,* vol. 12, no. 20, pp. 4959-4970, 2004.

[8] G. L. James, Geometrical Theory of Diffraction for Electromagnetic, London: The Institution of Engineering and Technology, 1986.

[9] Y. Z. Umul, "Scattering of a line source by a cylindrical," *J.Opt.Soc. Am. A,* vol. 25, no. 7, pp. 1652-1659, 2008.

[10] A. Büyükaksoy and G. Uzgören, "High-frequency scattering from the impedance discontinuity on a cylindrically curved surface," *IEEE Trans. Antennas Propag,* vol. 35, pp. 234-236, 1987.

[11] I. Akduman and A. Büyükaksoy, "Asymptotic expressions for the surface currents induced on a cylindrically curved impedance strip," , vol. 43, p. 453–463, 1995.," *IEEE Trans. Antennas Propag,* vol. 43, pp. 453-463, 1995.

[12] O. M. Bucci and G. Franceschetti, "Rim loaded reflector antennas," *IEEE Trans. Antennas Propag,* vol. 28, pp. 297-305, 1980.

[13] U. Yalçın and M. Sarnık, "Uniform Diffracted Fields from a Perfectly Conducting Cylindrical Reflector with Modified Theory of Physical Optics," *The Scientific World Journal,* pp. 1-6, 2013.

[14] M. Sarnık and U. Yalçın, "Uniform scattered fields from a perfectly conducting," *Optics,* vol. 135, pp. 320-326, 2017.

[15] M. Kara, "Scattering of a plane wave by a cylindrical parabolic perfectly electric," *Optik,* vol. 135, pp. 320-326, 2017.

[16] H. A. Ragheb, "Simulation of cylindrical reflector antennas," May 1987. [Online]. Available: https://mspace.lib.umanitoba.ca/xmlui/bitstream/handle/1993/16566/Ragheb_Simulation_of.pdf?sequence=1&isAllowed=y.

[17] T. Takenaka, M. Kakeya and O. Fukumitsu, "Asymptotic representation of the boundary diffraction wave for a Gaussian beam incident on a circular aperture," *J. Opt. Soc. Am.,* vol. 70, p. 1323–1328, 1980.

[18] S. Kimura and C. Munakaga, "Measurement of a Gaussian laser beam spot size using a boundary diffraction wave," *Appl. Opt.,* vol. 27, pp. 84-88, 1988.

[19] J. E. Pearson, T. C. McGill, S. Kurtin and A. Yariv, "Diffraction of Gaussian laser beams by a semi-infinite plane," *J. Opt. Soc. Am.,* vol. 59, pp. 1440-1445, 1969.

[20] G. Otis, "Application of the boundary-diffraction-wave theory to Gaussian beams," *J. Opt. Soc. Am.,* vol. 64, pp. 1545-1550, 1974.

[21] G. Otis and J. W. Lit, "Edge-on diffraction of a Gaussian laser beam by a semi-infinite plane," *Appl. Opt.,* vol. 14, pp. 1156-1160, 1975.

[22] G. A. Suedan and E. V. Jull, "Beam diffraction by half-planes and wedges: Uniform and asymptotic solutions," *J. Electromagn. Waves Appl.,* vol. 3, pp. 17-26, 1989.

[23] G. A. Suedan and E. V. Jull, "Approximating beam diffraction by a half-plane," *J. Electromagn. Waves Appl.,* vol. 6, pp. 287-295, 1992.

[24] Y. Z. Umul, "Beam diffraction by a resistive half-plane," *APLLIED OPTICS,* vol. 54, no. 10, pp. 2665-2671, 2015.

[25] F. Yuan, S. Manadhar and Y. H. Lee, "Investigation of Gaseous Attenuation on a Ka-Band Propagation Link in Tropical Region," in *2017 USNC-URSI Radio Science Meeting (Joint with AP-S Symposium)*, San Diego, 2017.

[26] Y. Gataullin and R. Kozlowski, "MPLEMENTATION OF RAIN AND GASEOUS ATTENUATION MODELS FOR 26-30 GH KA-BAND COMMUNICATION," in *Proceedings on the 6th IASTED International Conference Antennas,Radar and Wave Propagation*, Canada, 2009.

[27] Z. Minggao, "A modification to previous ITU-R simplified model for gaseous attenuation," in *in Proceedings of 1997 Asia-Pacific Microwave Conference*, Hong Kong, 2002.

[28] R. Pollard and H. Helmken, "Estimation of gaseous absorption using surface and radiosonde meteorological measurements," in *in Proceedings IEEE SoutheastCon 2002*, Columbia, 202.

[29] P. Bouchard, "Simplified method for estimating gaseous absorption at low elevation angles along earth-space paths," in *2010 14th International Symposium on Antenna Technology and Applied Electromagnetics & the American Electromagnetics Conference*, Ottowa, 2010.

[30] P. Bouchard, "Approximate Method for Estimating Gaseous Loss at Very Low Angles Along Paths of Finite Length and Earth-Space Paths," *IEEE Transactions on Antennas and Propagation,* vol. 64, no. 2, pp. 687-699, 2016.

[31] J. M. Garcia-Rubia, J. M. Riera and P. Garcia-del-Pine, "Attenuation Measurements and Propagation Modeling in the W-Band," *IEEE Transactions on Antennas and Propagation,* vol. 61, no. 4, pp. 1860-1867, 2013.

[32] S. A. Akinwumi and e. al., "Atmospheric gases attenuation in West Africa," in *2016 IEEE Radio and Antenna Days of the Indian Ocean (RADIO)*, St.Gilles-Ies-Bains, 2016.

[33] P. W. Rosenkranz, "Absorption of microwaves by atmospheric gases," in *Atmospheric Remote Sensing by Microwave Radiometry*, New York, John Wiley & Sons Inc., 1993, pp. 37-79.

[34] M. Grabner, V. Kvicera and J. Kostelecky, "Application of Water Vapour Profiling for Gaseous Attenuation Estimation – Radiometer versus Radiosonde Results," in *Proceedings of the 8th International Symposium on Tropospheric Profiling*, Delft, 2010.

[35] P. K. Karmakar and et al., "Some of the atmospheric influences on microwave propagation through atmosphere," *AMERICAN JOURNAL OF SCIENTIFIC AND INDUSTRIAL RESEARCH,* vol. 1, no. 2, pp. 350-358, 2010.

[36] K. K. Srinivas and T. V. Raman, "Severe Cause of Cloud Attenuation and Rain Attenuation on Space Communication Link at Millimetre Band and Differentiation between Rain Attenuation and Cloud Attenuation," in *2017 IEEE 7th International Advance Computing Conference (IACC)*, Hyderabad, 2017.

[37] M. G. Murtaza, A. M. Imran and M. I. Kamrul, "Investigation of cloud attenuation over Bangladesh for microwave communications," in *2017 20th International Conference of Computer and Information Technology (ICCIT)*, Dhaka, 2017.

[38] H. Singh, B. Bonev and P. Petkov, "Cloud attenuation model at millimeter frequency bands," in *2017 International Conference on Infocom Technologies and Unmanned Systems (Trends and Future Directions) (ICTUS)*, Dubai, 2017.

[39] F. Yuan, S. Manandhar, Y. H. Lee and Y. S. Meng, "Model comparison for estimating cloud liquid water content and attenuation in tropical region," in *2016 IEEE Region 10 Conference (TENCON)*, Singapore, 2016.

[40] K. Luini and C. Capsoni, "Predicting cloud attenuation on Earth-space EHF links," in *2015 9th European Conference on Antennas and Propagation (EuCAP)*, Lisbon, 2015.

[41] F. Yuan and et al., "Statistical Study of Cloud Attenuation on Ka-Band Satellite Signal in Tropical Region," *IEEE Antennas and Wireless Propagation Letters,* vol. 16, pp. 2018-2021, 2017.

[42] R. Yang, L. Li, Z. Zhao and T. Lu, "Cloud simulation and attenuation at Ka band on slant path," in *2013 Cross Strait Quad-Regional Radio Science and Wireless Technology Conference*, Chengdu, 2013.

[43] J. S. Mandeep and S. I. Hassan, "Cloud Attenuation for Satellite Applications Over Equatorial Climate," *IEEE Antennas and Wireless Propagation Letters,* vol. 7, pp. 152-154, 2008.

[44] L. Luini and C. Capsoni, "Efficient Calculation of Cloud Attenuation for Earth–Space Applications," *IEEE Antennas and Wireless Propagation Letters,* vol. 13, pp. 1136-1139, 2014.

[45] T. Mao, D. Zhou and Z. Niu, "The calculation model of the attenuation due to clouds or fog and the analysis of its characteristic," in *2004 Asia-Pacific Radio Science Conference*, Qingdao, 2004.

[46] T. V. Omotosho, J. S. Mandeep and M. Abdullah, "Cloud-Cover Statistics and Cloud Attenuation at Ka- and V-Bands for Satellite Systems Design in Tropical

Wet Climate," *IEEE Antennas and Wireless Propagation Letters,* vol. 10, pp. 1194-1196, 2011.

[47] D. V. Grishin, D. Y. Danilov and L. V. Kurakhtenkov, "Use of ITU-R recommendations in calculating tropospheric signal attenuation in the simulation modeling problems of satellite systems," in *2017 Systems of Signal Synchronization, Generating and Processing in Telecommunications*, Kazan, 2017.

[48] P. Dvorak and C. Capsoni, "Model for synthesis of short-term tropospheric amplitude scintillation," in *2016 10th European Conference on Antennas and Propagation*, Davos, 2016.

[49] F. S. Marzano and C. Riva, "Evidence of long-term correlation between clear-air attenuation and scintillation in microwave and millimeter-wave satellite links," *IEEE Transactions on Antennas and Propagation,* vol. 47, no. 12, pp. 1749-1757, 1999.

[50] M. M. Kamp, J. K. Tervenon and E. T. Salonen, "Improved models for long-term prediction of tropospheric scintillation on slant paths," *IEEE Transactions on Antennas and Propagation,* vol. 47, no. 2, pp. 249-260, 1999.

[51] N. B. Rahim and et al., "Analysis of long term tropospheric scintillation from Ku-band satellite link in tropical climate," in *2012 International Conference on Computer and Communication Engineering*, Kuala Lumpur, 2012.

[52] T. V. Omotosho and et al., "Tropospheric scintillation and its impact on earth-space satellite communication in Nigeria," in *2016 IEEE Radio and Antenna Days of the Indian Ocean*, St.Gilles-Ies-Bains, 2016.

[53] M. M. Kamp, J. K. Tervonen and E. T. Salonen, "Tropospheric scintillation measurements and modelling in Finland," in *Tenth International Conference on Antennas and Propagation*, Edinburgh, 2002.

[54] H. Dao, I. M. Rafigul, J. Chebil and K. Al-Khaateeb, "Scintillation measurement on Ku-band satellite path in tropical climate," in *2013 IEEE International RF and Microwave Conference*, Penang, 2013.

[55] "Attenuation due to clouds and fog," ITU-R Recommendation P.840-6, Geneva, 2013.

[56] "Propagation data and prediction methods required for the design of Earth-space telecommunication systems," ITU-R Recommendation P.618-13, Geneva, 2017.

[57] "Rain height model for prediction methods," ITU-R Recommendation P.839-4, Geneva, 2013.

[58] "Prediction of path attenuation on links between an airborne platform and Space and between an airborne platform and the surface of the Earth," ITU-R Recommendation P.2041-0, Geneva, 2013.

[59] "Attenuation by atmospheric gases," ITU-R Recommendation P.676-10, Geneva, 2016.

[60] Y. Z. Umul, "Physical optics theory for the scattering of waves by an impedance strip," *Optics Communications,* vol. 284, pp. 1760-1765, 2011.

[61] B. Sieger, "Die beugung einer ebenen elektrischen welle an einem schirm von elliptischem querschnitt," *Ann. Phys.,* p. 626, 1908.

[62] M. I. Herman and J. L. Volakis, "High-frequency scattering by a resistive strip and extensions to conductive and impedance strips," *Radio Sci.,* p. 335, 1987.

[63] E. Erdoğan, A. Büyükaksoy and O. Bicakci, "Plane-wave diffraction by a two-part impedance strip," *IEEE Proc. Sci. Meas. Technol.,* vol. 141, no. 5, pp. 383-390, 1994.

[64] H. D. Başdemir, "Impedance surface diffraction analysis for a strip with the boundary diffraction wave theory," *Optik,* vol. 124, pp. 627-630, 2013.

[65] G. A. Kirchhoff, "Zur Theorie der Lichtstrahlen," *Ann. Phys.,* vol. 254, pp. 663-695, 1883.

[66] Y. Z. Umul, "Wave diffraction by a soft/hard strip: Modified theory of physical optics solution," *Optics,* vol. 156, pp. 857-865, 2018.

[67] Y. Z. Umul, "A new representation of the Kirchhoff's diffraction integral Author links open overlay panelYusufZiya Umul," *Optics Communications,* vol. 291, pp. 48-51, 2013.

[68] Y. Z. Umul, "Fictitious diffracted waves in the diffraction theory of Kirchhoff," *Journal of the Optical Society of America A,* vol. 27, no. 1, pp. 109-115, 2010.

[69] Y. Z. Umul, "Modified diffraction theory of Kirchhoff," *Journal of the Optical Society of America A,* vol. 25, no. 8, pp. 1850-1860, 2008.

[70] Y. Z. Umul, "Diffraction of plane waves by a black wedge," *Optics & Laser Technology,* vol. 42, no. 1, pp. 32-36, 2010.

[71] J. S. Asvestas, "Diffraction by a black screen," *J. Opt. Soc. Am.,* vol. 65, pp. 155-158, 1975.

[72] Y. Z. Umul, "Diffraction of waves by a planar junction between perfectly absorbing and resistive sheets," *Optik,* vol. 158, pp. 1436-1442, 2018.

[73] Y. Z. Umul, "Diffraction of Electromagnetic Waves by a Wedge with Perfectly Absorbing and Impedance Faces," *Optik,* no. 174, pp. 416-424, 2018.

[74] Y. Z. Umul, "Diffraction of electromagnetic waves by a wedge with perfectly absorbing and impedance faces," *Optik,* vol. 174, pp. 416-424, 2018.

[75] Y. Z. Umul, "Diffraction of plane waves by the interface between black and soft/hard semi-planes," *Optik,* vol. 123, no. 7, pp. 624-628, 2012.

[76] Y. Z. Umul, "Diffraction by a black half plane: Modified theory of physical optics approach," *Optics Express,* vol. 13, no. 19, pp. 7276-7287, 2005.

[77] C. J. Marcinkowski, "Some diffraction patterns of an absorbing half-plane," *Appl. Sci. Res. B 9,* pp. 189-198, 1961.

[78] A. C. Green, H. L. Bertoni and L. B. Felsen, "Properties of the shadow cast by a half-screen when illuminated by a Gaussian beam," *J. Opt. Soc. Am,* vol. 69, pp. 1503-1508, 1979.

[79] G. D. Malyughinetz, "Das Sommerfeldsche Integral und die Lösung von Beugungsaufgaben in Winkelgebieten," *Ann. Phys.,* vol. 461, pp. 107-112, 1960.

[80] J. Mabie, "Detection of Mesoscale Magnetic Eddies in the E-layer Ionosphere using the Vertically Incident Pulsed Ionospheric Radar," 2011. [Online]. Available: ftp://ftp.ngdc.noaa.gov/wdc/geomagnetism/tmp/special/Rocket/Mabie_comps2.pdf.

[81] S. V. Hum, "Ionospheric Propagation," 09 08 2018. [Online]. Available: http://www.waves.utoronto.ca/prof/svhum/ece422/notes/20c-ionosphere.pdf.

[82] Y. Z. Umul, "Equivalent functions for the Fresnel integral," *J. Opt. Soc. Of America,* vol. 13, no. 21, pp. 8469-8482, 2005.

[83] D. T. Xenos and V. T. Yioultsis, "FTDT Method With Oblique Incidence," *IEEE TRANSACTIONS ON MAGNETICS,* vol. 38, pp. 677-680, 2002.

[84] W. Z. Wu, J. Wu and S. Z. Wu, "A survey of ionospheric effects on space-based radar," *Waves in Random Media,* vol. 14, no. 2, pp. 189-273, 2004.

[85] S. M. Canta, D. Erricolo and A. Toccafondi, "Incremental Fringe Formulation for a Complex," *IEEE TRANSACTIONS ON ANTENNAS AND PROPAGATION,* vol. 59, no. 5, pp. 1553-1561, 2011.

[86] A. Ghasemi, A. Abedi and F. Ghasemi, Propagation Engineering in Radio Links Design, New York: Springer, 2013.

[87] "The radio refractive index: its formula and refractivity data," ITU-R Recommendation P.453-13 , Geneva, 2017.

[88] T. U. H. K. T. v. İ. A.Ş., "Türksat 4A," [Online]. Available: https://www.turksat.com.tr/sites/default/files/uydu/turksat_4a_uydu_kart_2.pdf . [Accessed 15 Dec 2018].

[89] "BOEING 737-900 Dimensions," September 16 2017. [Online]. Available: https://www.facebook.com/sntma.dz/?hc_ref=ARTeewjTwVllcXd1nEYGvENRNB0WKl19-jsSSH5Xx0fZ4Ho_cxGw2Mfqeup9Fi5zA7I&fref=nf&__xts__[0]=68.ARADqTr7HavZaI76PjUWlbmrpVonBWjqAz-wqYGtQXxTWJ_VygtZ8A1Z2QfIM2s-MSW3kj4ZTwzpmIzhE5XWhMNeNLS7OeyRyAXRxYstnHawE7zN5tELYrT2JT3.

[90] "F-117 drawing," [Online]. Available: http://www.aerospaceweb.org/aircraft/bomber/f117/pics03.shtml. [Accessed 2018 Dec 22].

[91] Y. Z. Umul, "Scattering of gaussian beam by an impadence," *J. Opt. Soc. Am. A,* vol. 24, no. 10, pp. 3159-3167, 2007.

[92] K. C. Yeh and C. H. Liu, Theory of Ionospheric Waves, New York: Academic Press, 1972.

[93] M. Zubair, Z. Haider, S. A. Khan and J. Nasir, "Atmospheric influences on satellite communications," *PRZEGLĄD ELEKTROTECHNICZNY (Electrical Review),* vol. 87, no. 5, pp. 261-264, 2011.

[94] J. Proakis, Digital Communications, New York: McGraw-Hill, 2001.